University of South-Eastern Norway

www.usn.no

FMH606 Master's Thesis 2019
Process Technology

Thermal Ignition of Surrogate Jet Fuels

Sveinung M. Sund

Faculty of Technology, Natural Sciences and Maritime Sciences
Campus Porsgrunn

University of South-Eastern Norway

www.usn.no

Course: FMH606 Master's Thesis 2019
Title: *Thermal Ignition of Surrogate Jet Fuels*
Pages: *128*
Keywords: *<safety, combustion, ignition, thermal ignition, hot surface, jet fuel, surrogate>*

Student: *Sveinung M. Sund*
Supervisor: *Prof. Joseph E. Shepherd, Prof. Dag Bjerketvedt*
External partner: *Caltech, The Boeing Company*
Availability: *Open*

Summary:
An understanding of the ignition characteristics of jet fuel is important to enable safe design and operation of aircraft, storage facilities, and refineries. However, the complexity and variability of jet fuel composition makes it impractical to model and study in a repeatable manner. Jet fuel surrogates are mixtures of fewer, well-studied hydrocarbons designed to mimic the relevant characteristics of jet fuel, while being easier to study. For safety applications, the thermal ignition properties of the surrogate fuel is one such relevant characteristic. In this work, the hot surface ignition temperatures of three surrogates of increasing complexity were determined experimentally. The selected surrogates: dodecane, Aachen, and JI Unified, were mixed with dry air to atmospheric pressure in a 2.2 liter vessel heated to $403 \pm 5\,\mathrm{K}$ and ignited by a 10 mm x 10 mm stainless steel cylinder ($D/L = 1$). The cylinder was heated at 90 W to 130 W and $10.7\,\mathrm{K\,s^{-1}}$ to $14.3\,\mathrm{K\,s^{-1}}$ (average over 45 seconds). The cylinder surface temperature was measured by 2-color pyrometry and the ignition events were captured by Mach-Zehnder interferometry. For dodecane, the average ignition temperature over all experiments ($n = 26$) was $1020 \pm 50\,\mathrm{K}$. The standard deviation for the observations was $s = 27$. The minimum ignition temperature observed was $977 \pm 50\,\mathrm{K}$ at $\phi = 1.47 \pm 0.068$, and the maximum was $1067 \pm 50\,\mathrm{K}$ at $\phi = 0.95 \pm 0.068$. For the Aachen surrogate, the mean ($n = 6$) ignition temperature ($0.75 < \phi < 1.25$) was $1061 \pm 50\,\mathrm{K}$ ($s = 2.6$). At richer conditions, only one ignition event was captured ($\phi = 2.44 \pm 0.022$) at a temperature of $1122 \pm 50\,\mathrm{K}$, characterized by a weak pressure transient and puffing flame behavior. Richer ignition attempts within the calculated flammability limits did not ignite. For the JI surrogate at $0.79 < \phi < 1.22$, the average ignition temperature ($n = 3$) was 1061 K ($s = 4$) with a minimum of $999 \pm 50\,\mathrm{K}$ and a maximum of $1006 \pm 50\,\mathrm{K}$. Away from the flammability limits, the ignition temperature was independent of stoichiometry for all fuels studied. The ignition temperature was found to be dependent on the heating rate, and at similar heating rates, the fuels showed similar ignition temperatures.

Acknowledgements

Firstly, I would like to thank my Norwegian advisor, Professor Dag Bjerketvedt, for his kind support and for making my stay at Caltech possible. In the same vein, I would like to thank Professor Joseph Shepherd for welcoming me to the GALCIT Explosion Dynamics Laboratory and making me feel like a valuable member of the group from day one. I am very grateful for the opportunity to take courses and conduct research in such a great scientific environment. I could not wish for a better advisor; the creative ideas, insights, and encouragement along the way made the work a pleasure.

Furthermore, I want to thank the other members of the Explosion Dynamics Laboratory who made my stay very enjoyable: J.C Veilleux, Silken Jones, Conor Martin, Bohoon Kim, Yunliang Qi, and Barbara McKinzie Slater. A special thanks goes out to the brilliant Silken Jones for her invaluable mentorship and assistance in the lab, and to Conor Martin for the fruitful collaboration on jet fuel surrogates.

Lastly, I would like to thank the Boeing Company for funding this work and providing valuable input along the way, and the Norway-Fulbright Foundation for sponsoring my stay in the U.S.

Pasadena, California, 28th June 2019

Sveinung M. Sund

Contents

Preface **5**

Contents **8**
List of Figures . . . 11
List of Tables . . . 13

1 Theory **19**
1.1 Vapor Liquid Equilibrium . . . 19
1.1.1 Non-condensable gases . . . 21
1.1.2 Flash calculation . . . 22
1.1.3 Vapor pressure correlations . . . 23
1.2 Solubility of light gases in hydrocarbons . . . 24
1.2.1 Ostwald coefficient . . . 26
1.3 Reaction kinetics . . . 28
1.3.1 Arrhenius rate law . . . 30
1.4 Ignition criteria . . . 31
1.4.1 Autoignition . . . 32
1.4.2 Hot surface ignition . . . 33
1.5 Reaction equilibrium and thermodynamics . . . 34
1.6 Le Chatelier's mixing rule . . . 36
1.7 Natural convection boundary layer flow . . . 38
1.7.1 Similarity solution . . . 41

2 Jet fuel **43**
2.1 Commercial jet fuel . . . 43
2.1.1 Jet fuel ignition . . . 44
2.1.2 ASTM E 659 autoignition test . . . 45
2.2 Jet fuel surrogates . . . 46
2.2.1 Aachen surrogate . . . 48
2.2.2 JI Unified surrogate . . . 50
2.2.3 Surrogate mixing and analysis . . . 51

3 Previous studies **55**
3.1 Hexane glowplug ignition . . . 55
3.2 Hydrogen, ethylene and hexane hot cylinder ignition . . . 57

4 Surrogate Vapor Liquid Equilibrium **61**
4.0.1 Closed combustion chamber . . . 64
4.0.2 Open combustion chamber . . . 65

5 Methodology **69**
5.1 Combustion vessel . . . 69
5.1.1 External heating and temperature measurement . . . 69
5.1.2 Insulation . . . 70
5.1.3 Mixing . . . 71
5.2 Ignition cylinder . . . 72
5.3 Pyrometer . . . 74
5.3.1 Pyrometer calibration . . . 77
5.3.2 Calibration and temperature measurement error sources . . . 79
5.4 Mach-Zehnder Interferometer . . . 82
5.5 Interferogram post processing . . . 83
5.6 Laser schlieren imaging . . . 86
5.7 Acquisition and triggering . . . 87
5.8 General procedure . . . 87

6 Results **89**
6.1 Ignition thresholds . . . 90
6.1.1 Dodecane . . . 90
6.1.2 Aachen surrogate . . . 92
6.1.3 JI Unified surrogate . . . 93
6.2 Ignition dynamics . . . 95

7 Discussion **101**
7.1 Error sources . . . 101
7.2 Heating rate dependence . . . 102
7.2.1 Atmospheric vs dry air . . . 106

8 Conclusion **107**

Bibliography **109**

A Shot Checklist Procedure **117**

B Certificate of Analysis **119**

C Part CAD drawings **122**

D Shotlists **126**

List of Figures

1.1 Single equilibrium stage phase separator (flash drum). 23
1.2 Solubility (Ostwald coefficient) of O_2 and N_2 in jet fuel as a function of temperature [9]. 27
1.3 Solubility (Ostwald coefficient) of CO_2 in jet fuel as a function of temperature [9]. 28
1.4 Constant volume adiabatic flame temperature vs. equivalence ratio for pure ethylene, hexane and dodecane. Calculated in Cantera using JetSurf2.0 at an initial temperature and pressure of 300 K and 101.3 kPa, respectively. 36
1.5 Constant volume adiabatic combustion pressure vs. equivalence ratio for pure ethylene, hexane and dodecane. Calculated in Cantera using JetSurf2.0 at an initial temperature and pressure of 300 K and 101.3 kPa, respectively. 37
1.6 Water-gas shift reaction species vs. equivalence ratio for constant volume adiabatic combustion of n-dodecane. Calculated in Cantera using JetSurf2.0 at an initial temperature and pressure of 300 K and 101.3 kPa, respectively. 38

2.1 Autoignition and spark ignition limits for jet fuel [36]. 45
2.2 Molecular structure of Aachen surrogate target components. 50
2.3 Molecular structure of JI Unified surrogate target components. 53

3.1 Cross-sectional view of the combustion vessel with glowplug ignition, from Boettcher [41]. Used with permission. 56
3.2 Schematic of the vessel and piping system, from Boettcher [41]. Used with permission. 56
3.3 The glowplug ignition study results of Boettcher [41] for hexane-air at atmospheric pressure. Equivalence ratio uncertainty was +3%/-13% (not shown). Used with permission. 57
3.4 Dark background schlieren time series of hexane flame propagation, from Boettcher [41]. Used with permission. 57
3.5 Surface temperature profiles along the cylinder during heating in air, measured by scanning pyrometry. Horizontal dashed lines mark boundaries of the heated stainless steel cylinder at $y = \pm 5$mm, from Boeck et al. [40]. Used with permission. 58

3.6 Finite fringe interferograms of a non-heated horizontal cylinder (left) and a heated horizontal cylinder (right), from Kink [55]. 59
3.7 Ignition thresholds for stoichiometric fuel-air mixtures. Initial pressure and temperature 101.3 kPa and 296 K, respectively. Auto-ignition temperatures (AIT) from [56]. Figure from Boeck [40]. Used with permission. . . . 59

4.1 Vapor composition of JI Unified surrogate mixed in a vapor-liquid-equilibrium at inlet $\phi = 1$ as a function of temperature. 62
4.2 Fuel vapor composition of JI Unified surrogate at vapor-liquid equilibrium at inlet $\phi = 1$ as a function of temperature (normalized without air). . . . 63
4.3 The dew temperature of selected jet fuel surrogates as a function of equivalence ratio. Calculated in Python using pure component data from the DIPPR database [7]. 65

5.1 Combustion vessel with insulation and beam covers installed. Note that the side injection and top tubing heating installation is not finished in this picture. 71
5.2 Combustion vessel internals with stirbar impeller and lip installed. 72
5.3 Mixing test: Interferograms showing a heated cylinder with impeller off and on 73
5.4 CAD cross-section view of the parts of the cylinder assembly, from Boeck [40]. Used with permission. 73
5.5 CAD drawing of the two-color pyrometer, designed by Boeck [40]. Used with permission. 74
5.6 Black body spectral radiance curve. 75
5.7 Pyrometer calibration setup. 78
5.8 Calibration curve for two-color pyrometer. 79
5.9 Clean (a) and dirty (b) optical access window. 80
5.10 Measured temperature vs. black body temperature for a clean window and no window 80
5.11 Measured temperature vs. black body temperature for a clean and dirty window 81
5.12 Measured temperature vs. black body temperature for calibrations at different points in time. 81
5.13 Mach-Zehnder interferometer set-up (adapted from [55]). 83
5.14 Grid distortion and pixel density test. 84
5.15 Laser schlieren set-up. 86

6.1 Ignition time definition based on high speed imaging and corresponding pyrometer temperature reading at ignition (dodecane shot 23). $t = 0$ indicates time of ignition pressure trigger signal, and t_{ign} is the time defined interval for averaging the ignition temperatures. Experiment conducted using dry air (21.20 vol% O_2), at an equivalence ratio of $\phi = 0.95 \pm 0.068$, initial pressure of $P_0 = 101.3 \pm 0.1\text{kPa}$, and initial temperature of $T_0 = 130 \pm 5°\text{C}$. 90
6.2 Raw and moving average temperature signals (dodecane shot 23). Moving average window size was 500 samples. $t = 0$ indicates time of ignition pressure trigger signal. Experiment conducted using dry air (21.20 vol% O_2), at an equivalence ratio of $\phi = 0.95 \pm 0.068$, initial pressure of $P_0 = 101.3 \pm 0.1\text{kPa}$, and initial temperature of $T_0 = 130 \pm 5°\text{C}$. 91
6.3 Ignition temperature thresholds for dodecane (Sigma-Aldrich ReagentPlus >99%) mixed with dry air (21.2 mol% O_2) at $T_0 = 130 \pm 5°\text{C}$, $P_0 = 101.3 \pm 0.1\text{kPa}$. Heating rate of $90\,\text{W}$ to $130\,\text{W}$, and $11\,\text{K s}^{-1}$ to $14.3\,\text{K s}^{-1}$ (45 second average). 92
6.4 Ignition temperature thresholds for Aachen surrogate (80/20 wt% n-decane/TMB) mixed with dry air (21.2 mol% O_2) at $T_0 = 138 \pm 2°\text{C}$, $P_0 = 101.3 \pm 0.1\text{kPa}$. Heating rate of $95\,\text{W}$ to $(130 \pm 1)\,\text{W}$ and $10.7\,\text{K s}^{-1}$ to $14.4\,\text{K s}^{-1}$ (45 second average). 93
6.5 Heating curves for similar equivalence ratios of dodecane and JI surrogate ignition at heating rates of $115 \pm 1\,\text{W}$ and $12.6 \pm 0.2\,\text{K s}^{-1}$ (45 second average). $t = 0$ indicates time of ignition (pressure trigger). All experiments conducted in dry air (21.20 vol% O_2) at $P_0 = 101.3 \pm 0.1\text{kPa}$ 94
6.6 Ignition temperature thresholds for JI Unified surrogate. 95
6.7 Dodecane ignition dynamics comparison for fast, slow, and puffing flame dynamics. 97
6.8 Dodecane ignition pressure transients for increasing equivalence ratios. . . 98
6.9 Aachen surrogate peak pressure as a function of equivalence ratio from adiabatic constant-volume Cantera simulations and measured peak pressures. 99

7.1 Dodecane (Sigma-Aldrich ReagentPlus >99 mol%) ignition series at heating powers of $115 \pm 1\,\text{W}$ and $130 \pm 1\,\text{W}$. $t = 0$ indicates time of ignition pressure signal. The experiments were all conducted using dry air (21.20 vol% O_2), at equivalence ratios of $0.5 < \phi < 1.5$, initial pressures of $P_0 = 101.3 \pm 0.1\text{kPa}$, and initial temperatures of $T_0 = 130 \pm 5°\text{C}$. 103
7.2 Heating curves for similar equivalence ratios of dodecane and Aachen surrogate ignition. $t = 0$ indicates time of ignition. All experiments conducted in dry air (21.20 vol% O_2) at $P_0 = 101.3 \pm 0.1\text{kPa}$ 104

List of Tables

2.1 U.S. Commercial Turbine Fuel Specifications [9] 44
2.2 Target composition of the selected surrogates for this work. 49
2.3 Component properties for the surrogates from the DIPPR database [7]. . . 49
2.4 Reagent flask data for surrogate pure components. 51
2.5 Component properties for the surrogates listed on the reagent flasks. . . . 51
2.6 Target and measured composition by GC-FID. 52

4.1 DIPPR 101 vapor pressure equation parameters, from the DIPPR 801 database [7], [8] 64
4.2 Dew temperature at different stoichiometries for n-dodecane 65
4.3 Dew temperature at different stoichiometries for Aachen surrogate 66
4.4 Dew temperature at different stoichiometries for JI unified surrogate 66

5.1 Gladstone-Dale constants for common combustion gases [65]. 85

Nomenclature

Symbols used in the text.

Symbol	Explanation
G	Gibbs free energy
μ	Chemical potential
f_i	Fugacity of component i
$\hat{f}_i$	Fugacity of component i in solution
R	Universal gas constant
R_g	Individual gas constant
T	Absolute temperature
P	Total absolute pressure
P_i^{sat}	Saturation pressure of pure component i
x_i	Liquid mole fraction of component i
y_i	Vapor mole fraction of component i
z_i	Initial or feed total mole fraction of component i
φ	Fugacity coefficient
γ	Activity coefficient
V	Volume
V_l	Liquid volume
V_g	Gas (or vapor) volume
MW	Molecular weight
ρ	Density
ρ_l	Liquid density
$\mathscr{K}$	Equilibrium constant (VLE)
$\mathscr{V}$	Vapor total moles (or mole flow)
$\mathscr{L}$	Liquid total moles (or mole flow)
$\mathscr{F}$	Feed total moles (or mole flow)
Q	Heat input
ΔH_{vap}	Heat of vaporization
S	Entropy
L_v	Ostwald coefficient
B_{11}	Second virial coefficient
r	Rate of reaction

Symbol	Explanation
k_r	Reaction rate constant
E_a	Activation energy
$[A]$	Concentration of molecule A
q_{gen}	Heat generation
q_{loss}	Heat loss
ΔH_c	Heat of combustion
h_q	Heat transfer coefficient
A_w	Wall surface area
T_w	Wall temperature
T_{ai}	Autoignition temperature
k	Thermal conductivity
x	Horizontal length
y	Vertical length
L	Characteristic length
T_{ad}	Adiabatic flame temperature
ϕ	Fuel-air equivalence ratio
LFL	Lower Flammability Limit
AFR	Molar air-fuel ratio
u	x-velocity component
v	y-velocity component
g	Gravitational acceleration
ν	Kinematic viscosity
β	Volumetric thermal expansion coefficient
Re	Reynolds number
Pr	Prantl number
Gr	Grashof number
η	Ostrach similarity parameter
ψ	Stream function
D	Diameter
T_{bp}	Boiling point temperature
T_{fp}	Flash point temperature
λ	Wavelength
c	Speed of light in vacuum
h	Universal Planck constant
k_B	Boltzmann constant
σ	Stefan-Boltzmann constant
$L_{\lambda,b}$	Black body spectral radiance
E	Emittance (emissive power)
E_λ	Spectral emittance (emissive power)
ε	Emissivity
ε_λ	Spectral emissivity

Symbol	**Explanation**
$\Delta\varphi$	Optical phase difference
n	Refractive index
K	Gladstone-Dale constant
Da	Damkohler number
τ_{flow}	Flow timescale
τ_{chem}	Chemical reaction timescale

1 Theory

1.1 Vapor Liquid Equilibrium

Vapor liquid equilibrium (VLE) is an important concept in many disciplines, including chemical engineering, mechanical and aerospace engineering. It is especially relevant for the production, treatment and handling of hydrocarbon fuels, and is treated extensively in the literature [1]–[3].

The vapor and liquid phases are at equilibrium when the following criteria are met:

1. The pressure is equal in both phases (mechanical equilibrium).
2. The temperature is equal in both phases (thermal equilibrium)
3. The chemical potential is the same in both phases (chemical equilibrium)

The last criteria (3) can be expressed as:

$$\mu_i^l = \mu_i^v \tag{1.1}$$

Where μ_i^l and μ_i^v are the chemical potentials of component i in the liquid and vapor phase, respectively. The chemical potential is found by

$$\mu_i = G_i + RT \ln(\hat{f}_i / f_i) \tag{1.2}$$

where G_i is the molar Gibbs free energy of pure i in its real physical state (gas, liquid or solid), f_i is the fugacity of the pure species i, and $\hat{f}_i$ is the fugacity of species i in solution. Equation 1.2 is valid for both phases. As the reference G_i is equal for both phases of a pure component, the chemical equilibrium condition (3) is fulfilled when the fugacities of solution in both phases are equal:

$$\hat{f}_i^l = \hat{f}_i^v \tag{1.3}$$

It is customary to define the the fugacity coefficients [1]:

$$\varphi_i \equiv \frac{f_i}{P} \qquad \varphi_i^{sat} \equiv \frac{f_i^{sat}}{P_i^{sat}} \qquad \hat{\varphi}_i \equiv \frac{\hat{f}}{y_i P} \tag{1.4}$$

as well as the activity coefficient γ_i to account for the non-ideality of the liquid phase with concentration

$$\gamma_i \equiv \frac{\hat{f}_i}{x_i f_i} \tag{1.5}$$

The fugacity of the individual components in the vapor phase mixture is then

$$\hat{f}_i^v = \hat{\varphi}_i y_i P \tag{1.6}$$

and the fugacity of the individual components in liquid phase solution can be found from

$$\hat{f}_i^l = \gamma_i x_i \varphi_i^{sat} P_i^{sat} \exp\left[\frac{V_i^l (P - P_i^{sat})}{RT}\right] \tag{1.7}$$

where V_i^l is liquid-phase molar volume for the saturated liquid, and P_i^{sat} is the vapor pressure of the pure component at saturation. Setting the solution fugacities equal to one another gives the criteria for vapor-liquid equilibrium

$$\hat{\varphi}_i y_i P = \gamma_i x_i \varphi_i^{sat} P_i^{sat} \exp\left[\frac{V_i^l (P - P_i^{sat})}{RT}\right] \tag{1.8}$$

The exponential expression is the Poynting factor, and is close to unity at low to moderate pressures. At low pressures, where the ideal gas law is valid, the fugacity coefficients are also close to unity. If the molecules in liquid solution are also similar enough to be approximated as ideal, the expression reduces to Raoult's law [1]:

$$y_i P = x_i P_i^{sat} \tag{1.9}$$

This form is a good approximation for mixtures of similar molecules at low pressure [1]. The vapor pressure is a function of temperature, and can be found from vapor pressure correlations (see Section 1.1.3). If the liquid mole fractions are known, by summing the vapor fractions ($\sum y_i = 1$), this equation can be solved explicitly for pressure given the temperature to find the bubble point pressure, or implicitly to find the boiling point, T_{bp}. Similarly, for a given vapor composition, by summing the liquid fractions ($\sum x_i = 1$), the

equation can be solved explicitly for the dew point pressure given the temperature, or implicitly for the dew temperature T_{dew} given the pressure.

For convenience, the equilibrium ratio can be defined as

$$\mathcal{K}_i = \frac{y_i}{x_i} \tag{1.10}$$

And when Raoult's law holds

$$\mathcal{K}_i = \frac{P_i^{sat}}{P} \tag{1.11}$$

The vapor-liquid equilibrium of a binary ideal mixture of hydrocarbons can be solved and visualized graphically by constructing a bubble and dew point line, defined in terms of pressure or temperature. At constant pressure, the dew point temperature will be above the bubble point temperature. At constant temperature, the bubble point pressure will be above the dew point pressure. A two-phase equilibrium may exist in the region between the bubble and dew point.

1.1.1 Non-condensable gases

Non-condensable gases are species that are above the critical point at the relevant system pressure and temperature. If the system contains species that are non-condensable, such as air, the dew temperature is decreased. They will not condense, but a small fraction may exist in the liquid phase as dissolved gas. When the system is considered as a whole, including non-condensable gases in the vapor space, the dew point temperature is decreased, and the region between the dew and bubble point is no longer meaningful for calculating the VLE.

When a liquid of known initial composition is injected into an enclosed volume containing a non-condensable gas (such as air at atmospheric conditions), the solution strategy depends on the ratio of liquid volume to available vapor space. There are essentially three different cases:

1. The liquid volume is very large compared to the available vapor space ($V_l >> V_g$). The volume evaporated is very small compared to the liquid volume, so the change in composition due to evaporation can be neglected. The composition of the liquid phase is essentially unchanged and the vapor phase composition can readily be found from Raoult's law assuming ideality.

2. The vapor space volume is very large compared to the liquid volume ($V_g >> V_l$). All liquid will evaporate and no vapor-liquid equilibrium will be reached. For an ideal pure component liquid phase, the condition for this is

$$\frac{V_l}{V_v} < \frac{MWP^{sat}}{\rho_l RT} \tag{1.12}$$

   The condition can also be described in terms of the dew temperature, $T > T_{dew}$, if the vapor composition at complete evaporation can be found. This composition is determined by the total amount of liquid injected and air present. Before total evaporation, the composition as a function of time can be solved as a diffusion mass transfer problem.

3. Intermediate liquid/gas volume ratio. Some, but not all the liquid will evaporate. A vapor-liquid equilibrium is reached, but the phase composition of both phases is heavily dependent on the liquid/gas volume ratio. Can be solved as a Raoult's or flash calculation problem taking non-condensable gases into account.

1.1.2 Flash calculation

Flash calculations solve for the vapor and liquid composition in a single equilibrium stage, typically given the state of the input stream, the system pressure, and additional information to specify the system. Common assumptions are constant pressure and temperature (P,T-flash), or adiabatic ($Q = 0$) or constant heat duty operation [1], [4]. An illustration of a single equilibrium stage phase separator (flash drum) is shown in Figure 1.1. In the vessel, the vapor and liquid are assumed to be in equilibrium.

For a system of known pressure, temperature, mole (or mass), and initial composition, the vapor liquid split and composition can be found by combining the mole balances and the equilibrium ratio for each component [1]:

$$\sum_i \frac{\mathscr{F} z_i \mathscr{K}_i}{\mathscr{F} + \mathscr{V}(\mathscr{K}_i - 1)} = 1 \tag{1.13}$$

where z_i is the inlet (or initial) composition of component i, $\mathscr{F}$ is the moles of feed, and $\mathscr{V}$ is the moles of vapor. For a basis of one mole feed ($\mathscr{F} = 1$),

$$\sum_i \frac{z_i \mathscr{K}_i}{1 + \mathscr{V}(\mathscr{K}_i - 1)} = 1 \tag{1.14}$$

This equation must be solved implicitly for $\mathscr{V}$, and is therefore commonly recast as a monotonic function of $\frac{\mathscr{V}}{\mathscr{F}}$ and solved for $\frac{\mathscr{V}}{\mathscr{F}}$ using root-finding methods such as Newton-Raphson. This form was first proposed by Rachford and Rice [5]:

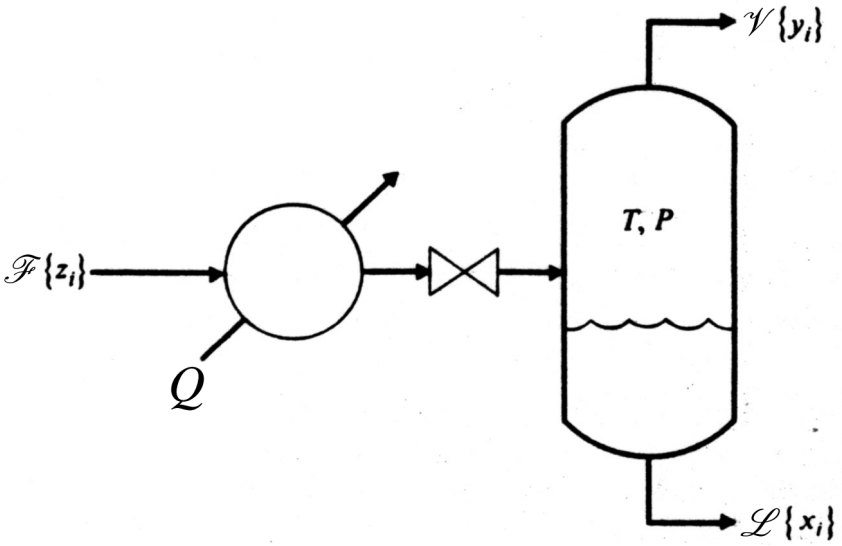

Figure 1.1: Single equilibrium stage phase separator (flash drum).

$$\sum_i \frac{z_i(\mathscr{K}_i - 1)}{1 + \frac{\mathscr{V}}{\mathscr{F}}(\mathscr{K}_i - 1)} = 0 \tag{1.15}$$

When a non-condensable gas is present in the system, a division-by-zero issue arises when calculating $\mathscr{K}_{nc}$ because $x_{nc} = 0$. This can be avoided by dividing by $(\mathscr{K}_i - 1)$ and taking the limit as $x \to 0$ to obtain [6]:

$$\sum_i \frac{z_i}{1/(\mathscr{K}_i - 1) + \frac{\mathscr{V}}{\mathscr{F}}} + \frac{z_{nc}}{\frac{\mathscr{V}}{\mathscr{F}}} = 0 \tag{1.16}$$

where z_i is the inlet (or initial) composition of component i, and $\mathscr{V}$ is the moles of vapor, both including non-condensable gases in the feed, and z_{nc} is the inlet (or total) mole fraction of non-condensable gas. Although this method is developed on the basis of a flowing system, the equilibrium conditions and material balances are also applicable to non-flowing systems. In cases where the solubility of non-condensable gases is important, the liquid composition of the gases in the liquid can be found by empirical coefficients, as will be discussed in Section 1.2.

1.1.3 Vapor pressure correlations

The pure component vapor pressure (P_i^{sat}) as a function of temperature can be found from experimental correlations.

When the vapor pressure at one temperature and the heat of vaporization is known and approximately constant, the effect of temperature on the vapor pressure can be estimated by the Clausius-Clapeyron equation

$$\ln\left(\frac{P_1^{sat}}{P_2^{sat}}\right) = \frac{\Delta H_{vap}}{R}\left(\frac{1}{T_2} - \frac{1}{T_1}\right) \tag{1.17}$$

where P_1^{sat} and P_2^{sat} are the vapor pressures at different states, ΔH_{vap} is the heat of vaporization, and T_1 and T_2 are the absolute temperatures at the different states.

High-accuracy correlations are based on finding curve fit parameters to match experimental data. The classic Antoine equation is a semi-empirical correlation on the form

$$\log_{10} P^{sat} = A - \frac{B}{C+t} \tag{1.18}$$

where t is the temperature (in °C), and A, B and C are experimental constants.

For higher accuracy over a broader range of T, the more recent DIPPR 101 Equation [7], [8] can be used

$$P^{sat} = \exp(A + \frac{B}{T} + C\ln T + DT^E) \tag{1.19}$$

where P^{sat} is the vapor pressure in Pascal, T is the absolute temperature in Kelvin, and A, B, C, D and E are compound-specific curve fitting parameters from the DIPPR 801 database. This correlation was used in this work, and selected parameters relevant for the surrogates used in this work are compiled in Table 4.1.

1.2 Solubility of light gases in hydrocarbons

Knowledge about the solubility of gases is important for design of fuel systems and their components [9].

The degree of solubility can change the flammability limits. At sea level temperature and pressure, jet fuel can contain dissolved air (oxygen and nitrogen). For the same partial pressure, oxygen is more soluble than nitrogen (higher Ostwald coefficient), and solubility is proportional to pressure. Consequently, as pressure decreases with altitude, the vapor space becomes enriched with oxygen. This will increase flammability on the rich side, although the lower limit is virtually unchanged [9].

Solubility, like any other thermodynamic process, will only occur spontaneously if the Gibbs free energy is negative.

$$\Delta G_{sol} = \Delta H_{sol} - T\Delta S_{sol} < 0 \tag{1.20}$$

Where ΔG_{sol} is the change in Gibbs free energy, ΔH_{sol} is the change in enthalpy, and ΔS_{sol} is the change in entropy.

The dissolution process can be described as three steps:

1. Breaking solute-solute attractions. Endothermic $\Delta H_{AA} > 0$
2. Breaking solvent-solvent attractions. Endothermic $\Delta H_{BB} > 0$
3. Forming solute-solvent attractions. Exothermic $\Delta H_{AB} < 0$

The total change is then:

$$\Delta H_{sol} = \Delta H_{AA} + \Delta H_{BB} + \Delta H_{AB} \tag{1.21}$$

Where A signifies the solute and B signifies the solvent. ΔH_{AA} is the change in enthalpy from breaking solute-solute attractions, ΔH_{BB} is the change in enthalpy from breaking solvent-solvent attractions, and ΔH_{AB} is the change in enthalpy from forming solvent-solute attractions [10].

For gases dissolving in liquid, the entropy decreases $\Delta S_{sol} < 0$. Thus, for ΔG_{sol} to be negative, the solution process must be exothermic $\Delta H_{sol} < 0$.

We see from Equation 1.20 that as T increases, the entropy term becomes larger and ΔG_{sol} becomes less negative (weaker).

The effect of temperature on solubility can also be predicted by Le Chatelier's principle:

> If the equilibrium of a system is disturbed by a change in one or more of the determining factors (as temperature, pressure, or concentration) the system tends to adjust itself to a new equilibrium by counteracting as far as possible the effect of the change [11].

This can be seen from the dissolution reaction, e.g. for nitrogen gas dissolving in water:

$$\begin{aligned} \text{solute}\,(\text{g}) + \text{solvent}\,(\text{l}) &\rightleftharpoons \text{solute}\,(\text{aq}) + \text{solvent}\,(\text{aq}) + \text{heat} \\ \text{N}_2\,(\text{g}) + \text{H}_2\text{O}\,(\text{l}) &\rightleftharpoons \text{N}_2\,(\text{aq}) + \text{H}_2\text{O}\,(\text{aq}) + \text{heat} \end{aligned}$$

If the solution process is exothermic, added heat (increased temperature) will decrease the solubility. The equilibrium is shifted to the left. Conversely, if the process is endothermic, added heat will increase solubility. The equilibrium is shifted to the right.

Gases have very weak intermolecular attraction. Ideal gases have, by definition, no intermolecular forces at all. Thus, the energy required to break these bonds are negligible ($\Delta H_{AA} \approx 0$). For polar liquid solvents, such as water, the solvent-solvent attractions are very strong due to hydrogen-bonding. However, polar solvents generally also make stronger solute-solvent bonds, and the energy released from the formation of these bonds is higher than those required to break solvent-solvent bonds, $\Delta H_{AB} > \Delta H_{BB}$. As a result, the dissolution of gases in polar compounds is exothermic, and solubility decreases with temperature according to Le Chatelier's principle.

For organic liquid solvents, such as hydrocarbon fuels, the solvent-solvent attractions are weaker, and so is the solute-solvent bonds. Often, the solute-solvent bond is so weak that $\Delta H_{AB} < \Delta H_{BB}$ and the net process is endothermic ($\Delta H_{sol} > 0$). Thus, for organic solvents, gas solubility often increases with temperature.

For both polar and non-polar solvents, the solubility tends towards zero as the temperature approaches saturation (the boiling point for pure compounds).

Gas solubility in polar solvents generally decreases with temperature, while it can increase or decrease with temperature in organic solvents, depending on the relative strength of attractions. As an example, the solubility of carbon dioxide (CO_2) in Jet A decreases with temperature, while solubility of oxygen (O_2) and nitrogen (N_2) increases in the same temperature range.

The solubility of light gases, such as nitrogen, oxygen, carbon dioxide etc., can be characterized in several ways; the most widely used are Henry's constants, Ostwald coefficients, or mole fractions at a given temperature and pressure [12].

1.2.1 Ostwald coefficient

The Ostwald coefficient can be defined as:

$$L_v = (V_g / V_l)_{equil} \tag{1.22}$$

Where L_v is the Ostwald coefficient and V_g is the volume of gas dissolved by the volume V_l of pure liquid (no gas), both measured at equilibrium at the specified temperature.

If we have ideal gas behavior and Henry's law holds, the Ostwald coefficient is independent of the partial pressure of the gas [13]. Battino et al. [12] recommend the use of Ostwald coefficients over Henry's constants to describe solubility.

Figure 1.2 shows the solubility (Ostwald coefficient) of oxygen and nitrogen in Jet A as a function of temperature.

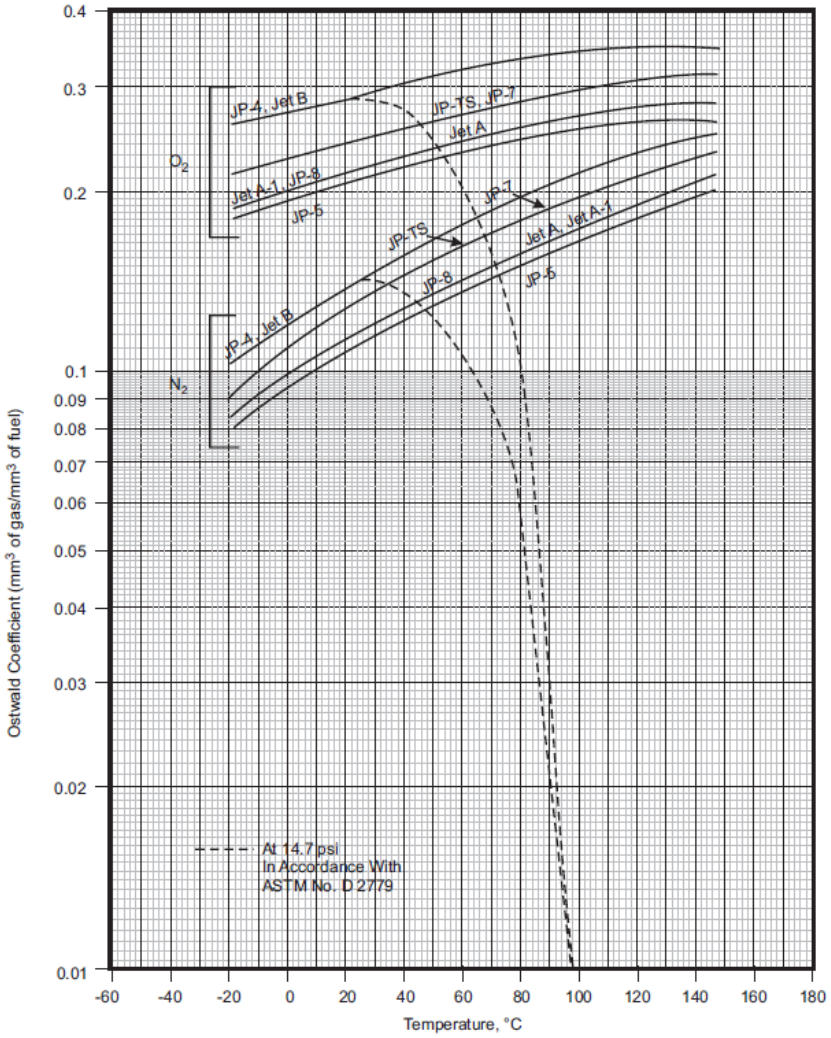

Figure 1.2: Solubility (Ostwald coefficient) of O_2 and N_2 in jet fuel as a function of temperature [9].

Figure 1.3 shows the solubility (Ostwald coefficient) of carbon dioxide in jet fuel as a function of temperature.

Ostwald coefficient data can be converted to mole fraction of gas dissolved in the liquid at equilibrium using the equation:

$$x_1 = [\frac{1}{V_l L_v}(\frac{RT}{P_1} + B_{11}) + 1]^{-1} \tag{1.23}$$

Where x_1 is the mole fraction of gas dissolved at equilibrium, R is the universal gas

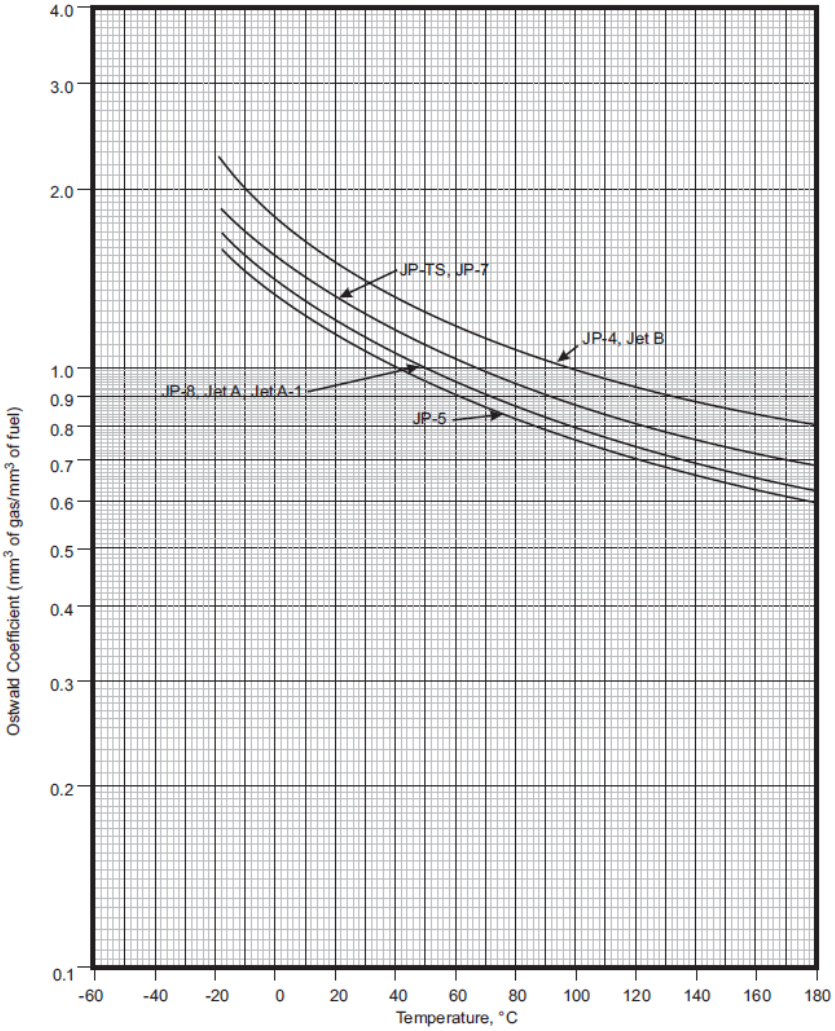

Figure 1.3: Solubility (Ostwald coefficient) of CO_2 in jet fuel as a function of temperature [9].

constant, T is the temperature (in Kelvin), P_1 is the pressure, and B_{11} is the second virial coefficient of the gas of interest.

1.3 Reaction kinetics

Combustion of hydrocarbons can in simple terms be thought of as the breakdown of the fuel all the way down to carbon monoxide (CO), followed by the oxidation of CO into CO_2. For this reason, the kinetics of (CO) oxidation is very important for the combustion of any hydrocarbon. The common reactions for CO oxidation are [14]:

$$\begin{aligned} CO + O_2 &\longrightarrow CO_2 + O^\bullet \\ O + H_2O &\longrightarrow OH^\bullet + OH^\bullet \\ CO + OH^\bullet &\longrightarrow CO_2 + H^\bullet \\ H + O_2 &\longrightarrow OH^\bullet + O^\bullet \end{aligned}$$

The oxidation of CO is accelerated by the presence of hydrogen-containing species, such as H_2O or H_2, because the hydroxyl radical (OH) step proceeds at a much higher rate than the others. In fact, the first step is too slow to serve as a significant source of CO_2, and is rather an initiating source of oxygen radicals for the subsequent production of OH-radicals.

High temperature oxidation of alkanes with more than three carbons is essentially governed by thermal cracking (pyrolysis) of the fuel, with the following steps (using propane as an example) [14], [15]:

1. **(Initialization) C-C fission**: At high temperatures, a C-C bond in the alkane structure is broken (the C-C bond is weaker than the C-H bond), and the alkane is split into two alkyl radicals (M signifies a third body).

$$C_3H_8 + M \longrightarrow C_2H_5{}^\bullet + CH_3{}^\bullet + M$$

2. **H-atom abstraction:** The alkyl radicals form a double bond, creating an olefin (e.g ethylene) and a hydrogen radical.

$$C_2H_5{}^\bullet + M \longrightarrow C_2H_4 + H^\bullet + M$$

3. The hydrogen radicals react with oxygen to form a pool of OH-radicals.

$$H^\bullet + O_2 \longrightarrow O^\bullet + OH^\bullet$$

4. The radicals attack the alkane molecules to produce more alkyl radicals.

$$\begin{aligned} C_3H_8 + H^\bullet &\longrightarrow C_3H_7{}^\bullet + H_2 \\ C_3H_8 + OH^\bullet &\longrightarrow C_3H_7{}^\bullet + H_2O \\ C_3H_8 + O^\bullet &\longrightarrow C_3H_7{}^\bullet + OH^\bullet \end{aligned}$$

These alkyl radicals will again decompose to olefins (e.g propylene) and H-radicals via H-atom abstraction as in step 2, or via β-scission as described in the next step.

5. **β-scission**: A C-C or C-H bond one place away from the radical site is broken. This is because the bond adjacent to the radical site is strengthened by the by the unpaired electron, but the subsequent bond is weakened as a result. Depending on the position of the radical, a C-C or C-H bond may be broken.

$$C_3H_7^\bullet + M \longrightarrow C_3H_6 + H^\bullet + M$$
$$C_3H_7^\bullet + M \longrightarrow C_2H_4 + CH_3^\bullet + M$$

6. **Oxidation**: The olefins are attacked by oxygen radicals and produce formyl radicals and formaldehyde:

$$C_3H_6 + O^\bullet \longrightarrow C_2H_5^\bullet + HCO^\bullet$$
$$C_3H_6 + O^\bullet \longrightarrow C_2H_4 + C_2CO$$

   Subsequently, methyl radicals, formaldehyde, methylene (CH_2) and CO also oxidizes, with the majority of heat release resulting from the oxidation of CO.

Variations of these steps are found to be governing also for higher carbon number n-alkanes, such as n-decane or n-dodecane. The role of cracking in n-dodecane combustion was studied in detail by You et al. [16], and the important steps were found to be: C-C fission, H-atom abstraction from primary or secondary C atoms by radicals (H, O, OH, O_2, CH_3), mutual isomerization of alkyl radicals, β-scission to produce olefins and alkyl radicals, H-atom abstraction from alkenes, and decomposition of n-alkenyl radicals. The fuel conversion was found to be limited by C-C fission and H-abstraction by H and CH_3, whereas β-scission of alkyl radicals was not rate-limiting [16].

Another more recent study by Banerjee et al. [17] showed that for atmospheric pyrolysis of n-dodecane at 1000 K and 1050 K rich oxidation produce ethylene and propane as the main products, followed by methane and 1-C_4H_8. At these temperatures, the formation of alkyl radicals occured mainly from H-abstraction reactions, although C-C fission could be limiting at temperatures above 1400 K. In the flow reactor, the reaction then proceeded through β-scission of alkyl radicals. Large alkanes form alkenyl radicals though H-abstraction, or H-addition rection and subsequent β-scission to form smaller molecules. The alkyl radicals were also shown to undergo mutual isomerization at β-scission. The total residence time was approximately 40 ms.

1.3.1 Arrhenius rate law

Elementary reactions in combustion are most commonly bimolecular reactions on the form [14]:

$$\mathrm{A} + \mathrm{B} \longrightarrow \mathrm{C} + \mathrm{D}$$

These are generally second order reactions where the reaction rate is proportional to the reactant concentrations:

$$r = -k_r[A][B] \tag{1.24}$$

Where $r = \frac{d[A]}{dt}$ is the reaction rate (here expressed with respect to reactant A, hence the negative sign), $[A]$ is the concentration of molecule A, $[B]$ is the concentration of molecule B, and k_r is the rate coefficient. The reaction rate coefficient can be expressed by the empirical Arrhenius rate law, here in the modified 3-parameter form:

$$k_r(T) = aT^b \exp\left(\frac{-E_a}{RT}\right) \tag{1.25}$$

Where a, b, are empirical parameters, and E_a is the activation energy, also found from experiment.

1.4 Ignition criteria

Oxidation of hydrocarbons produces heat, and according to the Arrhenius rate law, the reaction rate scales exponentially with temperature. This coupling constitutes a positive feedback loop that is self-sustaining over a threshold temperature and sufficient reactants present. This thermal runaway is called ignition.

An often-used criteria for ignition is thus that the rate of heat generation from the reactions exceed the losses to the surroundings [14]:

$$q_{gen} > q_{loss} \tag{1.26}$$

For simplified modeling purposes, the global reaction rate is expressed by Arrhenius' law and for a bimolecular reaction in a volume of homogeneous concentration and temperature, the heat released scales with volume as:

$$q_{gen} = V\Delta H_c[A][B]k_r T^b \exp\left(\frac{-E_a}{RT}\right) \tag{1.27}$$

Where V is the volume, and ΔH_c is the heat of combustion (convention: positive for exothermic reaction). This form is simplified as it models only the global reaction kinetics. Actual fuels react by a set of complicated elementary reaction pathways, as discussed in 1.3.

1.4.1 Autoignition

A simplified method of predicting the autoignition temperature (AIT, T_{ai}) based on thermal theory is given by Chomiak [18]. For a quiescent fluid in an enclosed solid container where the wall temperature is below the gas temperature, the losses can be expressed as

$$q_{loss} = h_q A_w (T - T_w) \tag{1.28}$$

where h_q is the heat transfer coefficient from the gas to the walls, and A_w is the wall surface area. At this point, the rate of change with temperature is also equal

$$q_{gen} = q_{loss} \tag{1.29}$$

$$\left(\frac{\partial q_{gen}}{T}\right)_{T_{ai}} = \left(\frac{\partial q_{loss}}{T}\right)_{T_{ai}} \tag{1.30}$$

Substituting in the expressions for q_{gen}, q_{loss} in these conditions and solving for T_{ai} (note that the simplified Arrhenius' law is used):

$$V \Delta H_c [A][B] k_r \exp\left(\frac{-E_a}{R T_{ai}}\right) = h_q A_w (T_{ai} - T_w) \tag{1.31}$$

$$T_{ai} = \frac{E_a}{2R}\left[1 - \left(1 - 4R\frac{T_w}{E_a}\right)^{1/2}\right] \tag{1.32}$$

$$T_{ai} \approx T_w + \frac{R}{E_a} T_w^2 \tag{1.33}$$

However, as the activation energies of hydrocarbon combustion reactions generally are very large [14], Equation 1.33 implies that the autoignition temperature of most hydrocarbons are similar, and within ± 10 K of surrounding temperature required for slow reaction

$T \approx T_w$ [18]. This is not in agreement with experimental data [19]. Thus, simple thermal theory is limited to a qualititive description of the phenomena at best. Although more accurate predictive methods exist [20][21], autoignition temperatures for hazard assessment are based on experimental data, and are dependent on the experimental apparatus and a multitude of other factors.

1.4.2 Hot surface ignition

For a fluid moving over a hot surface, where the wall temperature is higher than the fluid temperature, the ignition criterion of Equation 1.26 can be expressed as the point when the heat flow is reversed. This occurs when the reaction heat generation has overcome the losses to the surroundings and increased the temperature above that of the hot surface walls [18]. This is also known as the Van't Hoff ignition criterion. This criterion has been verified for most cases, but is not valid for constant heat flux or wall temperatures close to the adiabatic flame temperature [22].

$$\left(\frac{dT}{dy}\right)_w = 0 \tag{1.34}$$

At stagnant conditions, assuming conduction is the dominant mode of heat transfer, the energy equation is:

$$k\frac{d^2T}{dy^2} + \Delta H_c r(T) = 0 \tag{1.35}$$

Integration from $y = 0$ to $y = L$ and $T = T_w$ to $T = T_0$ gives

$$\frac{dT}{dy} - (\frac{dT}{dy})_w = \left(\frac{2\Delta H_c}{k}\int_{T_0}^{T_w} r(T)dT\right)^{1/2} \tag{1.36}$$

Substituting in the Frank-Kamenetskii approximation:

$$\exp\left(\frac{-E_a}{RT}\right) \approx \exp\left(\frac{-E_a}{RT_w}\right)\exp\left(-E_a\frac{T_w - T}{RT_w^2}\right) \tag{1.37}$$

integrating again and using the Van't Hoff ignition criteria yields

$$\left(\frac{dT}{dy}\right)_{ign} \approx \left(\frac{2\Delta H_c}{k}r(T_w)\frac{RT_w^2}{E_a}\left[1 - \exp(-E_a\frac{T_w - T}{RT_w^2})\right]\right)^{1/2} \tag{1.38}$$

The expression in square brackets is on the order of unity and the reaction zone thickness [18], so the following approximation can be made

$$\left(\frac{T_w - T_\infty}{L}\right)^2_{ign} \approx \frac{2\Delta H_c}{k} r(T_w) \frac{RT_w^2}{E_a} \tag{1.39}$$

As with Equation 1.33, this approximation is not useful for quantitative results, but can indicate the effects of parameters such as characteristic length and wall temperature on ignition.

1.5 Reaction equilibrium and thermodynamics

The theoretical maximum temperature obtained from combustion with no heat loss is called the adiabatic flame temperature (T_{ad}) and is an important combustion property. This temperature depends on whether the combustion is completed under constant pressure or constant volume. As no work is done under the constant volume process, the adiabatic flame temperature is higher for constant volume processes. Combustion that is open to the atmosphere is generally modeled as a constant pressure process, whereas in a closed combustion chamber, the volume is held constant and the pressure increases.

The adiabatic flame temperature is also highly dependent of the heat of combustion and heat capacity. It increases with heat of combustion, but decreases with increased heat capacity. The adiabatic flame temperature is generally at a maximum slightly on the rich side of stoichiometric (at an equivalence ratio of $\phi \approx 1.05$). This is because the heat capacity decreases more rapidly than the heat of combustion between $\phi = 1$ and $\phi(T_{max})$ [14].

Equilibrium dissociation also affects the temperature and pressure of real combustion. The major species CO_2 and H_2O both dissociate according to:

$$\begin{aligned} CO_2 &\rightleftharpoons CO + \frac{1}{2}O_2 \\ H_2O &\rightleftharpoons H + OH \end{aligned}$$

The dissociation of CO_2 and H_2O is significant even at stoichiometric conditions. 11.7 % of CO_2 and 4.3 % of H_2O is dissociated for stoich propane-air combustion [14]. Because these reactions produce a net increase of total moles in the forward direction, the degree of dissociation generally decreases with pressure, as predicted by Le Chatelier's principle.

At rich conditions CO is formed, and may react to CO_2 and H_2 though the Water-Gas Shift reaction (WGS):

$$CO + H_2O \rightleftharpoons H_2 + CO_2 + \text{heat}$$

The WGS reaction is endothermic ($\Delta H = -41.1\,\text{kJ}\,\text{mol}^{-1}$) in the forward direction (H_2 production). According to Le Chatelier's principle, the reaction will therefore shift to the left at higher temperatures. At post combustion equilibrium at high temperatures, a significant part of the energy is also taken up by dissociated species such as hydrogen.

$$H_2 \rightleftharpoons 2\,H$$

Due to the sheer number of minor species and elementary reactions involved, accurate predictions of real combustion processes require computer software. Common chemical equilibrium solvers include STANJAN, CHEMKIN, Cantera, CEA, and FlameMaster. Many of these equilibrium solvers are based on the element potential method, and the relevant fuel kinetics are provided by kinetic models for the fuels in question. Improving and updating these models with accurate kinetics is an ongoing area of research. Example models that are relevant for this work include JetSurf2.0 [23], AramcoMech3.0 [24], and PolimiKerosene [25], [26]. These models provide the chemical kinetics data for n-alkanes up to dodecane and other common jet fuel compounds as described in 2.1. In this work, the models were used with the Cantera [27] software package in Python.

Figure 1.4 shows the constant volume adiabatic flame temperature as a function of equivalence ratio for ethylene (IUPAC: ethene), n-hexane and n-dodecane, calculated in Cantera using JetSurf2.0 at an initial temperature and pressure of $300\,\text{K}$ and $101.3\,\text{kPa}$, respectively. Figure 1.5 shows the constant volume combustion pressure at the same conditions. The stoichiometric reactions for these species are:

$$\begin{aligned} C_2H_4 + 3\,(O_2 + 3.76\,N_2) &= 2CO_2 + 2H_2O + 11.28N_2 \\ C_6H_{14} + 9.5\,(O_2 + 3.76\,N_2) &= 6CO_2 + 7H_2O + 35.72N_2 \\ C_{12}H_{26} + 18.5\,(O_2 + 3.76\,N_2) &= 12CO_2 + 13H_2O + 69.56N_2 \end{aligned}$$

On the lean side, the effects of dissociation are negligible, and the adiabatic flame temperature is determined by the ratio of heat release and heat capacity. Hexane and dodecane

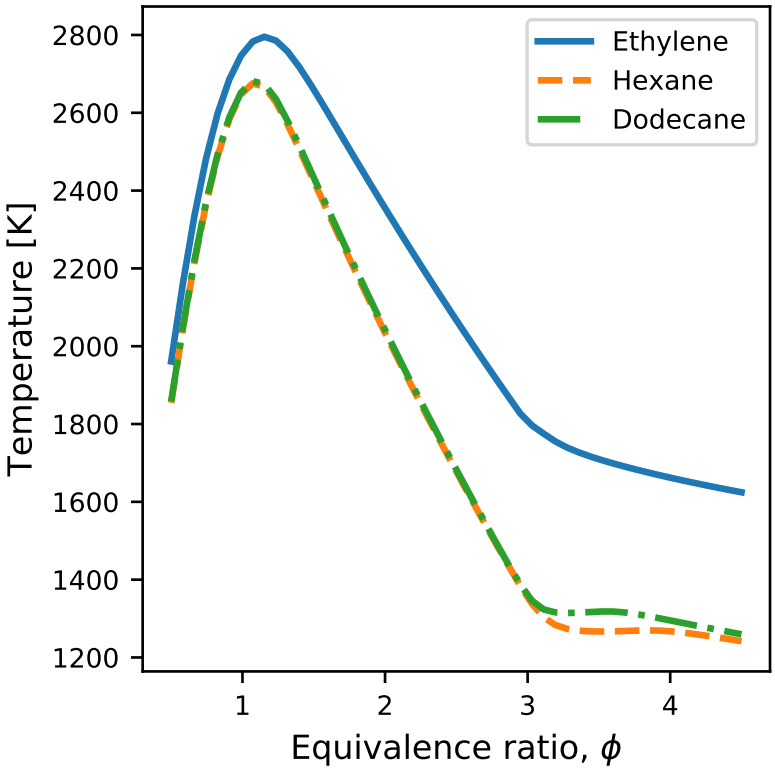

Figure 1.4: Constant volume adiabatic flame temperature vs. equivalence ratio for pure ethylene, hexane and dodecane. Calculated in Cantera using JetSurf2.0 at an initial temperature and pressure of 300 K and 101.3 kPa, respectively.

are both high carbon number (n) alkanes with similar H/C-ratios ($\frac{2n+2}{n}$). The combustion energetics are largely determined by the H/C-ratio. Thus, the lean side is almost identical. On the rich side ($\phi > 1$) some deviation can be seen due to slight differences in dissociation and water gas shift equilibrium. Above $\phi \approx 3$, there is no more water available for WGS, and the temperature and pressure decrease with ϕ flattens out. Figure 1.6 shows the evolution of the WGS reaction species as a function of equivalence ratio for n-dodecane combustion at the same conditions as Figure 1.4 and 1.5.

1.6 Le Chatelier's mixing rule

The flammability limits of a mixture of flammable gases can be estimated based on the limits of each individual species by Le Chatelier's [28] mixing rule

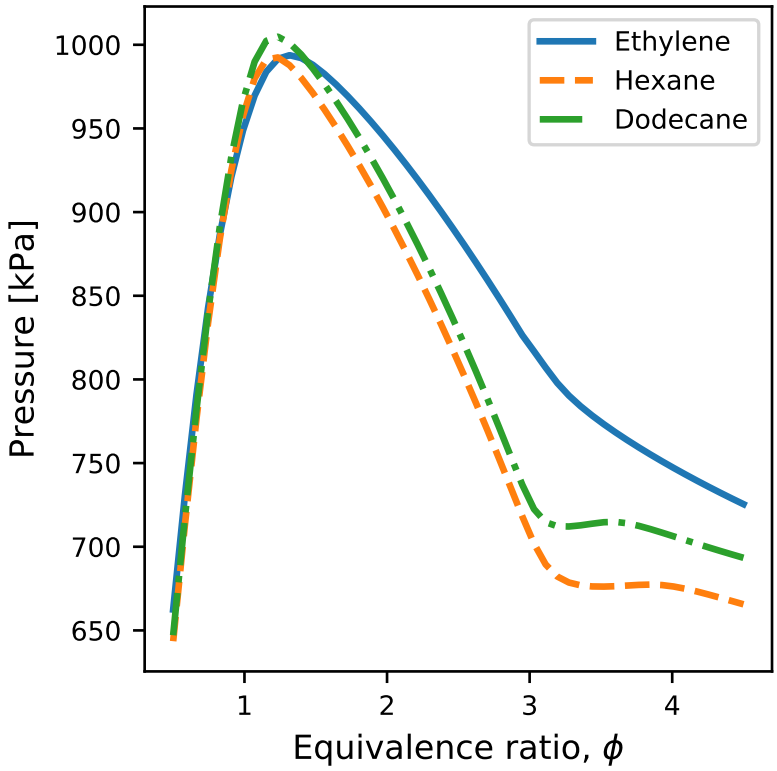

Figure 1.5: Constant volume adiabatic combustion pressure vs. equivalence ratio for pure ethylene, hexane and dodecane. Calculated in Cantera using JetSurf2.0 at an initial temperature and pressure of 300 K and 101.3 kPa, respectively.

$$LFL_{mix} = \frac{1}{\sum \frac{y_i}{LFL_i}} \tag{1.40}$$

where LFL_{mix} is the lower flammability limit of the fuel mixture, y_i is the mole fraction of component i in the fuel mixture (considering only flammable species), and LFL_i is the lower flammability limit of component i.

This form was originally presented by Le Chatelier as an empirical rule, and was later shown by Mashuga and Crowl [29] to be a special form of the calculated adiabatic flame temperature (CAFT) method [30]–[33] under the assumption of constant moles of gas, constant product heat capacities, constant pure species combustion kinetics, and equal adiabatic temperature rise at the flammability limit for each species. For lean hydrocarbon mixtures hydrocarbon-air mixtures at atmospheric conditions, these assumption result in good estimations for the lower flammability limit. An equivalent form of Equation 1.40

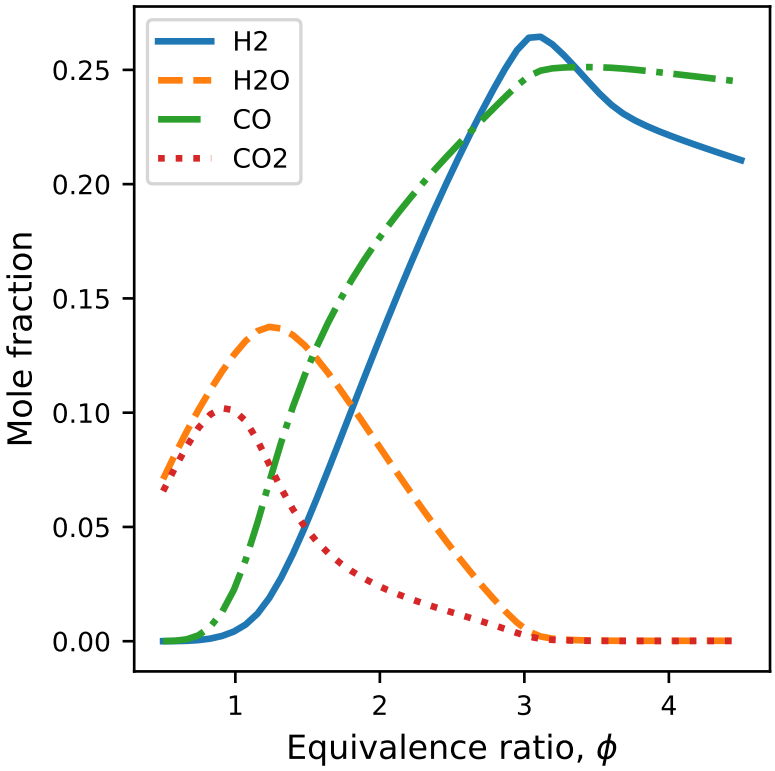

Figure 1.6: Water-gas shift reaction species vs. equivalence ratio for constant volume adiabatic combustion of n-dodecane. Calculated in Cantera using JetSurf2.0 at an initial temperature and pressure of 300 K and 101.3 kPa, respectively.

can also be employed for calculation of the upper flammability limit (UFL), albeit at lower accuracy [29].

1.7 Natural convection boundary layer flow

Free convection is the motion of a fluid due to buoyancy forces. Buoyancy forces can be induced by gradients in temperature, and therefore density, combined with a body force, such as gravity, acting on the medium. This is relevant for the cylinder heating device utilized for the hot surface ignition experiments in this work.

Following the the treatment of Bergman et al. [34], consider a vertical hot surface with a quiescent fluid outside of the boundary layer. Assuming the boundary layer assumptions to be valid, 2-D, steady-state, non-reacting fluid with constant properties, and a vertically

oriented surface with the gravity vector in the negative x-direction (downwards), the governing x-momentum equation is represented by:

$$u\frac{\partial u}{\partial x}+v\frac{\partial v}{\partial y}=-\frac{1}{\rho}\frac{dp_\infty}{dx}-g+\nu\frac{\partial^2 u}{\partial y^2} \tag{1.41}$$

where u is the fluid velocity in the x-direction (vertical), v is the fluid velocity in the y-direction (horizontal), ρ is the fluid density, g is the acceleration of gravity, ν is the kinematic viscosity, and $\frac{dp_\infty}{dx}$ is the pressure change with x outside of the boundary layer. For a quiescent fluid, and opposing the gravity vector, this is the hydrostatic pressure gradient, and can be written as $\frac{dp_\infty}{dx}=-\rho_\infty g$. By simplifying and grouping $\Delta\rho=\rho_\infty-\rho$, we get

$$u\frac{\partial u}{\partial x}+v\frac{\partial v}{\partial y}=g\frac{\Delta\rho}{\rho}+\nu\frac{\partial^2 u}{\partial y^2} \tag{1.42}$$

Further, we invoke the Boussinesq approximation by assuming density differences are only important when multiplied by g and introduce the volumetric thermal expansion coefficient $\beta=-\frac{1}{\rho}(\frac{\partial\rho}{\partial T})_P$ and its approximate form $\beta\approx-\frac{1}{\rho}\frac{\rho_\infty-\rho}{T_\infty-T}$ to get

$$u\frac{\partial u}{\partial x}+v\frac{\partial v}{\partial y}=g\beta(T-T_\infty)+\nu\frac{\partial^2 u}{\partial y^2} \tag{1.43}$$

Including the mass conservation equation (continuity) from the boundary layer assumptions, and the energy conservation equation assuming no heat generation, the governing equations are

$$u\frac{\partial u}{\partial x}+v\frac{\partial v}{\partial y}=0 \tag{1.44}$$

$$u\frac{\partial u}{\partial x}+v\frac{\partial v}{\partial y}=g\beta(T-T_\infty)+\nu\frac{\partial^2 u}{\partial y^2} \tag{1.45}$$

$$u\frac{\partial T}{\partial x}+v\frac{\partial T}{\partial y}=\alpha\frac{\partial^2 T}{\partial y^2} \tag{1.46}$$

where α is the thermal diffusivity. For an ideal gas, $\beta=1/T$. Note that due to the Boussinesq approximation, ρ is omitted and the continuity equation is on a similar form

as for incompressible flow, even though the driving force for flow is the density gradient. By introducing non-dimensional variables

$$x^* \equiv \frac{x}{L} \qquad y^* \equiv \frac{y}{L} \qquad T^* \equiv \frac{T - T_\infty}{T_w - T_\infty}$$

$$u^* \equiv \frac{u}{u_0} \qquad v^* \equiv \frac{v}{u_0}$$

we get

$$u^* \frac{\partial u^*}{\partial x^*} + v^* \frac{\partial v^*}{\partial y^*} = 0 \tag{1.47}$$

$$u^* \frac{\partial u^*}{\partial x} + v^* \frac{\partial v^*}{\partial y^*} = \frac{g\beta(T_w - T_\infty)L}{u_0^2} T^* + \frac{1}{Re_L} \frac{\partial^2 u^*}{\partial y^{*2}} \tag{1.48}$$

$$u^* \frac{\partial T^*}{\partial x^*} + v^* \frac{\partial T^*}{\partial y^*} = \frac{1}{(Re_L)(Pr)} \frac{\partial^2 T^*}{\partial y^{*2}} \tag{1.49}$$

where T_w is the surface wall temperature, L is the length of the surface, and and u_∞ is an arbitrary reference velocity in the "free steam" outside the boundary layer. For pure natural convection, the fluid is quiescent and no logical reference velocity exists, so it is convenient to set it as u_∞ to simplify the T^* coefficient to unity. The Grashof number can then be defined as the square of the Reynolds number:

$$Re_L = \sqrt{g\beta(T_w - T_\infty)L^3/\nu^2} \tag{1.50}$$

$$Gr_L \equiv Re_L^2 \tag{1.51}$$

$$Gr_L \equiv \frac{g\beta(T_w - T_\infty)L^3}{\nu^2} \tag{1.52}$$

The Grashof number Gr describes the ratio of buoyancy to viscous forces, and is as essential to free convection flows as the Reynolds number is for forced convection.

1.7.1 Similarity solution

Equations 1.44-1.46 can be solved as a system with the appropriate boundary conditions. For an isothermal vertical surface in a quiescent fluid, the boundary conditions are:

$$\begin{array}{lll} y = 0 & u = v = 0 & T = T_w \\ y \to \infty & u \to 0 & T \to T_\infty \end{array}$$

This formulation of the problem can also be reduced and solved through the introduction of the Ostrach similarity parameter [35]:

$$\eta \equiv \frac{y}{x}\left(\frac{Gr_x}{4}\right)^{1/4} \tag{1.53}$$

and defining the stream function to represent the velocity components

$$\psi(x,y) \equiv f(\eta)\left[4\nu\left(\frac{Gr_x}{4}\right)^{1/4}\right] \tag{1.54}$$

$$u = \frac{\partial \psi}{\partial y} \tag{1.55}$$

$$v = -\frac{\partial \psi}{\partial x} \tag{1.56}$$

By applying the chain rule, the x-velocity can be expressed as:

$$u = \frac{2\nu}{x} Gr_x^{1/2} f'(\eta) \tag{1.57}$$

The system of partial differential equations can now be reduced to a system of two ordinary differential equations:

$$f''' + 3ff'' - 2(f')^2 + T^* = 0 \tag{1.58}$$

$$T^{*\prime\prime} + 3fPrT^{*\prime} = 0 \tag{1.59}$$

Where the prime signifies differentiation with respect to η. The transformed boundary conditions are:

$$\begin{array}{lll} \eta = 0 & f = f' = 0 & T^* = 0 \\ \eta \to \infty & f' \to 0 & T^* \to 0 \end{array}$$

This system was solved numerically and values of $f'(\eta)$ and T^* vs η tabulated by Ostrach [35].

The analysis outlined in this section is only valid as long as the boundary layer assumptions are valid. The boundary layer approximations are valid if:

$$Gr_x Pr > 10^4 \tag{1.60}$$

And the flow is laminar if:

$$Gr_x Pr < 10^9 \tag{1.61}$$

A cylindrical surface can be approximated as a flat plate if the thickness of the boundary layer is less than or on the order of the cylinder diameter. This has been shown to be the case if [34]:

$$\frac{D}{L} \gtrsim \frac{35}{Gr_L^{1/4}} \tag{1.62}$$

2 Jet fuel

2.1 Commercial jet fuel

Commercial jet fuel (also called turbine fuel) is composed of hundreds of different hydrocarbons, mainly divided into three groups: paraffins, naphtalenes (cycloparaffins), and aromatics. The exact composition varies between regions and refining processes [9].

Paraffins consist of n-alkanes and iso-alkanes. These molecules are single-bonded and saturated with hydrogen, making them stable and less likely to react with metal, paint or elastomer surfaces. The high number of C-H bonds results in a high heating value (energy released per unit weight). Whereas the n-alkane content of aviation gasoline is limited to avoid engine knocking, jet fuel can contain high amounts of n-alkanes [9].

Naphtenes (cycloparaffins) are cyclic alkanes. The ring structure results in a lower hydrogen to carbon (H/C) ratio, and thus a lower heating value. On the other hand, the freezing point of naphtenes is lower than other alkanes of the same carbon number [9].

Aromatics are hydrocarbons containing at least one benzene ring in the structure. The benzene (C_6H_6) ring structure is very stable, and has a very high freezing point. Aromatics have the lowest H/C ratio and heating value of the groups mentioned. They can also form smoke, soot and coke when combusted in jet engines. For these reasons, the volume fraction of aromatics in jet fuel is typically limited to 0.2-0.25, and double-ring naphtalenes at 0.03. Aromatics are known to extract plastisizer in elastomers, and can cause swelling of seals [9].

In addition to the aforementioned groups, jet fuel may also contain trace amounts of hydrocarbons bonded with other atoms such as sulfur, nitrogen or oxygen. Sulfur, or sulfur compounds such as mercaptans, sulfides and disulphides may also be present and can have corrosive effects on internal metal and elastomer. Consequently, total sulfur content is limited in jet fuel specifications. Similarly, naphtenic acids can corrode metals such as aluminium, magnesium and zink [9]. Selected specifications for U.S. commercial jet fuels Jet A and Jet A-1 are shown in Table 2.1. Note that the only difference between Jet A and Jet A-1 is the freezing point specification.

Table 2.1: U.S. Commercial Turbine Fuel Specifications [9]

Property		Jet A	Jet A-1
Aromatics (vol%)	Max	25	25
Naphtalenes (vol%)	Max	3.0	3.0
Sulfur mercaptan (wt%)	Max	0.003	0.003
Total sulfur (wt%)	Max	0.3	0.3
Boiling point (°C)	Max	300	300
Flash point (°C)	Min	38	38
Freezing point (°C)	Max	-40	-47
Density at 15°C ($\mathrm{kg/m^3}$)		775 to 840	775 to 840
Heat of combustion ($\mathrm{MJkg^{-1}}$)	Min	42.8	42.8

2.1.1 Jet fuel ignition

Figure 2.1 shows the autoignition and spark ignition limits for commercial jet fuel as a function of air-fuel ratio at varying temperatures and pressures [36]. The autoignition tests performed using a uniformly heated 18 inch spherical vessel. These tests show autoignition temperatures of 210 °C to 300 °C at atmospheric pressure, depending on the stoichiometry.

When the heat source is a small hot surface, the surface temperature must be considerably higher to cause ignition. Hot surface ignition tests using jet fuel have been conducted and reported as part of the NATO AGARD Advisory Report 132 [37]. For a 15.2 cm diameter cylinder in a 46 cm diameter sphere, the ignition temperature was found to be 310 °C. Similar results were found for flat surfaces. For a smaller cylinder with a diameter of only 3.8 cm, the ignition temperature was 650 °C. Based on these results, the AGARD AR-132 recommends all fuel contact surfaces to be maintained below 240 °C.

Aircraft designs must comply with Title 14, Code of Federal Regulations (14 CFR) 25.981, "Fuel tank explosion prevention". The FAA Advisory Circular (AC) 25.981 outlines safe design guidelines for preventing hot surface ignition and complying with this code [36][38]. AC 25-8 and 25.981-1 define the maximum allowable fuel-contact surface temperature as 22.2 °C below the autoignition temperature. In the same document, the autoignition temperature of Jet A is given as approximately 224 °C to 232 °C at atmospheric pressure, according to the ASTM D286 test method (replaced by the D2155 in 1966, and E 659 in 1978 [39]). Accounting for the effects of pressure and volume on autoignition temperature is also a design requirement, but temperatures below 204 °C have historically been accepted [38].

Experimental data shows that hot surface ignition temperatures from small surfaces generally are several hundred kelvin above the autoignition temperature [40], [41]. Thus, for

design cases where autoignition can be ruled out, the current guidelines are very restrictive. Ignition properties such as hot surface ignition thresholds are highly dependent on a multitude of factors such as geometry, flow conditions, and heat transfer rates, making it impractical to conduct experiments for every possible configuration. Although final design criteria should be based on conservative experimental data from real jet fuel, simulations could help reduce the scope of experimental studies to determine the safe operating conditions. To this end, numerical simulations coupling the fluid dynamics and kinetics may be a valuable tool, as long as a representative surrogate is used.

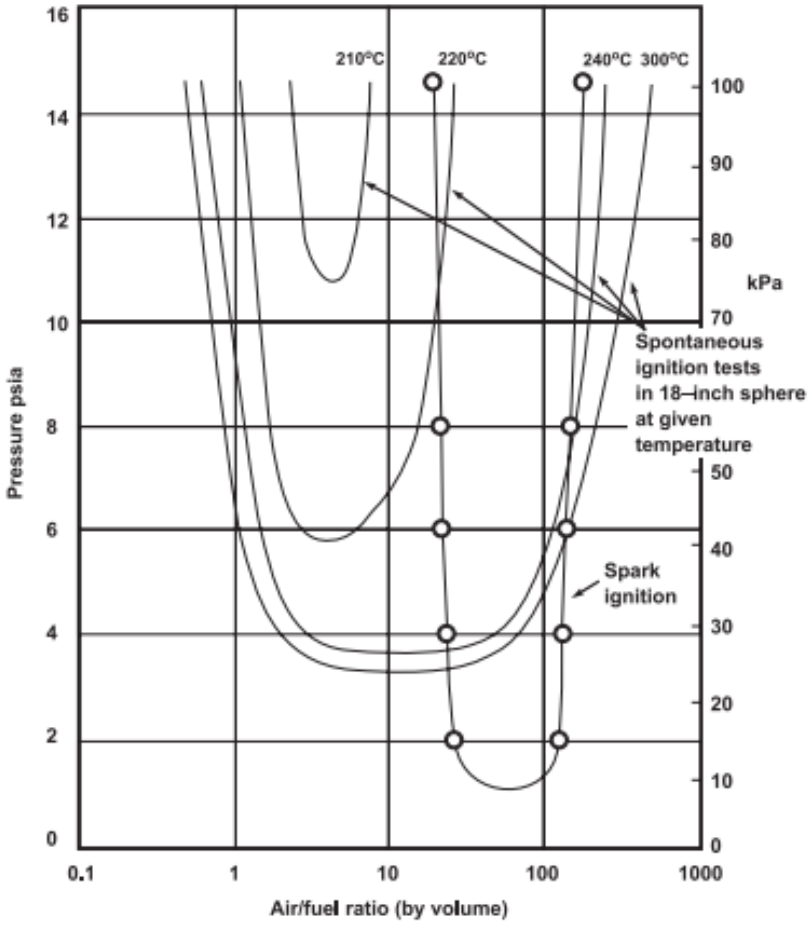

Figure 2.1: Autoignition and spark ignition limits for jet fuel [36].

2.1.2 ASTM E 659 autoignition test

The ASTM E 659 Test Method [39] is a standardized experimental method to determine the autoignition temperature of a fuel. It replaced the previous Test Method D2155 in 1978. Specific instructions are given for both the apparatus and the procedure of the

experiments. A small fuel sample is injected into a 500 ml glass flask that is uniformly heated to a certain temperature. Ignition is determined visually and by temperature measurements of the flask. A distinction is made between hot flame autoignition temperature (AIT), the cool flame ignition temperature (CFT), and the nonluminous preflame reaction threshold temperature (RTT). The results of this test are comparable to Test Method D 2883 [39]. The temperature and fuel sample size is stepped up and down to find the lowest temperatures where these phenomena can be observed, and the delay from injection to ignition is recorded. The autoignition temperature is defined as the lowest temperature where a visible, bright flame can be observed, accompanied by a sharp rise in temperature. A cool flame is characterized as a pale blue flame, and appears below the autoignition temperature at rich conditions.

2.2 Jet fuel surrogates

Jet fuel surrogates are well defined mixtures of fewer, well-studied hydrocarbons, designed to mimic certain properties of commercial jet fuel, that can be modeled and studied in a practical and reproducible way. The target properties depend on the nature of the study. Common property targets for the design of surrogate fuels are:

1. Adiabatic flame temperature
2. Enthalpy of combustion
3. Radical production
4. Laminar flame speed
5. Volatility and evaporation behavior
6. Transport properties
7. Sooting characteristics (premixed and non-premixed)

To achieve this, the following targets may be used:

1. Hydrogen-to-carbon (H/C) ratio
2. Average molecular weight
3. Cetane Number (CN) or Derived Cetane Number (DCN)
4. Smoke point (or threshold sooting index, TSI)
5. Distillation curve

The Cetane Number (CN), also referred to as cetane rating, of a jet fuel is a measure of ignition quality, similar to the octane number of gasoline. It is an inverse function of the igntion delay, so a high Cetane Number fuel has a low ignition delay time. The straight-chained n-hexadecane has a cetane number of 100 and is the high ignition quality reference. The highly branched iso-cetane (IUPAC: 2,2,4,4,6,8,8-heptamethylnonane), also known as HMN, has a cetane number of 15 and is the low ignition quality reference fuel [42]. The volume ratio of these two reference fuels that correspond to the real mixture's behavior determines the Cetane Number. The Derived Cetane Number (DCN) of a fuel mix can be found from several different test procedures. A commonly applied method is the Ignition Quality Tester (IQT, ASTM D6890). In this test, the fuel is injected in a constant volume vessel containing compressed air at a specified temperature and pressure. The measured ignition delay is then correlated to DCN by Test Method D613 [43].

A plethora of researchers have attempted to formulate representative jet fuel surrogates to study various aspects of jet fuel combustion. Early work includes a 14-component surrogate for JP-4 by Wood et al. [44], and a 12-component surrogate for JP-8 by Schulz [45].

Edwards and Maurice [46] defined two types of surrogate fuels: *physical surrogates*, with the same physical properties (e.g density, viscosity, heat conductivity, heat capacity), and *chemical surrogates*, with similar average molecular mass and ratios of aromatics, naphtalenes, olefins, and paraffins. This type of surrogate fuel does not take into account trace compounds and is consequently often unable to match the sooting behavior. Violi et al. [47] also defined *comprehensive surrogates*, that approximate the physical and chemical properties of the real fuel, including the sooting behavior.

Dooley et al. [48], [49] proposed Jet-A (POSF 4658[1]) surrogates designed to target autoignition, adiabatic flame temperature, rate of heat release, local mixing-limited stoichiometric constraint and sooting were chosen as the targets. This was achieved by matching the hydrogen-to-carbon (H/C) ratio and Derived Cetane Number (DCN), as well as the threshold sooting index (TSI) and average molecular weight (MW). A set of 10 hydrocarbons with well documented properties were chosen as a "palette" to represent the different hydrocarbon groups mentioned in Section 2.1:

1. Paraffins
    - n-decane
    - n-dodecane
2. Naphtalenes
    - methyl-cyclohexane
    - n-butyl cyclohexane

[1]Standard sample (5 batch composite) prepared at the Air Force Research Laboratories, Wright-Patterson Air Force Base

3. Aromatics
    - toluene
    - n-propyl benzene
    - 1,3,5-trimethylbenzene
    - 1-methyl naphtalene

Other compunds for each group have also been added. A mixture of 42.67/33.02/24.31 mol.% n-decane/iso-octane/toluene was chosen as a first generation Jet-A (POSF-4658) surrogate, where DCN was the prioritized target, followed by H/C ratio. A mixture of 40/29/7/23 liquid vol% n-dodecane/iso-octane/mesitylene/n-propylbenzene was proposed as a second generation surrogate. Both surrogates gave near identical results and a good match for flow reactor oxidation, ignition delay times and strain rates for extinction.

Hexane has been used in previous studies on hot surface ignition [40], [41] for aviation applications. Owing to its simple reaction mechanism and high vapor pressure, hexane is easy to handle numerically and experimentally. However, higher carbon number fuels such as decane and dodecane more closely resemble the physical and chemical characteristics of real jet fuels.

Dodecane is considered a single-component surrogate, as it has similar physical properties as kerosene jet fuels such as JP-7 at temperatures of 93-649 °C [46]. Dodecane mixed with aromatic hydrocarbons, to account for the aromatic content of real jet fuel, is classified as second generation jet fuel surrogate. However, when the vaporization behavior is important and the distillation curve is to be matched, more components are required to account for the differing volatility of the chemical classes described in section 2.1.

The surrogate design targets are based on data where the transport processes are well known or negligible, such as shock tubes, rapid compression machines, and jet stirred reactors. Therefore, it is of interest to test their validity in cases where the transport processes are very different and play an important role, such as hot surface ignition of initially quiescent fuel-air mixtures. For this purpose, three surrogates of increasing complexity were selected. The target composition for each surrogate on a molar, weight and volume basis is compiled in Table 2.2.

Properties for the pure surrogate components from the DIPPR database [7] are shown in Table 2.3. Note that the AIT value for iso-cetane is based on prediction, not experiment, and is highly uncertain.

2.2.1 Aachen surrogate

The Aachen surrogate [50] is a two-component surrogate composed of 80 wt% n-decane and 20 wt% 1,2,4-trimethylbenzene (TMB), pictured in Figure 2.2. The reaction kinetics

Table 2.2: Target composition of the selected surrogates for this work.

Compound	mol%	wt%	vol%
Single component surrogate:			
Dodecane (with isomers)	100	100	100
Aachen surrogate [50]:			
N-decane	77.0	80.0	82.7
1,2,4-trimethylbenzene	23.0	20.0	17.3
JI Unified surrogate [51]:			
Iso-cetane	36.0	46.5	47.0
N-dodecane	30.0	29.2	30.8
Trans-decalin	24.6	19.4	17.7
Toluene	9.4	4.9	4.5

Table 2.3: Component properties for the surrogates from the DIPPR database [7].

Compound	MW (g/mol)	ρ (liq.)[a] (kg/m^3)	T_{bp} (K)	T_{fp} (K)	AIT (K)	LFL (vol%)	UFL (vol%)	LHV (kJ/mol)
Aachen								
N-Decane	142.28	727.89	447.3	322.9	474	0.75	5.4	6294.22
1,2,4-TMB	120.19	872.19	442.5	318.7	788	0.9	7.3	4930.70
JI Unified								
Iso-cetane	226.44	781.60	519.5	368	978	0.6	4.1	9930.24
N-dodecane	170.33	746.28	489.5	352	476	0.6	4.9	7513.68
Trans-decalin	138.25	866.66	460.5	327	528	0.71	4.9	5880.88
Toluene	92.14	863.91	383.8	279	753	1.1	7.1	3734.00

[a]Liquid density at 25 °C

are well established through experiments in shock tubes, rapid compression machines, jet stirred reactors, burner stabilized premixed flames, and freely propagating premixed flames. The surrogate was developed to mimic kerosene fuels such as Jet-A1, Jet-A and JP-8. Autoignition was the prioritized target, followed by H/C-ratio. The conditions for autoignition, extinction and soot volume fraction was found to be similar to kerosene fuels in laminar non-premixed flames. The surrogate properties were compared to a previous study by Humer et al. [52] where reference batches of JP-8 and Jet-A from different sources were tested and the autoignition and extinction was found to be similar for both fuels. The results for the 80/20 n-decane/TMB blend was found to be in good agreement

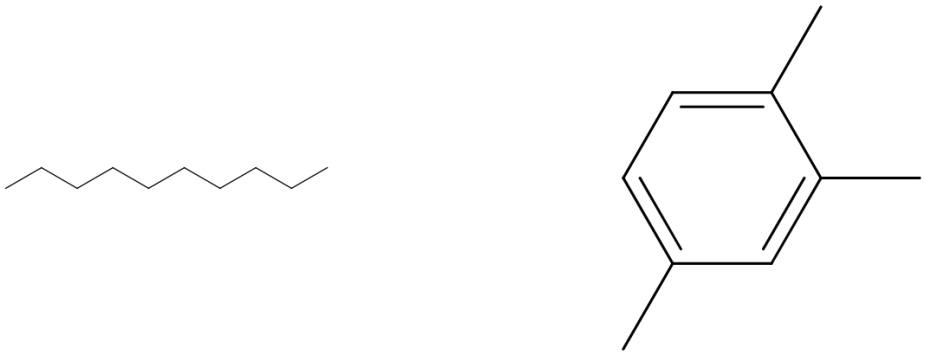

(a) n-decane ($C_{10}H_{22}$): 80 wt% (b) 1,2,4-trimethylbenzene (C_9H_{12}): 20 wt%

Figure 2.2: Molecular structure of Aachen surrogate target components.

with the parent fuel (JP-8 batch POSF 4177, from WPAFB).

2.2.2 JI Unified surrogate

The JI surrogate [51] is a Jet-A (POSF-4658) surrogate composed of isocetane (IUPAC: 2,2,4,4,6,8,8-heptamethylnonane), n-dodecane, trans-decalin (IUPAC: decahydronaphtalene), and toluene. The composition and molecular structure is shown in Figure 2.3.

The JI surrogate was formulated for droplet evaporation modeling, with similar heating, evaporation and ignition characteristics as important targets. An inversed batch distillation method was used to select species that matched the distillation curve of the parent fuel. The surrogate is unified in the sense that it aims to emulate both the physical and chemical properties of the fuel. It is based on the same components as the UM2 surrogate proposed by Kim et al. [53], consisting of 0.2897 mol% n-dodecane, 0.1424 mol % isocetane, 0.3188 mol% trans-decalin, 0.2491 mol% toluene. The targets for this surrogate were the cetane number (CN), lower heating value (LHV), H/C ratio and average molecular weight (MW), as well as the liquid density, kinematic viscosity and surface tension. The JI unified improves upon the UM2 surrogate by tweaking the composition to more closely match the distillation curve of the Jet A POSF-4658 standard.

Droplet evaporation and combustion of the surrogate was simulated with satisfactory results, using the kinetics from the reduced POLIMI231 kerosene mechanism with 231 species and 5591 reactions, including low and high temperature kinetics [25], [26].

2.2.3 Surrogate mixing and analysis

The surrogates were mixed from pure components by weight using a high-accuracy scale. The pure component batch data is shown in Table 2.4 and properties listed on the label are summarized in Table 2.5. The trans-decalin used was a mixture of cis and trans, and the dodecane also included an unspecified amount of isomers.

Table 2.4: Reagent flask data for surrogate pure components.

Compound	Purity (%)	Manufacturer	P-code	#	Lot #
Iso-cetane	98	Aldrich	102035347	128511-100G	STBH7165
Decalin	99	Sigma-Aldrich	1002686452	294772-1L	SHBK0146
Decane	99	Sigma-Aldrich	1000999605	457116-1L	20396APV
Dodecane	99	Aldrich		203-967-9	
TMB	98	Aldrich	1002796403	T73601-500ML	WXBC4246V
Toluene	99.5	EM Science		TX0735P-4	41093115

Table 2.5: Component properties for the surrogates listed on the reagent flasks.

Compound	Purity (%)	MW (g/mol)	T_{bp} (°C)	T_{fp} [a] (°C)	ρ (liq.) (g/mL)	P^{sat} (mmHg)
Iso-cetane	98	226.44	240	96.0	0.793	<1 (25 °C)
Decalin	99	138.25	189-191	57.2		42 (92 °C)
Dodecane	99		215-217		0.749	
Toluene	99.5					

[a] Closed cup flash test.

The JI Unified surrogate mixture was analyzed by Gas Chromatography and Flame Ionization Detection (GC-FID)[2] to find the actual composition of the batch after multiple experiments. The HP5890 Series 2 GC was fitted with an FID, autoinjector, a 30 m HP1-5 column (dimethylpolysiloxane, 5% phenols) and run at equal-split flowrate. The oven was ramped from **50 °C** to **320 °C** over 16 minutes.

[2] Thanks to Conor Martin, and Nathan Dallaska of the Caltech Environmental Analysis Center (EAC), for the assistance with the GC-FID analysis.

The autoinjector sample size was set to 1 microliter. This was found to be an ideal size to avoid blowback of the sample after vaporization in the pre-filter volume. The volume was rinsed with solvent 8 times before each run, and the autoinjector was set to 6 pre-injection sample pumps to acquire a uniform sample free of gas. A dummy sample was run before each run to evacuate any residual impurities and reduce the baseline drift.

163 milligrams of fuel was diluted in 25 milliliters of methyl chloride. This dilution was found to result in symmetric peaks (no overload). Samples of each pure component at different dilutions were also run 5 times to generate calibration tables. The result of the analysis is shown in Table 2.6. The results show good agreement with the target mass fraction (within the margin of error), but with a noticeable decreased value of toluene and enrichment of iso-cetane. This is likely a result of a loss of volatiles through diffusion. This could be during mixing and sample preparation work under a fume hood, but also during storage. The batch glass flask was capped with a PTFE-lined silicone septum. When the septum was punctured repeatably for sample extraction, the PTFE diffusion barrier is broken, allowing volatiles to escape over the approximately 1 month storage period.

Table 2.6: Target and measured composition by GC-FID.

Compound	Target (mass fraction)	Measurement (mass fraction)
Iso-cetane	0.4653	0.4735
N-dodecane	0.2917	0.2889
Decalin (cis/tr)	0.1941	0.1922
Toluene	0.0494	0.0399

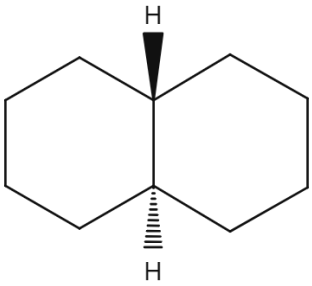

(a) trans-decalin ($C_{10}H_{18}$): 0.246 mol%

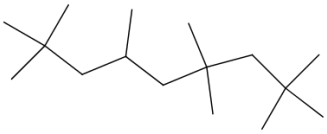

(b) iso-cetane ($C_{16}H_{34}$): 0.36 mol%

(c) n-dodecane ($C_{12}H_{26}$): 0.3 mol%

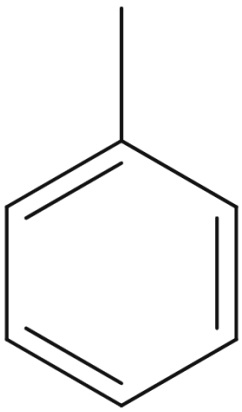

(d) toluene (C_7H_8): 0.094 mol%

Figure 2.3: Molecular structure of JI Unified surrogate target components.

3 Previous studies

The work described in this thesis is a continuation of previous efforts by the Explosion Dynamics Laboratory to study hot surface ignitions of stationary surfaces. The fuels previously studied were hydrogen, ethylene and n-hexane. As those fuels all had sufficiently high vapor pressures at room temperature, the vessel was not heated. The same pressure vessel (114 mm x 114 mm x 171 mm), piping system and pressure transducer (Endevco Model 8530B-200, >10 kHz) was used in [40], [41], [54], [55], with the most significant difference being the ignition source.

3.1 Hexane glowplug ignition

P. A. Boettcher [41] studied hot surface ignition of hexane-air mixtures using glow plugs as the ignition source. Two different types of glowplugs were used; a 3.1 mm diameter, 6.9 mm length Bosch model, and a 5.1 diameter, 9.3 mm length Autolite 1110. Both glowplugs were made of stainless steel and could reach temperatures of 1500 K. The glow plug was installed in the lower end of the field of view, supported by a stagnation plate. A cross-sectional front view of the setup is shown in Figure 3.1. The temperature was measured using an array of OMEGA K-type thermocouples (0.5 second response time) above the glowplug.

A schematic of the vessel and piping system is shown in Figure 3.2. The hexane (89% n-hexane and 11 % isomers) was injected into the piping in liquid form while the system pressure was near vacuum. Subsequently, pure nitrogen and oxygen was added to partial pressures corresponding to the target equivalence ratio. For further mixing, the gases were circulated by the circulation pump. This procedure introduced the possibility of trapping fuel in the dead space of the piping to valve V3 (highlighted). As a consequence, the lower composition uncertainty increased by around 10 % for a reported uncertainty in equivalence ratio of +3%/-13%.

Ratios in the range $0.56 > \phi > 3.0$ were studied at atmospheric pressure and temperature initial conditions. The results showed a minimum ignition temperature of 920 K ±20 K that was nearly constant in the range of $0.75 > \phi > 3.0$, as seen in Figure 3.3. Ignition could not be achieved at equivalence ratios lower than $\phi = 0.6$, and high variability was observed at that equivalence ratio. High variability was also observed near $\phi = 3.0$. No

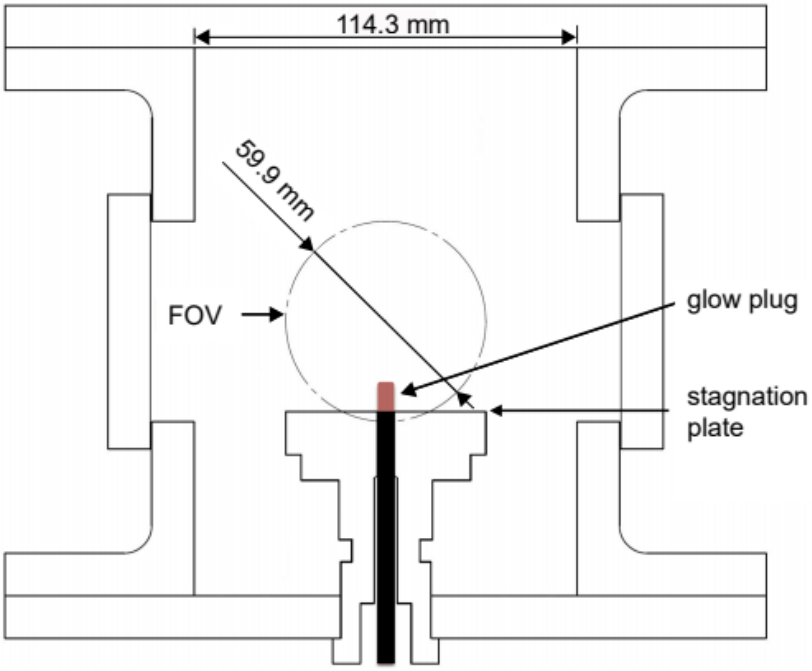

Figure 3.1: Cross-sectional view of the combustion vessel with glowplug ignition, from Boettcher [41]. Used with permission.

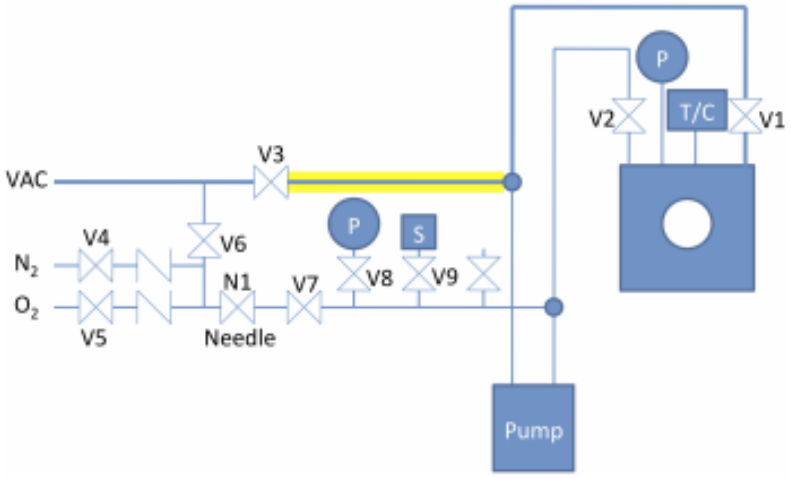

Figure 3.2: Schematic of the vessel and piping system, from Boettcher [41]. Used with permission.

experiments were performed at or above the upper flammability limit from literature, given as 7.4 mol% ($\phi = 3.4$)[19].

High speed schlieren images were captured to visualize the thermal plume and ignition dynamics. The images were captured at 1000-2000 frames per second with a 800x800 pixel

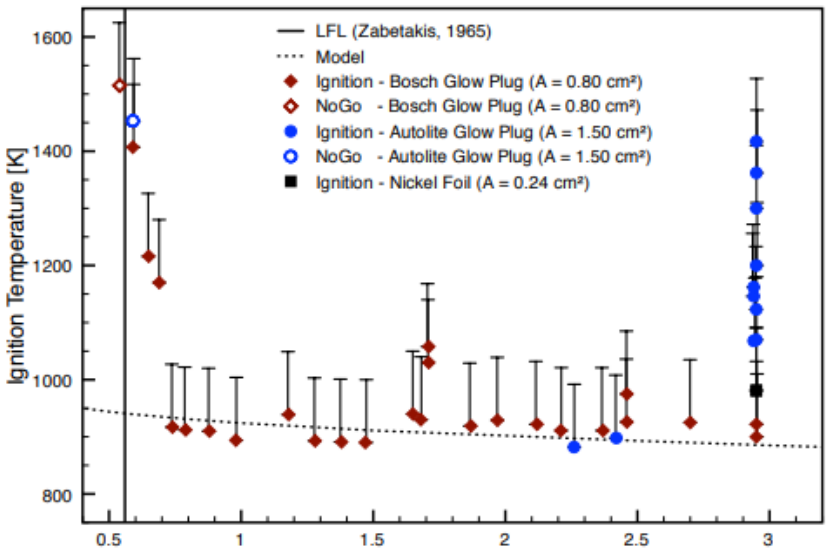

Figure 3.3: The glowplug ignition study results of Boettcher [41] for hexane-air at atmospheric pressure. Equivalence ratio uncertainty was +3%/-13% (not shown). Used with permission.

resolution. Several different schlieren techniques were employed, such as color and dark background schlieren. A dark background schlieren time series of the flame propagation is shown in Figure 3.4

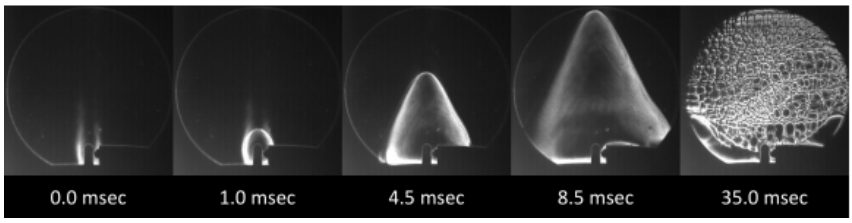

Figure 3.4: Dark background schlieren time series of hexane flame propagation, from Boettcher [41]. Used with permission.

3.2 Hydrogen, ethylene and hexane hot cylinder ignition

L.R Boeck, A. Kink and M. Meijers [40], [54], [55] studied hot surface ignition of hydrogen, ethylene and n-hexane mixed with air at atmospheric pressure. The ignition source was a hot cylinder assembly designed by Kink to achieve a more uniform temperature than the glowplug. With this new ignition device, the surface temperature uncertainty along the length was reduced from 10 % to 3-5 % of the measured temperature. This was established by surface scanning test, shown in Figure 3.5.

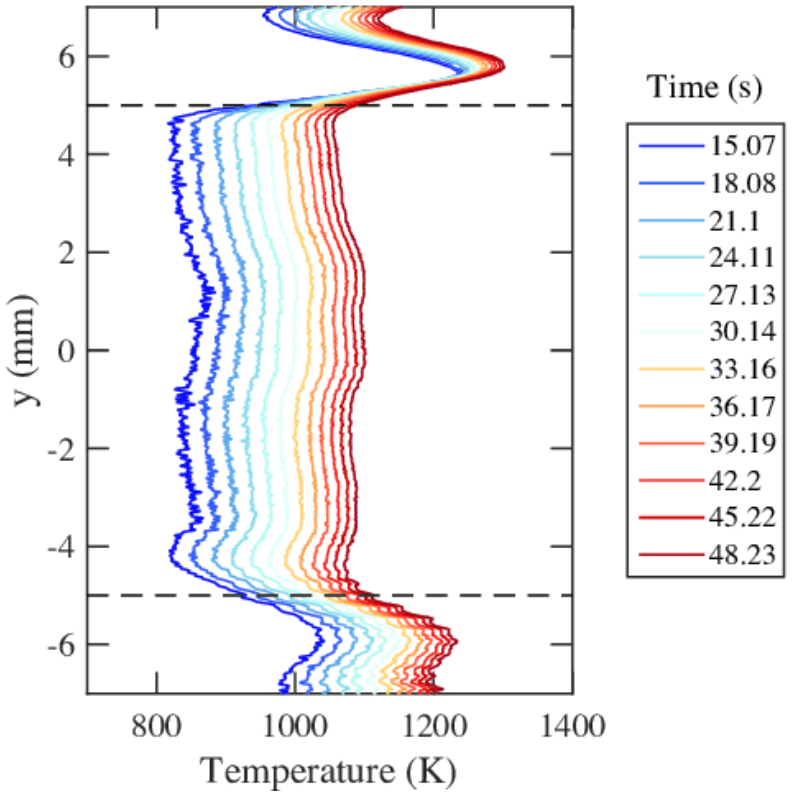

Figure 3.5: Surface temperature profiles along the cylinder during heating in air, measured by scanning pyrometry. Horizontal dashed lines mark boundaries of the heated stainless steel cylinder at $y = \pm 5\text{mm}$, from Boeck et al. [40]. Used with permission.

The orientation of the cylinder could also be changed, and the effect of vertical vs. horizontal cylinder orientation on ignition temperature was studied. Instead of thermocouples, a two-color pyrometer designed and built by Boeck was utilized for non-intrusive, high-frequency temperature measurements. The schlieren system was also interchanged for Mach-Zehnder interferometry, to allow for quantitative resolution of the temperature field through Fourier post-processing. Figure 3.6 shows finite fringe interferograms of the heated and non-heated cylinder in the horizontal orientation. The pyrometer, Mach-Zehnder interferometer, and cylinder in the vertical orientation were also used in this work, and will be described in further detail in the following chapter.

Pure hydrogen and ethylene was injected in gaseous form, and n-hexane (>99%) was injected as a liquid. All fuels were injected into the piping, and the mixing procedure was similar to that of Boettcher. The initial pressure and temperature was 101.3 kPa and 296 K, respectively.

For the horizontal cylinder orientation, the results showed ignition temperatures of 960-1100

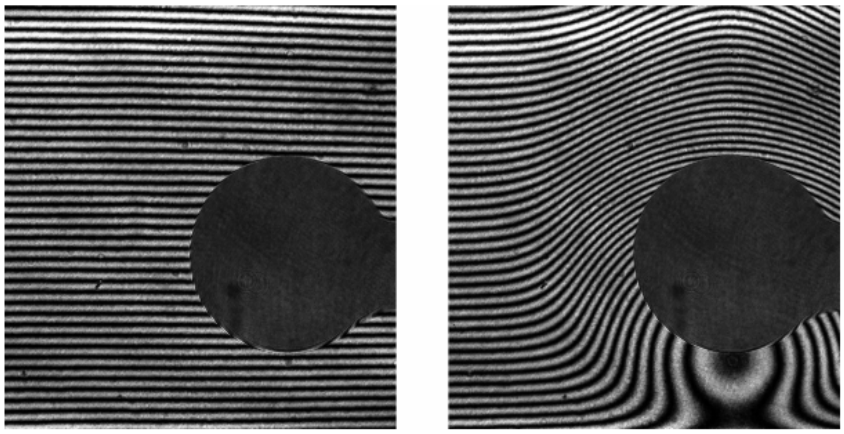

Figure 3.6: Finite fringe interferograms of a non-heated horizontal cylinder (left) and a heated horizontal cylinder (right), from Kink [55].

K for hydrogen, 1060-1100 for ethylene, and 1150-1190 K for n-hexane. The vertical orientation increased ethylene and n-hexane ignition temperatures by 50-110 K. Hydrogen ignition appeared unaffected by changes in orientation. Results, along with AIT-values from literature [56] are shown in Figure 3.7.

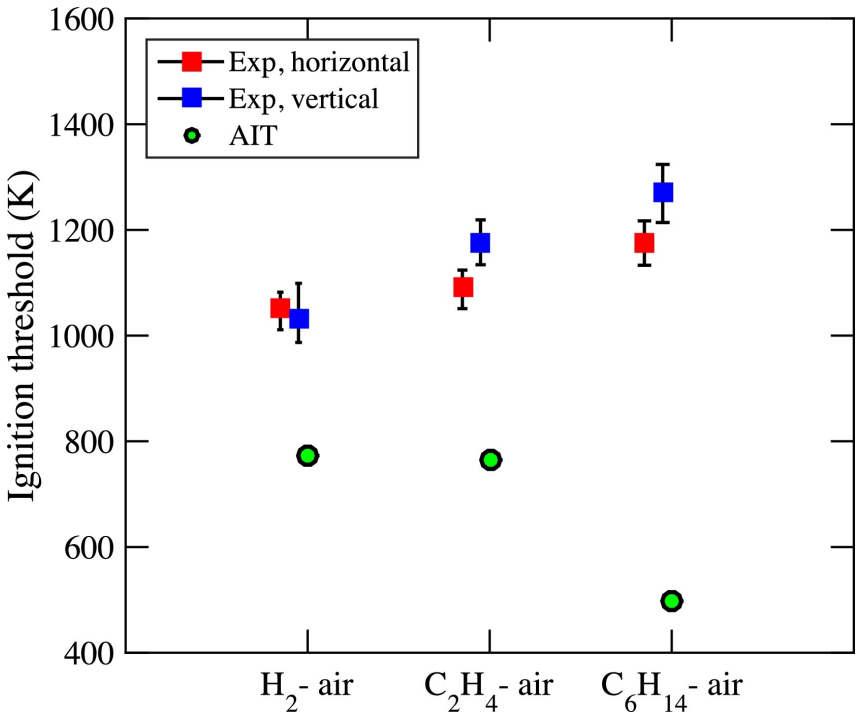

Figure 3.7: Ignition thresholds for stoichiometric fuel-air mixtures. Initial pressure and temperature 101.3 kPa and 296 K, respectively. Auto-ignition temperatures (AIT) from [56]. Figure from Boeck [40]. Used with permission.

4 Surrogate Vapor Liquid Equilibrium

The previous work summarized in the foregoing chapter was performed with pure, high vapor pressure components. On the other hand, jet fuel, and most jet fuel surrogates, are multi-component mixtures containing both low and high vapor pressure components. This complicates the evaporation behavior of the fuel, which in turn has great implications for practical safety scenarios and experiments. Many of these implications can be understood from the vapor-liquid equilibrium behavior of the fuel mixtures. This chapter aims to investigate some of these implications, and provide the basis for design modifications of experimental apparatus used to study jet fuel surrogate ignition.

One important safety consideration is that the vapor composition of a multi-component mixture may differ from that of the liquid fuel. This is important in cases where the fuel is not completely vaporized, such as fuel tank vapor space explosion, pool fires, and spray or mist explosions. For such scenarios, the vapor-liquid interaction can be important. It is the vapor composition that determines the flammability and ignition characteristics, but this in turn is governed by the vapor-liquid equilibrium. For a pure component fuel, such as ethane, there is no change in composition with evaporation, and the flammability is very predictable. However, for a multi-component mixture, such as jet fuel, the vapor phase is enriched in the more volatile components in the fuel. Thus, the liquid composition of a fuel may not be representative for the characterization of ignition behavior. For alkanes, the autoignition temperature generally increases with increasing volatility. The same trend is also expected for hot surface ignition [57]. Hence, the ignition temperature of the enriched vapor phase is expected to be higher than that of the initial fuel. The minimum ignition energy (MIE) at lean to stoich conditions for alkanes increases with carbon number, but at rich conditions the opposite is observed [58]–[60]. For these reasons, complete evaporation is an important prerequisite for surrogate studies to avoid potentially misleading results.

Most jet fuel surrogates are designed to mimic the ignition behavior of jet fuel at complete evaporation. For complete evaporation, the vapor fuel-composition is equal to that of the original liquid fuel for any fuel. The Aachen surrogate is composed of two hydrocarbons with very similar volatility, so the difference in composition in the vapor and liquid at partial evaporation/condensation is expected to be small. Although this behavior is very different from commercial jet fuel, it reduces the consequence of inadvertent condensation in experiments designed to test the surrogate at complete evaporation.

The JI surrogate on the other hand, consists of hydrocarbons of very different volatility. If the difference in vapor composition is very different, the ignition results may not be valid for incomplete evaporation. To investigate this, consider a steady state combustion chamber modeled as a single equilibrium stage (P,T-flash), as described in Section 1.1.2. Hot gaseous fuel and air are injected at a stoichiometric ratio ($\phi = 1$, molar $AFR = 89.5$) into a combustion chamber held at a constant temperature. Assume the residence time is sufficient for equilibrium to be instilled in the chamber. Figure 4.1 shows the resulting vapor composition for the JI Unified surrogate at atmospheric pressure. Figure 4.2 shows the corresponding fuel vapor composition (normalized to exclude air). The composition was calculated in Aspen HYSYS V10 [61] using the Peng-Robinson equation of state [62]. At low pressures, sufficiently accurate predictions can also be obtained from solving Equation 1.16. The LFL criteria for the flammable regime above $T \approx 74\,°\mathrm{C}$ is estimated based on Le Chatelier's mixing rule (Equation 1.40).

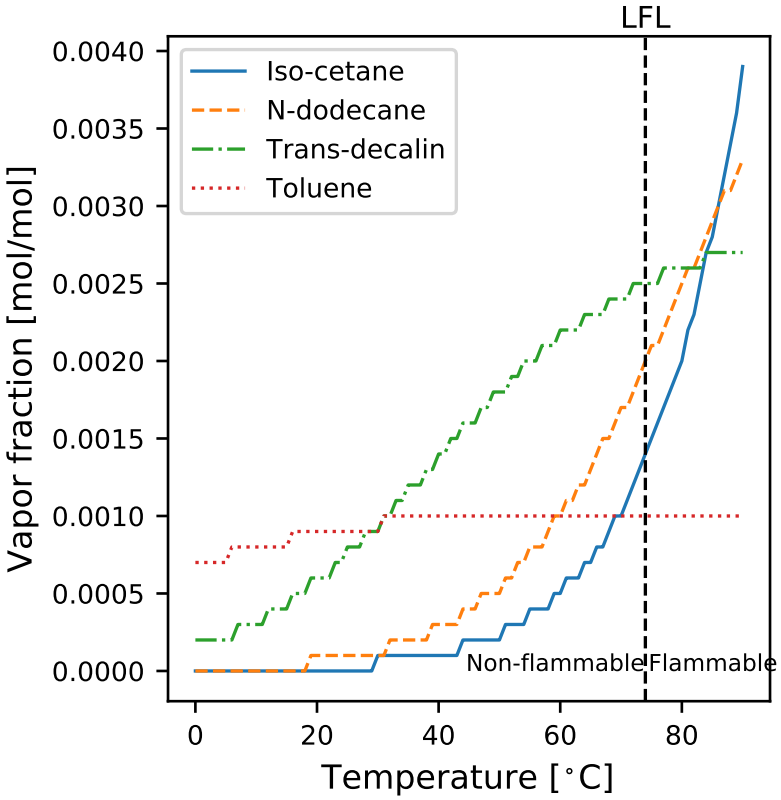

Figure 4.1: Vapor composition of JI Unified surrogate mixed in a vapor-liquid-equilibrium at inlet $\phi = 1$ as a function of temperature.

Depending on the temperature, three scenarios can be identified:

- Above the dew temperature ($T_{dew} = 92\,°\mathrm{C}$, see Table 4.4), all the fuel will remain in the vapor phase; the vapor would be at stoichiometric conditions, and the vapor

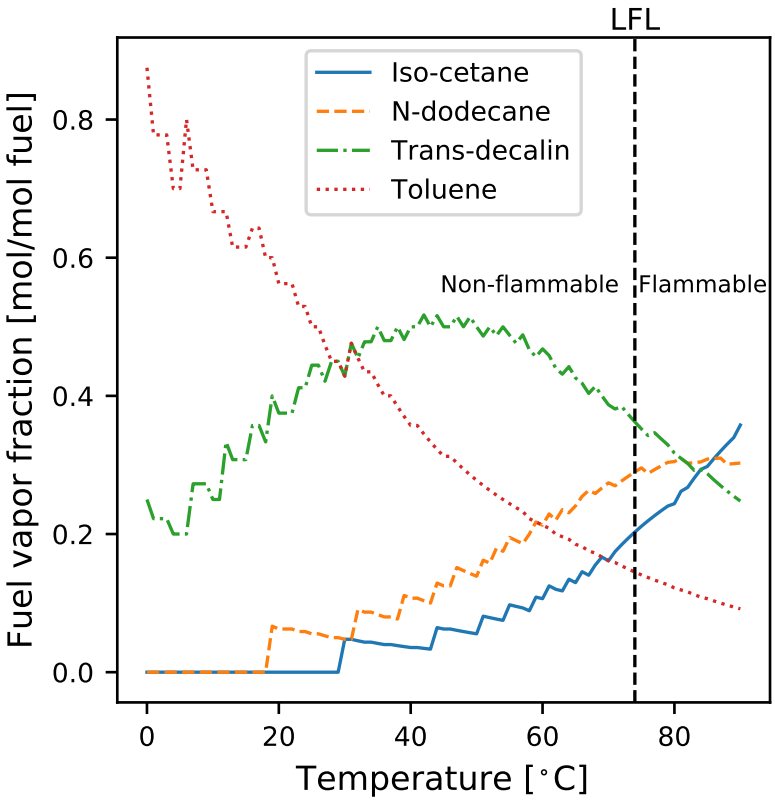

Figure 4.2: Fuel vapor composition of JI Unified surrogate at vapor-liquid equilibrium at inlet $\phi = 1$ as a function of temperature (normalized without air).

fuel composition would equal the feed composition. For each flammable component, the vapor fraction is given by $y_i = \frac{z_i}{1+AFR}$, where z_i is the initial fuel composition (not taking air into account).

- Below the dew temperature, but above the flash point ($T_{fp} \approx 74\,°\mathrm{C}$), some of the fuel will condense, and a flammable mixture of a different composition than that of the liquid fuel exists. The mixture is now leaner, but still flammable. The fuel vapor mixture (normalized without air) is enriched in the more volatile components in the fuel, and may have different ignition characteristics.

- Below the flash point (LFL, $T_{fp} \approx 74\,°\mathrm{C}$), the mixture is too lean to be flammable.

The effect on ignition characteristics will depend on the relevant fuel and how different the pure component ignition characteristics are, as well as the fuel-air ratio, temperature, vessel geometry, the procedure, and at what point in the process the ignition source is introduced. This will be further investigated for two cases relevant for the current tests being performed at EDL: hot surface ignition and autoignition tests.

1. Hot surface ignition (closed chamber)
2. ASTM E659 autoignition test (open chamber)

4.0.1 Closed combustion chamber

The hot surface ignition tests in this work were performed in an enclosed chamber of constant volume. The system volume, pressure and temperature is known and constant. The liquid sample volume is very small (75-750 microliters) compared to the volume of the vessel (2.2 liters). The total amount of moles is determined by the ideal gas law. The moles of fuel in the vapor space is given by the total moles of fuel in the case of complete evaporation. The remaining moles are air. At higher temperatures, the fuel will occupy a larger fraction of the total volume (air is added last to achieve atmospheric pressure).

For these experiments, the hot surface ignition source is located in the middle of the vessel. As a result, the system temperature is very non-uniform, and it is the gas composition near the hot surface that governs the ignition. In the case of partial evaporation, the composition near the hot surface could be very different from the liquid sample. For this reason, ensuring complete evaporation of the fuel and adequate mixing is important for the surrogate results to be comparable and repeatable. At complete evaporation of the small liquid samples used for this work, the effect of dissolved O_2 and N_2 are negligible.

To ensure that the entire fuel mixture is in the vapor phase during the experiments, the mixture should be above the dew temperature, and not come into contact with colder surfaces. By solving Equation 1.8 iteratively in Python, the dew temperature for the surrogates in question at equivalence ratios in the flammable range were found, as shown in Table 4.2, 4.3, and 4.4. The upper (UFL) and lower flammability limit (LFL) were calculated by Equation 1.40 and pure component data from the DIPPR 801 database [7], [8]. The vapor pressures were estimated from the DIPPR 101 Equation 1.19, and the relevant coefficients are compiled in Table 4.1. The dew temperature as a function of equivalence ratio for the three surrogates is shown in Figure 4.3.

Table 4.1: DIPPR 101 vapor pressure equation parameters, from the DIPPR 801 database [7], [8]

Compound	A	B	C	D	E	T_{min} (K)	T_{max} (K)
N-decane	112.73	-9749.6	-13.245	7.1266E-06	2.0	243.5	617.7
N-dodecane	137.47	-11976	-16.698	8.0906E-06	2.0	263.6	658.0
Iso-cetane	128.31	-11839	-15.333	6.9676E-06	2.0	163.0	692.0
Trans-decalin	100.94	-9055.5	-11.585	6.1499E-06	2.0	242.8	687.0
Cyclohexane	51.087	-5226.4	-4.2278	9.7554E-18	6.0	279.7	553.8
Toluene	76.945	-6729.8	-8.179	5.3017E-06	2.0	178.2	591.7
1,2,4-TMB	85.301	-8215.9;	-9.2166	4.7979E-06	2.0	229.3	649.1

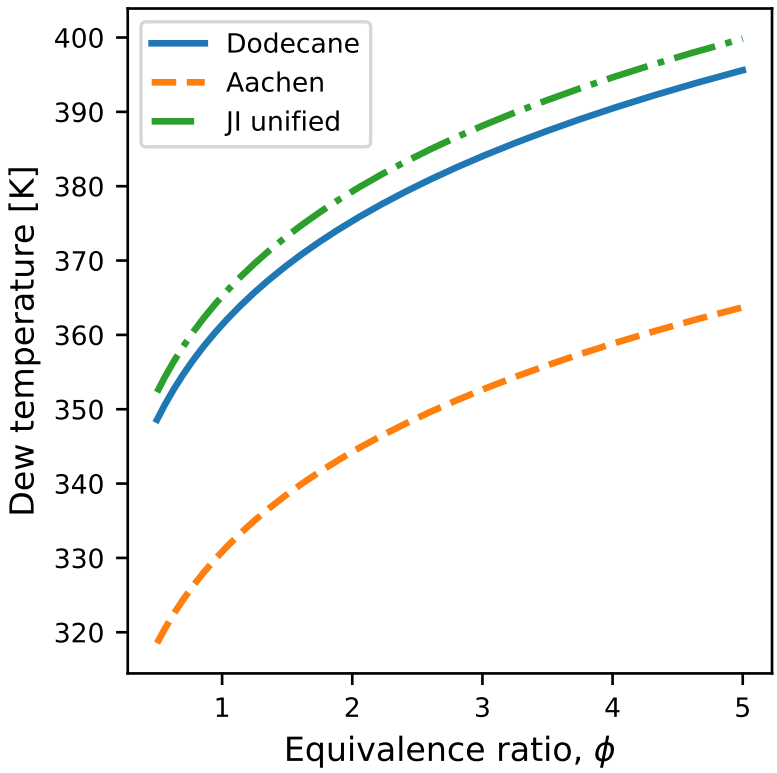

Figure 4.3: The dew temperature of selected jet fuel surrogates as a function of equivalence ratio. Calculated in Python using pure component data from the DIPPR database [7].

Table 4.2: Dew temperature at different stoichiometries for n-dodecane

ϕ	y_{fuel} (%)	T_{dew} (K)	T_{dew} (°C)
0.5	0.564	348.59	75.44
0.532	0.600 (LFL)	349.69	76.54
1.0	1.123	361.38	88.22
3.0	3.294	384.03	110.88
4.538	4.900 (UFL)	393.35	120.20
5.0	5.373	395.60	122.45

4.0.2 Open combustion chamber

In strict thermodynamic terms, no equilibrium can be reached for open systems where mass crosses the boundary. However, local equilibrium is still assumed for practical modeling purposes. Thus, the open chamber is modeled by the same assumptions as the closed combustion chamber. Instead of air being injected until atmospheric pressure is

Table 4.3: Dew temperature at different stoichiometries for Aachen surrogate

ϕ	y_{fuel} (%)	T_{dew} (K)	T_{dew} (°C)
0.5	0.7097	318.53	45.38
0.578	0.820 (LFL)	321.02	47.87
1.0	1.409	330.85	57.70
3.0	4.113	352.64	79.49
4.173	5.630 (UFL)	359.74	86.59
5.0	6.671	363.72	90.57

Table 4.4: Dew temperature at different stoichiometries for JI unified surrogate

ϕ	y_{fuel} (%)	T_{dew} (K)	T_{dew} (°C)
0.5	0.556	352.29	79.14
0.585	0.650 (LFL)	355.12	81.97
1.0	1.106	365.21	92.06
3.0	3.247	388.13	114.98
4.409	4.700 (UFL)	396.89	123.74
5.0	5.296	399.84	126.69

reached after the evaporation of the fuel as for the closed chamber, the open case can be interpreted as the injected fuel evaporating and displacing some of the air initially in the chamber. It is assumed that no fuel escapes the vessel before ignition. These assumptions are valid if the mass transport out of the volume is slow.

Figure 4.1 showed that the vapor composition of a partly evaporated fuel sample can be very different from the liquid fuel if vapor-liquid equilibrium is reached between the flash and dew temperature before ignition. However, the autoignition temperature is significantly higher than the dew temperature for all components studied when the presence of air is taken into account. Thus, if an equilibrium is achieved before ignition, the measured autoignition temperature would be representative of the initial (completely vaporized) fuel composition.

However, in the ASTM659 autoignition test procedure, the vessel is heated up prior to injection of the fuel. Thus, around the autoignition temperature, the conditions for ignition are already present when the fuel is injected. Ignition generally ensues within minutes, and there is no forced mixing in the chamber. Evaporation by diffusion is a slow process, and at these time-scales, the equilibrium assumption is likely not valid for low-volatility compounds such as n-dodecane. This is supported by experimental observations during test performed at EDL[1]: less volatile components were found to be ignitable at

[1]ASTM E659 experiments conducted by Conor Martin at EDL.

stoichiometries above the UFL, and a visible residual layer was formed on the bottom of the flask, indicating that the sample was not fully evaporated at ignition.

5 Methodology

5.1 Combustion vessel

The experimental set-up consists of a 114 mm x 114 mm x 171 mm (width x depth x height) rectangular, closed, 2 liter pressure vessel. Identical 59.9 mm optical glass windows are mounted on the front and back of the vessel. The top of the vessel is fitted with an Endevco Model 8530B-200 pressure transmitter with a response time of over 10 kHz, and an internal K-type thermocouple with response times of approx. 1 s. The test vessel externals are identical to those described in previous studies at the Caltech Explosion Dynamics Laboratory [40], [41].

In this work, the vessel was modified to study hot surface ignition of surrogate fuels. As discussed in Chapter 4, to avoid partial condensation of the fuel, either in the vessel itself or in the filling and circulation lines, the following modifications were done:

1. Heating
2. Insulation
3. Wall temperature measurements
4. Direct side injection
5. In-vessel mixing

5.1.1 External heating and temperature measurement

The underside of the vessel was heated directly by a 615 W combined hot plate and stirrer (Corning PC-351). The same plate also produces a magnetic field to drive a magnetic stirbar with an attached impeller placed inside the vessel. The wall temperature of the vessel was measured using four stick-on thermocouples (OMEGA SA1-K-72-SRTC), placed on the bottom, middle, and top of the vessel, as well as on the outer end of the injection point.

1. TT1: Internal temperature (top)
2. TT2: Bottom wall temperature

3. TT3: Side wall temperature (injection side)
4. TT4: Injection line temperature
5. TT5: Top wall temperature

To ensure full evaporation and avoid trapped liquid in the injection point line, the liquid was injected at a vacuum, and the line was slanted and heated by a 43 Watt heating cord, controlled by a PID Temperature Controller (OMEGA CN76000) and Solid State Relay (OMEGA SSR240DC45). Before each experiment, the temperature was ensured to have reached steady state above the calculated dew point for the surrogate.

The filling lines, up to the valves V1 and V2, were also heated by heating cords to avoid condensation on the tube walls. The piping temperatures were measured with a handheld thermometer.

5.1.2 Insulation

In addition to heating, insulation of the vessel was also considered. Calculations estimating the heat loss from the vessel indicated that insulation would not be necessary to attain temperatures above the dew point temperature for the surrogates in question. Nevertheless, the vessel was still insulated to decrease the heating required, achieve more uniform surface temperatures, and reduce heat currents and the risk of skin burns. The insulation solution was based on the following specifications:

1. Withstand at least 200 °C
2. Insulation surface temperature below 50 °C
3. Provide optical access
4. Provide access to side injection point
5. Be easily removable without interfering with optics
6. Not leave debris on removal

Based on these specifications, a 1 inch Teflon-fiberglass insulation blanket with Velcro fasteners was found to be the best solution. A custom blanket made to fit the vessel geometry was ordered from InsulTech. Beam covers were also installed to reduce external heating-induced air currents that could interfere with the interferometry. The insulated vessel with beam covers is shown in Figure 5.1. The final installation of heating cords for the side injection point and top tubing is not shown.

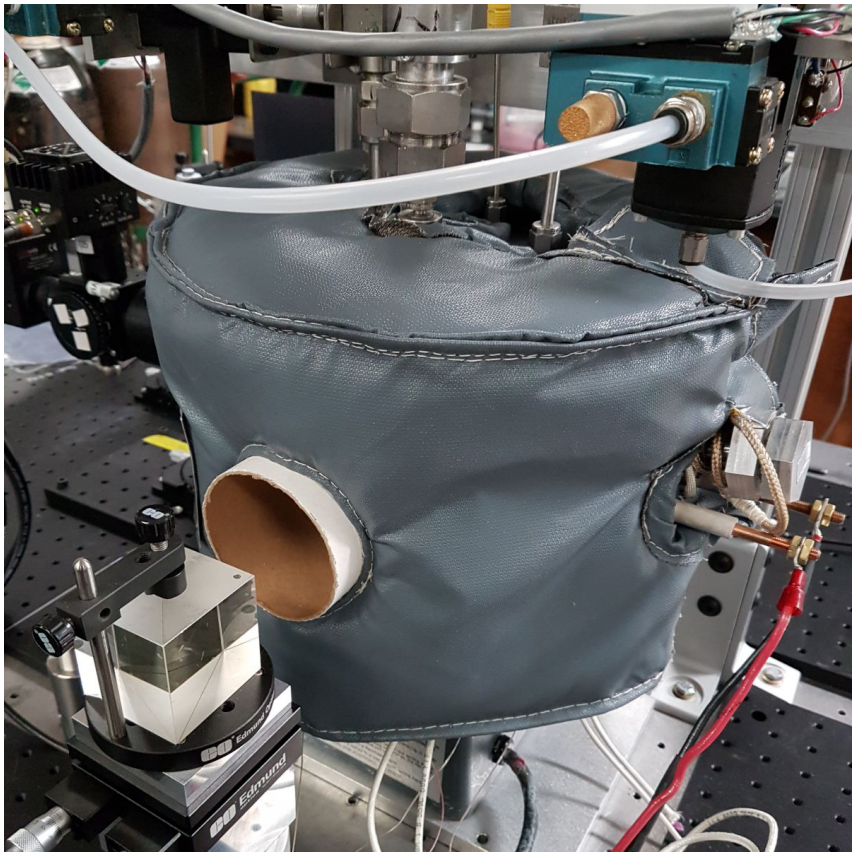

Figure 5.1: Combustion vessel with insulation and beam covers installed. Note that the side injection and top tubing heating installation is not finished in this picture.

5.1.3 Mixing

Despite the small volume of the vessel, previous experience indicated that good mixing was important for consistent ignition data.

The previous iteration of the vessel setup was mixed by circulating the mixture through the piping system with a circulation pump. To avoid condensation and accumulation in this piping loop, the entire system would have to be trace heated. Instead, the fuel injection point was moved to the side of the vessel, and a magnetic stirrer was designed for the vessel. This reduced the inaccuracies in the concentration from the volume and dead ends in the piping system, as illustrated in Figure 3.2.

A 3-inch long PTFE-coated teflon stirbar was fitted with a 4-blade impeller, and placed in a cavity on the bottom plate. The spinner was powered by the magnetic field induced by the combined hot plate and stirrer. A lip was installed above the cavity to keep the spinner upright and in place after ignition or if spin-out occurred. The assembly is shown in Figure 5.2.

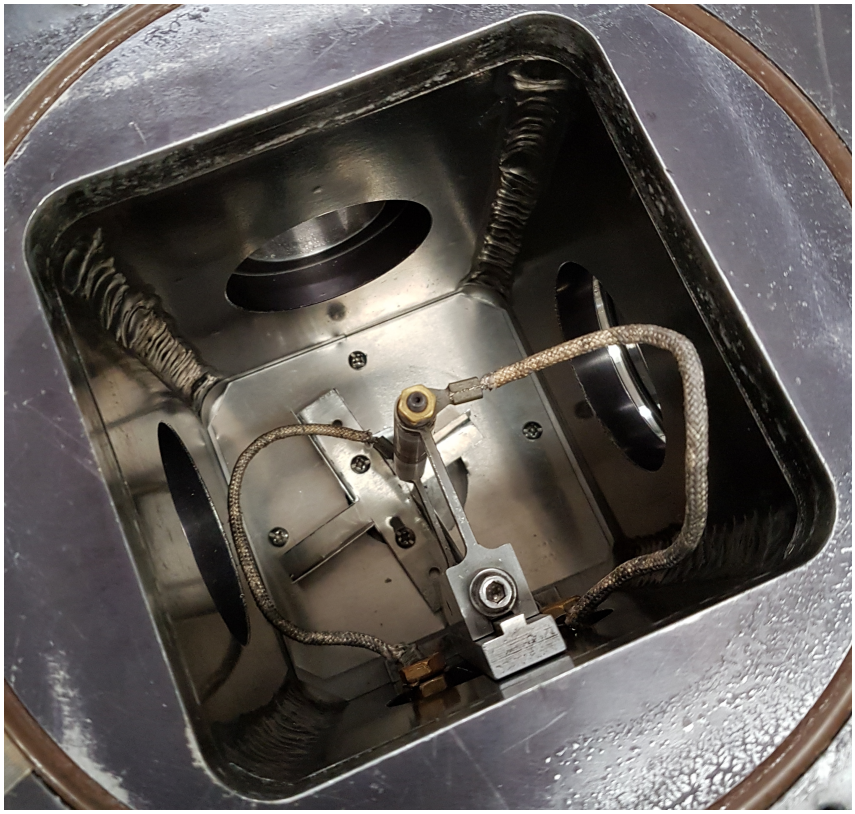

Figure 5.2: Combustion vessel internals with stirbar impeller and lip installed.

To ensure that the impeller could provide adequate mixing, interferograms of a heated cylinder were captured with the impeller off and on. The result of the test can be seen in Figure 5.3. Figure 5.3b shows well-distributed turbulence created in the chamber.

5.2 Ignition cylinder

The hot surface ignition source for the experiments was a 316 stainless steel cylinder designed by A. Kink [55]. Cylinder dimensions were 10 mm length, 10 mm O.D, and 1 mm thickness, giving an aspect ratio of 1. The cylinder was designed to reach 1350 K and provide a uniform temperature field. This is important for the measured temperature to be representative of the ignition temperature regardless of the location of ignition on the surface. Additionally, the symmetry of the cylinder greatly simplifies the post-processing of the interferograms.

The cylinder is indirectly heated by a 24 American Wire Gauge (AWG) Khantal A-1 resistance wire. The wire is coiled around a quartz support rod and pressed into the slits in the two conducting copper rods. The stainless steel cylinder covers the wire coil, with

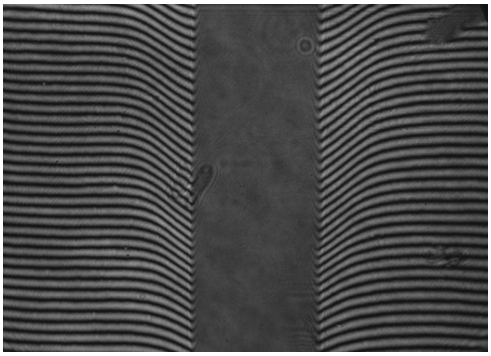

(a) Cylinder heating with impeller off

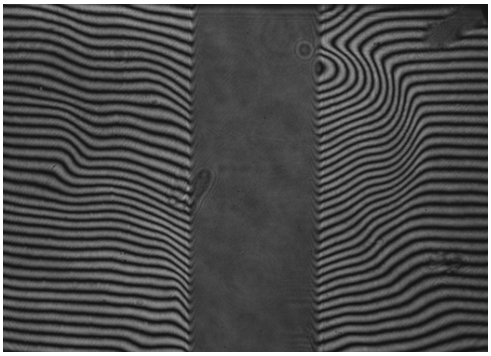

(b) Cylinder heating with impeller on

Figure 5.3: Mixing test: Interferograms showing a heated cylinder with impeller off and on

a tightly packed layer of magnesium oxide (MgO) powder between. Magnesium oxide is an ideal electrical insulator for heating applications due to it's high thermal conductivity. The cylinder is mounted between two quartz insulation pieces that are held firmly in place by the support structure cantilevers. A cross-section view of the assembly is shown in Figure 5.4.

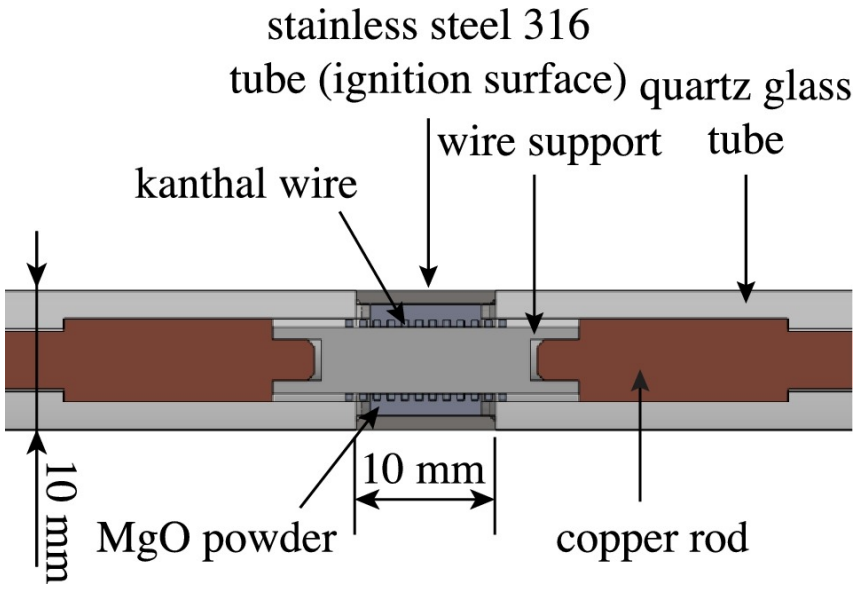

Figure 5.4: CAD cross-section view of the parts of the cylinder assembly, from Boeck [40]. Used with permission.

The copper rods in the assembly were later modified with wider slits to allow for installation of 22 AWG Khantal A-1 wire. Wire of increased thickness (lower AWG) is more resilient, but also has less resistance and consequently requires higher current to attain the same temperature. An assembly with 13 touching windings of 22 AWG wire was tested, and could withstand 4.5 minutes of 10 A, 10 V before burning out. It reached a

maximum temperature of 1050 K (Aachen shot 9).

5.3 Pyrometer

A pyrometer is a non-intrusive thermometer that measures the temperature of a surface based on it's emission of thermal radiation. In this work, a two-color pyrometer was used for non-intrusive, high-frequency temperature measurements. The pyrometer is shown in Figure 5.5.

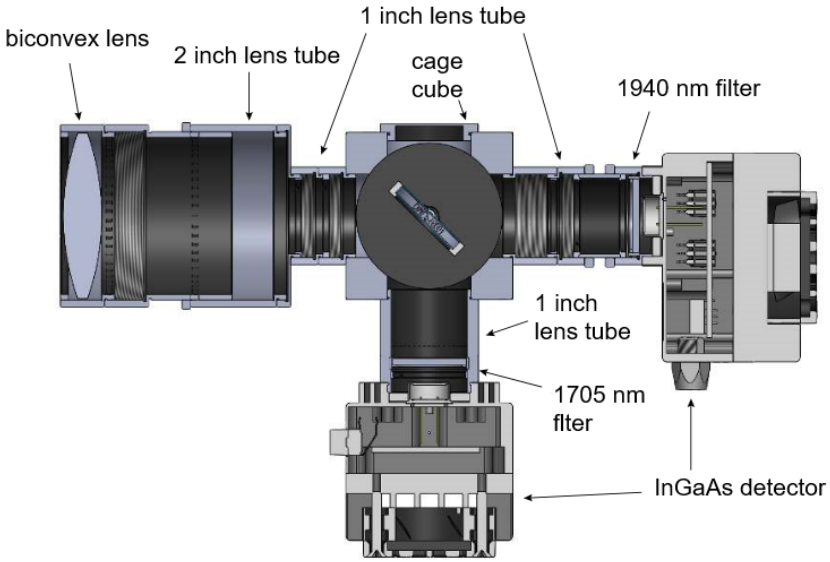

Figure 5.5: CAD drawing of the two-color pyrometer, designed by Boeck [40]. Used with permission.

When studying radiation, the black body is a useful theoretical construct with the following properties:

1. It absorbs all incident radiation
2. For a specific temperature and wavelength, it emits the maximum energy possible.
3. The emission is independent of direction (diffuse emitter).

The spectral radiance (described as spectral intensity in [34], but this term is omitted to avoid confusion with other conflicting definitions of intensity) is the rate at which radiant energy is emitted at a given wavelength and direction, per unit area of the emitting surface normal to this direction, per unit solid angle about this direction, and per unit wavelength. It has units of power per (projected) area per steradian per wavelength $\mathrm{W}/(\mathrm{m}^2\,\mathrm{sr}\mu\mathrm{m})$ The spectral radiance emitted from a black body at a given temperature and wavelength is described by Planck's law

$$L_{\lambda,b}(\lambda,T) = \frac{2hc^2\lambda^{-5}}{\exp(\frac{hc}{\lambda k_B T}) - 1} \tag{5.1}$$

where $L_{\lambda,b}$ is he spectral radiance at a given wavelength and direction, $h = 6.626 \times 10^{-34}$Js is the universal Planck constant, $k_B = 1.381 \times 10^{-23}$J/K is the Boltzmann constant, $c = 2.998 \times 10^8$m/s is the speed of light in vacuum [34]. Each individual temperature has a distinct spectral radiance curve, as shown in 5.6.

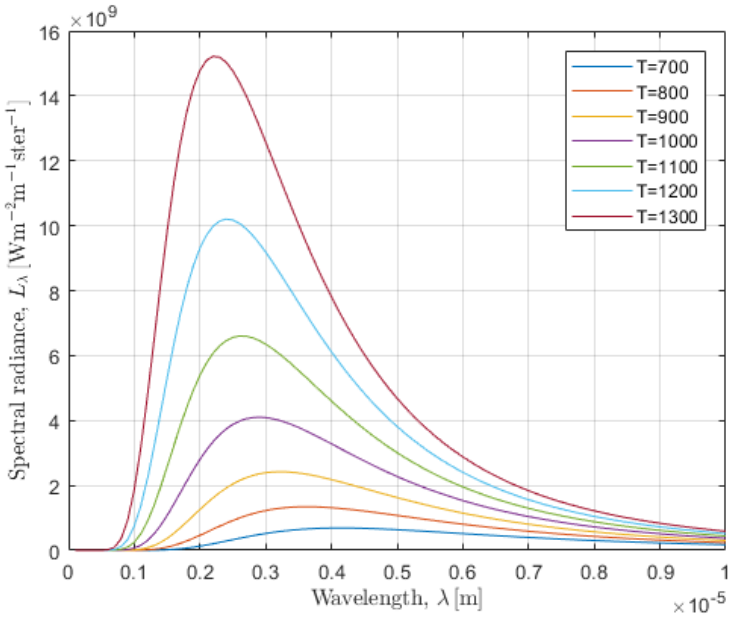

Figure 5.6: Black body spectral radiance curve.

The spectral emissive power per area of emitting surface (also known as exitance, emittance or radiant flux density, same units as irradiance but based on the emitting and not incident area) is found by integrating the intensity over all directions (as a hemisphere in spherical coordinates). Because black body emission is independent of direction, we get

$$E_\lambda(\lambda) = \int_0^{2\pi}\int_0^{\pi/2} L_\lambda(\lambda)\cos(\theta)\sin(\theta)\,d\theta\,d\phi = \pi L_\lambda(\lambda) \tag{5.2}$$

where E_λ is the spectral emissive power with SI units of Watts per surface area (spectral emittance or spectral flux density). The cos term in the integrand is a consequence of the irradiance being based on he projected area, whereas the power is based on the emitting surface area.

The peak of this curve can be found by Wien's displacement law

$$\lambda_{max} T = b \tag{5.3}$$

where $b = 2898 \mu \mathrm{mK}$ is Wien's displacement constant.

At short wavelengths (high frequencies) ($h\nu \gg kT$), or $\lambda < 5\lambda_{max}$ the Wien approximation is valid

$$E_{\lambda,b}(\lambda, T) = \frac{2\pi hc^2 \lambda^{-5}}{\exp(\frac{hc}{\lambda k_B T})} \tag{5.4}$$

To account for the fact that real emitting surfaces do not behave as black bodies, the spectral emissivity $\varepsilon_{\lambda,T}$ correction factor is introduced. The spectral emissivity is defined as the ratio of spectral radiance of a real emitted to that of a blackbody at the same temperature

$$\varepsilon_{\lambda,T} = \frac{I_{\lambda,T}}{L_{\lambda,T,b}} \tag{5.5}$$

where subscript b signifies blackbody and subscript lambda signifies that it is a spectral quantity.

$$E_{\lambda,b}(\lambda, T) = \frac{\varepsilon_{\lambda,T} 2\pi hc^2 \lambda^{-5}}{\exp(\frac{hc}{\lambda k_B T})} \tag{5.6}$$

By integrating the spectral emissive power over all wavelengths, we get the well-known Stefan-Boltzmann law

$$E = \int_0^\infty E_\lambda d\lambda = \varepsilon \sigma T^4 \tag{5.7}$$

where E is the total emissive power, ε is the emissivity of the object, and $\sigma = 5.670367 \times 10^{-8} \mathrm{Wm}^{-2}\mathrm{K}^{-4}$ is the Stefan-Boltzmann constant.

Monochromatic lasers emit light of a very narrow range of wavelengths (long coherence length). When integrating over a short range of wavelengths, the change in emissive power with wavelength can be neglected and the integral in Equation 5.6 can be approximated as

$$E = \int_{\lambda_1}^{\lambda_2} E_\lambda d\lambda \approx E_\lambda \Delta\lambda \tag{5.8}$$

$$E \approx \frac{2\pi hc^2 \lambda^{-5}}{\exp(\frac{hc}{\lambda k_B T})} \Delta\lambda \tag{5.9}$$

Two-color pyrometers are a type of ratio pyrometers that measure the temperature through the ratio of emissive power at two distinct wavelengths (more correctly the irradiance, as it is incident radiation, but also sometimes referred to as intensity, not to be confused with radiant intensity which has different units).

$$\frac{E_1}{E_2} = \frac{\varepsilon_1 \lambda_2^5 \Delta\lambda_1}{\varepsilon_2 \lambda_1^5 \Delta\lambda_2} \exp[\frac{hc}{k_B \lambda T}(\frac{1}{\lambda_2} - \frac{1}{\lambda_1})] \tag{5.10}$$

Taking the natural log of both sides yields

$$\ln(\frac{E_1}{E_2}) = \ln(\frac{\varepsilon_1 \lambda_2^5 \Delta\lambda_1}{\varepsilon_2 \lambda_1^5 \Delta\lambda_2}) \frac{hc}{k_B \lambda T}(\frac{1}{\lambda_2} - \frac{1}{\lambda_1}) \tag{5.11}$$

By neglecting the difference in emissivity at the the different wavelengths and grouping the terms in convenient constants, the expression reduces to

$$\ln(\frac{E_1}{E_2}) = \frac{A}{T} + B \tag{5.12}$$

where the constants $A = \frac{hc}{k_B \lambda T}(\frac{1}{\lambda_2} - \frac{1}{\lambda_1})$ and $B = \ln(\frac{\varepsilon_1 \lambda_2^5 \Delta\lambda_1}{\varepsilon_2 \lambda_1^5 \Delta\lambda_2})$ are found from calibrating against the known temperature of a blackbody radiation source. With known constants, and the emissive power ratio from the voltage output of the pyrometer, the temperature is found by solving Equation 5.12 for T.

5.3.1 Pyrometer calibration

To find the pyrometer constants A and B from Equation 5.12, the pyrometer was calibrated using a Process Sensors BBS1200 black body radiation source. The pyrometer constants are affected by the chosen bandpass filters (1705 and 1940 nm) of the pyrometer, as well as any other optical components in the path from the hot surface to the detectors. To obtain a high degree of accuracy of the temperature measurements, it is imperative that the calibration constants be found under similar conditions as the actual experimental

measurements. The calibration was done with a distance equal to that of the actual measurements, 140 mm from the front lens to the radiation source. A black body aperture size of 5.08 mm was used. This aperture size was found to be appropriate for calibration based on a sensitivity profile analysis described by Kink [55].

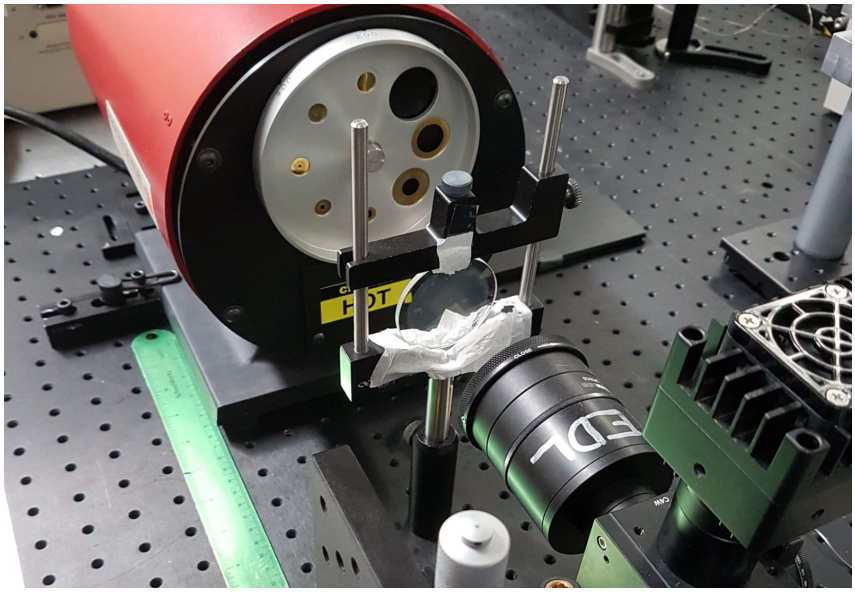

Figure 5.7: Pyrometer calibration setup.

The calibration constants are also affected by the baseline reading (dark current voltage or dark offset), due to background radiation and noise in the acquisition system. The baseline reading was recorded for each calibration point by blocking off the black body radiation source, and showed enough variation to affect the measurement accuracy. To avoid this effect, the baseline readings for each detector were subtracted from the signal before applying the curve fit and finding the constants. This resulted in the following expression for the temperature

$$T = \frac{A}{\ln(\frac{E_1}{E_2}) - B} \tag{5.13}$$

where T is the absolute temperature in Kelvin, E_1 is the reading from detector 1 (1940 nm) and E_2 is the reading from detector 2 (1705 nm), both with their respective baseline readings subtracted.

The temperature was ramped from 700 to 1150 °C in increments of 37.5 °C for a total of 13 calibration points. The constants were found to be $A = 1030$ and $B = -0.2886$, with 95% confidence intervals of $(1.025, 1.034)$ for A and $(-0.292, -0.2847)$ for B. The calibration curve is shown in Figure 5.8.

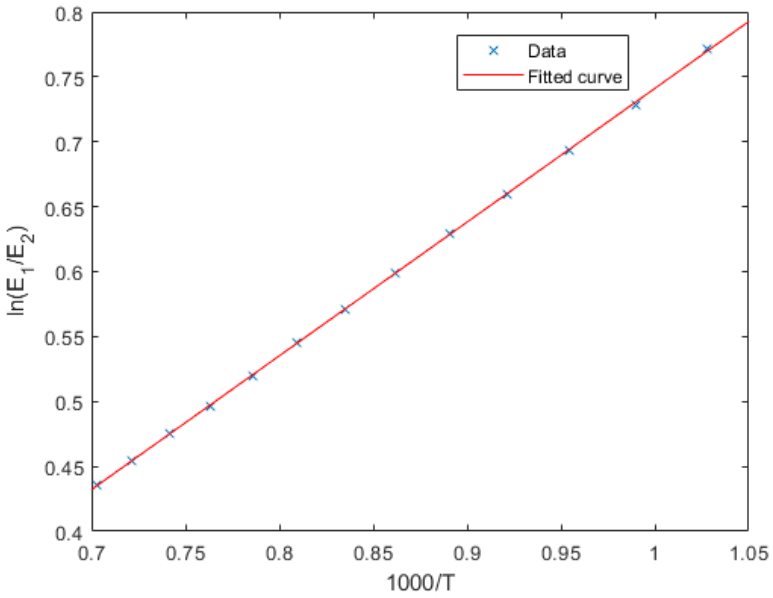

Figure 5.8: Calibration curve for two-color pyrometer.

5.3.2 Calibration and temperature measurement error sources

All optical components, such as windows, may affect the pyrometer temperature reading. After several shots, the window also gradually accumulates a layer of post-combustion particles, shown in Figure 5.9, that may further affect the reading. Previous studies by Boeck et al. [40] appear to report temperatures based on calibrations without the window in place and without accounting for the background intensity or particle accumulation.

To investigate the potential errors introduced by these factors, the pyrometer was calibrated with no window, a window with particles accumulated from 14 shots (dodecane shot 12-22 and JI unified surrogate shot 1-3), and a clean window, respectively. Two calibrations at equal conditions, but at different points in time were also compared to investigate the drift of the instrument with time. In all cases, the background intensity was taken into account and corrected for. The window position and tilt were also varied and found to have no observable effect for the small displacement distances and tilt angles in question.

The difference in measured temperature with and without the optical access window in place is shown in Figure 5.10. Although the signal intensity was noticeably reduced with the window in place, the ratio of the two wavelengths was nearly identical. Calibrating without the window resulted in a maximum difference of approximately 10 Kelvin compared to calibration with a clean window in place.

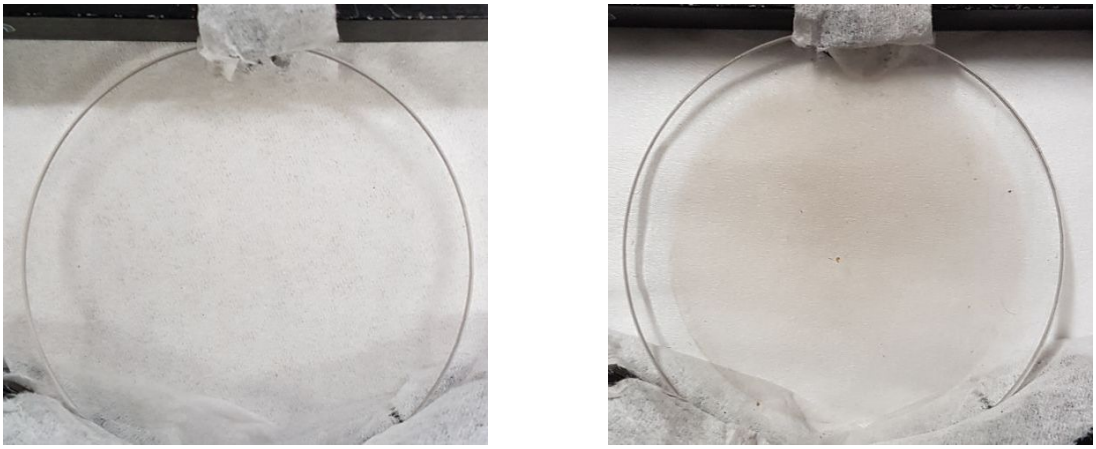

(a) Clean window (b) Dirty window

Figure 5.9: Clean (a) and dirty (b) optical access window.

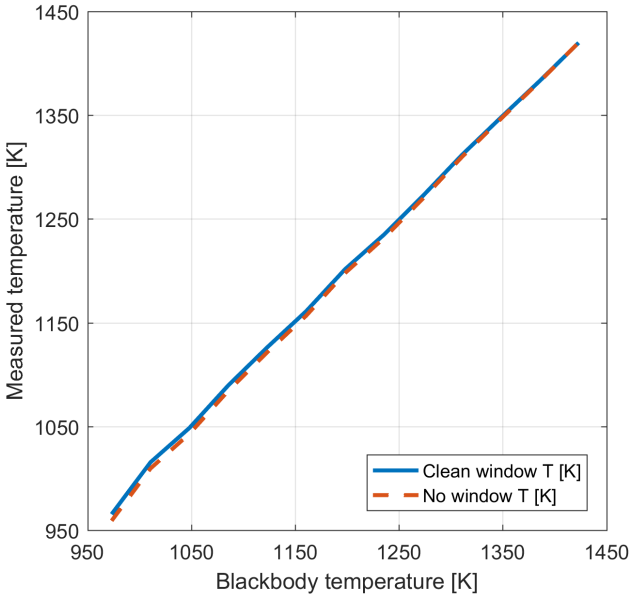

Figure 5.10: Measured temperature vs. black body temperature for a clean window and no window

The effect of accumulated particles on the reading is shown in Figure 5.11. The temperature difference due to the accumulated particles was negligible in the range of surface temperatures relevant for this work.

The most prominent difference in measured temperature was found to be between the calibrations taken before the first shot and after JI surrogate shot 3 (taken 56 days apart). This is shown in Figure 5.12.

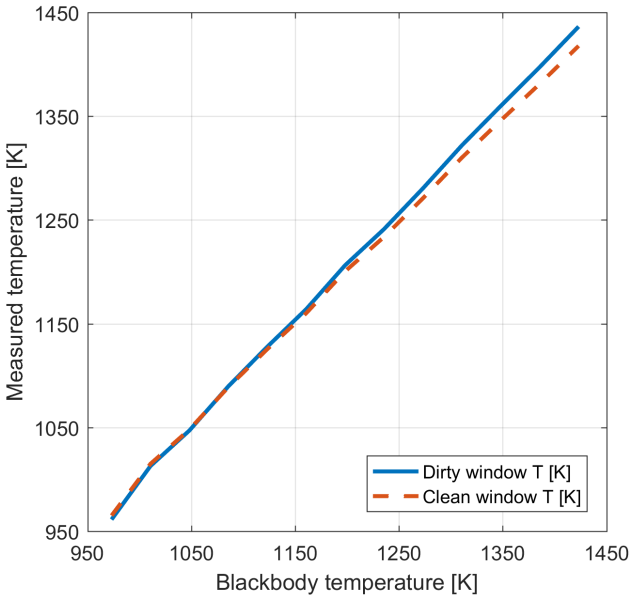

Figure 5.11: Measured temperature vs. black body temperature for a clean and dirty window

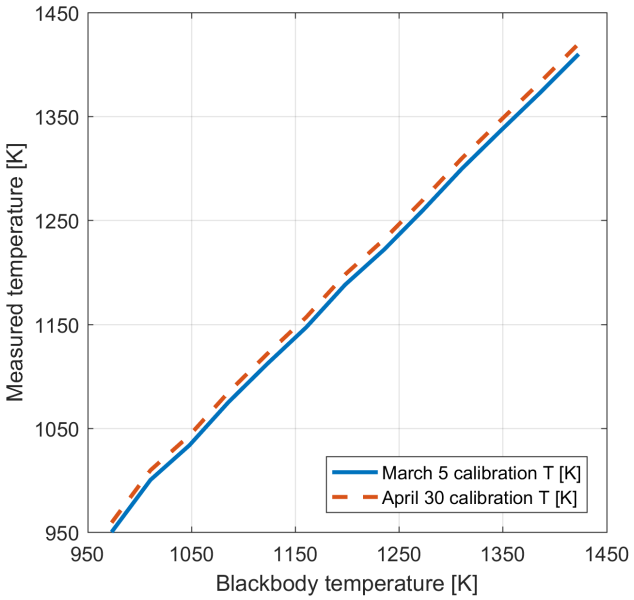

Figure 5.12: Measured temperature vs. black body temperature for calibrations at different points in time.

5.4 Mach-Zehnder Interferometer

Interferometry is an optical measurement method that utilizes the interference pattern created by two overlapping (superimposed) light beams (waves) to infer information about the system being studied. It is a widely used method across many scientific fields, such as physics, astronomy and chemistry.

The interferometer can be configured in several ways, depending on the application. Two common interferometer configurations are the Michelson interferometer and the Mach-Zehnder interferometer (MZI). The Michelson interferometer was used in the famous Michelson-Morley experiment of 1881 [63], but is still relevant today. Notably, a form of this configuration has also been used in more recent endeavors, such as the Laser Interferometer Gravitiational-Wave Observatory (LIGO) to detect gravitational waves [64].

The Mach-Zehnder (MZI) was developed by Ludwig Zehnder and Ludwig Mach in 1891 and 1892. It uses two beam splitters and produces two beams of interfering light. The MZI is extensively used for flow visualization due to it's flexibility; the fringes can be localized in any plane by adjusting the mirrors and beam splitters. It is a type of reference beam interferometer, where one beam propagates outside of the flowfield as a reference. For this type of interferometer, the beam separation is larger than the diameter of the field of view. The light from the light source (e.g a LASER of a certain wavelength) is split by a beamsplitter (semi-reflecting mirrors or cube), separating the test and reference beam. The test beam is turned by a fully-reflecting mirror and is led through the test section, while the reference beam is led around undisturbed. If a light source with a short coherence length is used, the reference beam is typically led through compensating glass plates to account for the large difference in optical path length induced by the test chamber windows. After the test section, the beams are recombined using another semi-reflecting mirror and focused onto a camera [65].

The interferometer mirrors and beamsplitters can be adjusted to control the width and orientation of the fringes. Achieving satisfacory alignment is an iterative process of subsequent mirror and beamsplitter adjustments. When the beams overlap perfectly (and the wavefronts are not distorted), no fringe pairs are visible - this is called the infinite fringe width configuration, and is good for flow visualization and as proof of good alignment. This mode is useful for qualitative images of the flow, but the precise alignment is very sensitive to outside disturbances, such as vibrations, and drifts easily. By further tilting the mirror, a path difference between the beams is induced, and a pattern of several fringe pairs is formed. This is called the finite fringe configuration. The fringes can appear horizontal, vertical or diagonal (depending on the position of the mirror). For more stability and ease of post-processing, the configuration was adjusted to achieve 40 horizontal fringe pairs.

The Mach-Zehnder interferometer set-up is shown in Figure 5.13. A collimated light beam is emitted from a 532 nm solid state laser (Spectra Physics Excelsior). The beam

is then expanded through two beam expanders for a total magnification factor of 180. Further, the beam is split in two by a cube beam splitter (BS1). The test beam goes through the test section (combustion vessel) and is turned 90 °by a flat mirror (M2). The reference beam is turned 90 °by another mirror (M1) and bypasses the test section undisturbed, before both beams are recombined in another cube beamsplitter (BS2). The recombined beam is then turned, focused by a 500 mm focal length lens and folded around to the camera by multiple flat mirrors. The lens was placed at a position such that the test section center plane was in focus, and a sufficient magnification was achieved. The interference pattern was captured by a Phantom V710 high speed camera.

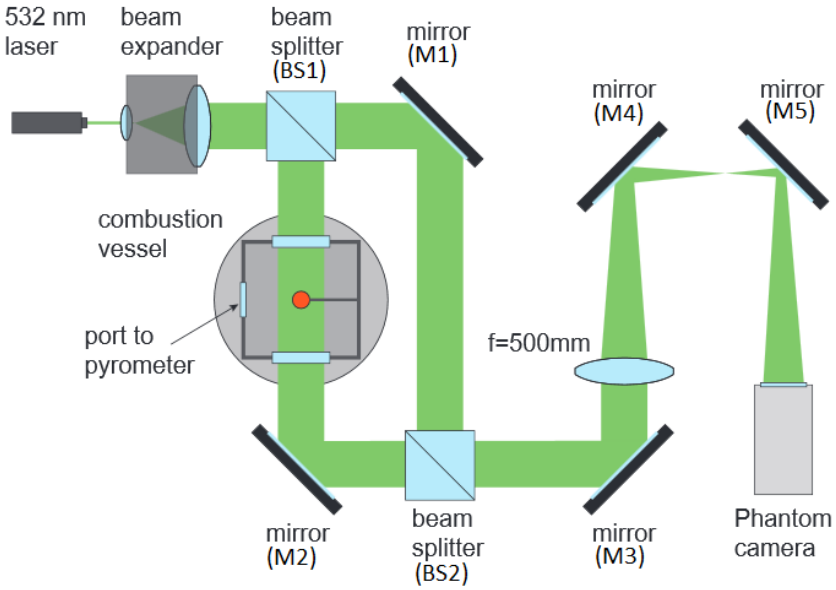

Figure 5.13: Mach-Zehnder interferometer set-up (adapted from [55]).

Error sources include misalignment of the plane walls (should be perpendicular to test beam) and the development of a secondary temperature field in the test chamber windows [65]. The resolution of the set-up was determined to be 7.13 line pairs per millimeter with a 1951 USAF Resolution Test Target. Using a ThorLabs R2L2S3P4 Grid Distortion target, the pixel density was found to be 15.75 ($\pm$0.05) pixels per millimeter with no significant distortion, as shown in Figure 5.14.

5.5 Interferogram post processing

The interferometer produces an image of the irradiance distribution of the interfering waves on the image plane. When the plane is perpendicular to the beam, the intensity is equal to the irradiance. The irradiance (or intensity) is given by

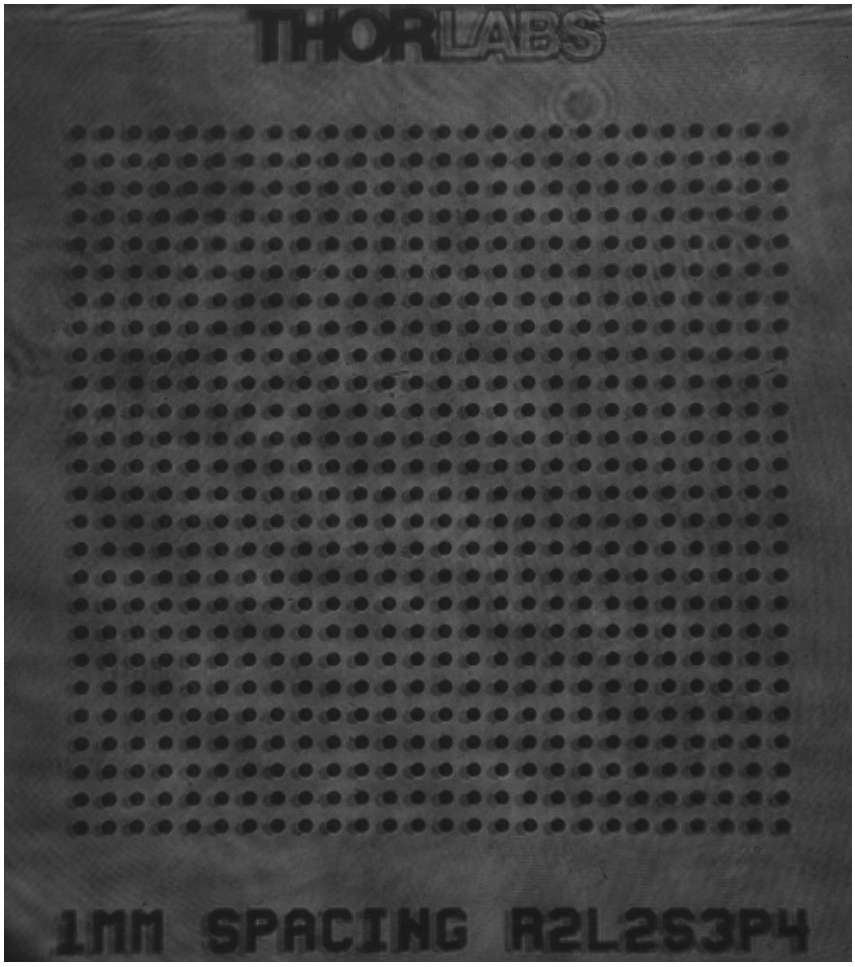

Figure 5.14: Grid distortion and pixel density test.

$$E = E_1 + E_2 + 2\sqrt{E_1 E_2}\cos(\Delta\varphi) \tag{5.14}$$

where E is the total irradiance, E_1 is the irradiance resulting from the reference beam, E_2 is the irradiance from the test beam and $\Delta\varphi$ is the optical phase difference. The last term is the interference term, and thus the total irradiance can be higher, lower or equal to the combined intensity of the two beams, depending on whether we have constructive or destructive interference [66].

From the interferograms, information about the temperature and density fields in the vessel can be inferred. The interferograms contain information about the phase difference between the test and reference beam, induced by the difference in index of refraction between the gas inside and outside the combustion chamber, given by

$$\Delta\varphi = \frac{2\pi}{\lambda}\int_{z_1}^{z_2}(n(x,y,z)-n_\infty)dz \tag{5.15}$$

where $\Delta\varphi$ is the optical phase difference between the disturbed and undisturbed beam (in the recording plane), λ is the wavelength of the light source (532 nm), $n(x,y,z)$ is the refractive index in the test section, n_∞ is the refractive index of the undisturbed reference beam, z is the direction of light propagation and z_1 and z_2 are the z-coordinates where light enters and leaves the test section [65].

At higher temperatures, the gas density decreases, which subsequently decreases the index of refraction of light passing through that gas. For gases, with a refractive index close to 1, this relation can be expressed by the abbreviated form of the Gladstone-Dale relation

$$n-1 = K\rho \tag{5.16}$$

where ρ is the density and K is the Gladstone-Dale constant (dimensions of $1/\rho$), which depends on the gas characteristics and the frequency or wavelength of the light source. This constant can be found from experiments or estimated from molecular data, and is commonly tabulated in physical chemistry literature. Selected K-values useful for combustion are shown in Table 5.1 [65].

Table 5.1: Gladstone-Dale constants for common combustion gases [65].

Gas	$K[cm^3/g]$	Wavelength [μm]	Temperature [K]
N_2	0.238	0.589	273
O_2	0.190	0.589	273
CO_2	0.229	0.589	273
H_2O	0.310	0.633	273
NO	0.221	0.633	295
CH_4	0.617	0.633	295

Due to the linear relationship between electric field vector and the dipole moment, the K-value for a gas mixture of density ρ can be found by

$$K = \sum_{i=1}^{N} K_i \frac{\rho_i}{\rho} \tag{5.17}$$

where K_i and ρ_i are the Gladstone-Dale constants and density of each individual species, respectively.

The density and temperature can be related by an equation of state, such as the ideal gas law

$$T = \frac{P}{\rho R_g} \tag{5.18}$$

where P is the total absolute pressure and R_g is the individual gas constant. For the pressure range in this work (10 Pa to 1 MPa), the ideal gas law gives good accuracy.

5.6 Laser schlieren imaging

To complement the interferometry data with a more direct visualization of the ignition dynamics, the interferometry set-up was changed to a laser schlieren setup. This was easily accomplished by blocking off the reference beam path and mounting a knife-edge device at the focal point before the camera. First, a razor blade was used, and then exchanged for a graded filter (fuzzy) to avoid light diffraction effects. The set-up is shown in Figure 5.15.

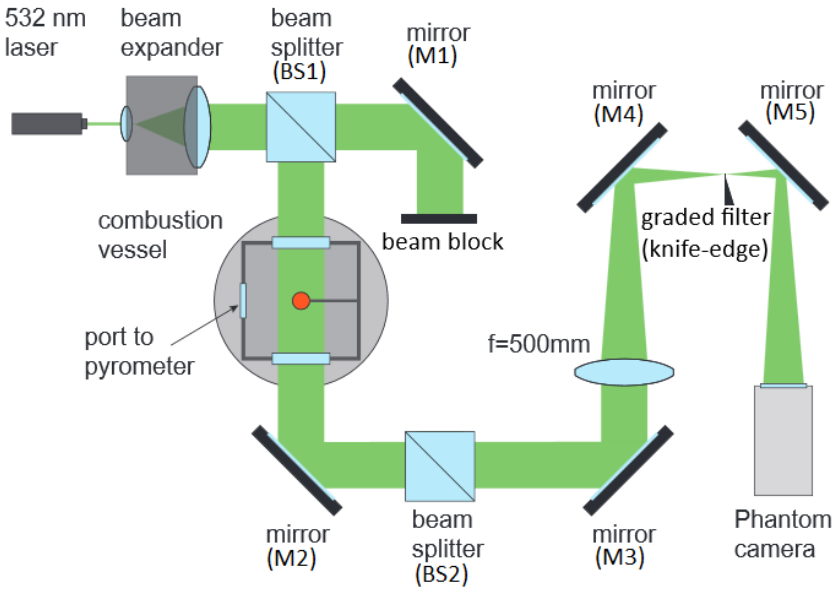

Figure 5.15: Laser schlieren set-up.

5.7 Acquisition and triggering

The pyrometer and Endevco pressure gauge signals were recorded using two oscilloscopes. The entire heating process, temperature and pressure history was recorded with a PicoScope 4424 digital oscilloscope (500000 samples total), and the high speed ignition transients were recorded with a Yokogawa DL850E ScopeCorder (50000 samples/s for 10 seconds), triggered by the ignition pressure rise. The trigger signal was fed to the Phantom V710 high speed camera for acquisition of interferograms of the ignition process.

5.8 General procedure

1. The vessel is heated so that all temperatures are at steady state above the dewpoint of the fuel-air mixture, typically above 130 °C (as read from TT1). The temperature should be roughly the same for each series of shots. The wall temperature must at no point exceed 200 °C (limit of Viton O-rings).
2. The vessel is evacuated to 10Pa, as read by the sensitive HEISE pressure gauge (PT2). Both pressure sensors are zeroed, and the range is checked and noted. This process is repeated to check for hysteresis.
3. The liquid fuel of known composition is injected through the side plate while the vessel is under vacuum. The resulting steady state partial pressure of surrogate fuel is recorded.
4. Premixed dry air is added through the piping system until the desired total pressure is obtained. NB: Valve V1 and V2 must be closed as soon as 1 atmosphere is reached to ensure a positive flow into the vessel and no loss of fuel to the piping system. All hand valves are closed.
5. The fuel-air composition is mixed with the magnetic stirbar impeller for 3 minutes and then allowed to settle for an additional 3 minutes.
6. After each shot, the vessel is evacuated and purged with air to remove combustion particles and cool the vessel to the initial temperature before the next shot.

The detailed shot checklist can be found in Appendix A.

6 Results

All ignition experiments were conducted with the cylinder in the vertical position, as shown in Figure 5.2. Time of ignition was defined based on high speed imaging, when the propagating flame was first visible. The time delay from visible ignition to the pressure trigger signal was found to be between 25 to 50 ms before the trigger signal. Figure 6.1 shows the defined ignition time interval for averaging the ignition temperatures (t_{ign}) along with the raw pyrometer temperature reading around ignition (dodecane shot 23). $t = 0$ indicates time of pressure trigger signal. The shown experiment was conducted using dry air (21.20 vol% O_2), at an equivalence ratio of $\phi = 0.95 \pm 0.068$, initial pressure of $P_0 = 101.3 \pm 0.1\text{kPa}$, and initial temperature of $T_0 = 130 \pm 5°\text{C}$.

As seen in Figure 6.1, the pyrometer output signal gave false surface temperature readidings during the ignition transient, so it was important that this portion of the signal be excluded when calculating the ignition temperature. In the time period of 25-50 ms before triggering, no significant jump in pyrometer signal was observed for the majority of the experiments. The ignition temperature was defined as the average of the temperature signal over this time interval. Experiments with very rich mixtures had a slightly longer trigger delay due to a slower pressure rise, and were adjusted accordingly.

The heating process and cylinder surface temperature history was captured with the PicoScope 4424 digital oscilloscope at 500000 samples over 1 minute and 40 seconds. At temperatures below 700 K, the signal-to-noise ratio was too low to measure the temperature. As the signal-to-noise ratio increased with temperature, the temperature reading accuracy increased, but significant variations in the raw signals were still observed. These variations are magnified in the temperature reading due to the $\log(V_1/V_2)$ term of Equation 5.12. Figure 6.2 shows the raw temperature data and a moving average with a window size of 500 samples. The temperature data are the same as from Figure 6.1 (dodecane shot 22). Note that the heating curves shown are based on temperature data collected from the PicoScope, and may differ slightly (± 10 K) from the more accurate Yokogawa ScopeCorder data used for calculating the final ignition temperatures.

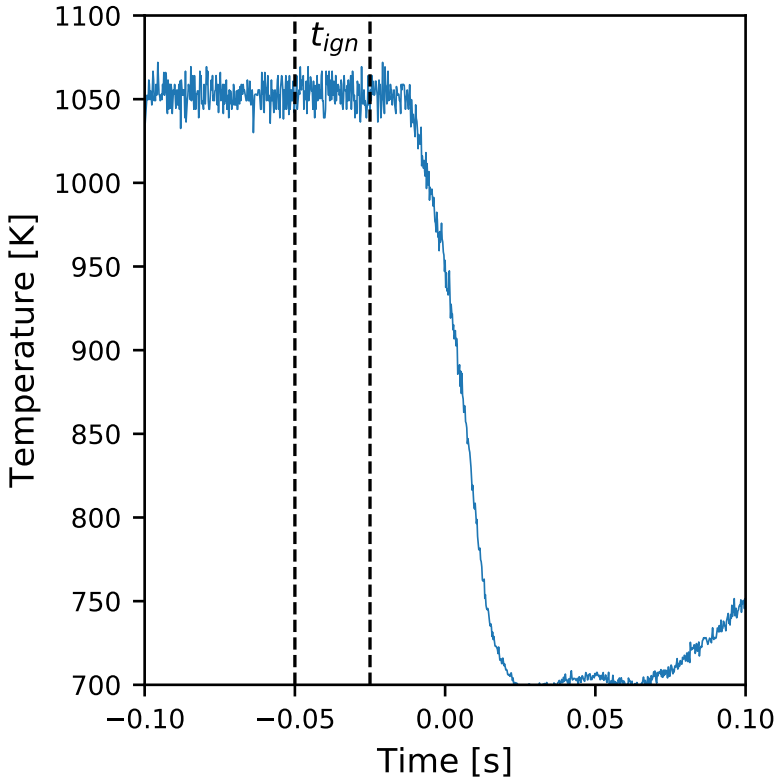

Figure 6.1: Ignition time definition based on high speed imaging and corresponding pyrometer temperature reading at ignition (dodecane shot 23). $t = 0$ indicates time of ignition pressure trigger signal, and t_{ign} is the time defined interval for averaging the ignition temperatures. Experiment conducted using dry air (21.20 vol% O_2), at an equivalence ratio of $\phi = 0.95 \pm 0.068$, initial pressure of $P_0 = 101.3 \pm 0.1$kPa, and initial temperature of $T_0 = 130 \pm 5$°C.

6.1 Ignition thresholds

6.1.1 Dodecane

The dodecane used in the experiments were Sigma-Aldrich ReagentPlus >99% Dodecane (sum of all isomers). Certificate of Analysis can be found in Appendix B. The dodecane was mixed with air at a pressure (P_0) of 101.3 ± 0.1kPa and allowed to settle to starting temperatures (T_0) of 130 ±5 °C before turning on the power supply to heat the ignition cylinder. Before ignition, the temperature would increase by up to ≈4 K and 1 kPa due to the cylinder heating. The power and heating rates ranged from 90 W to 130 W, and 11 $\mathrm{K\,s^{-1}}$ to 14.3 $\mathrm{K\,s^{-1}}$ (average over the first 45 seconds of heating), $T_0 = 132 \pm 4$°C, $P_0 = 101.3 \pm 1.0$kPa. For ignition events, the heating time was between 1 to 1.5 minutes, with the majority of ignition at the 1 minute mark. For non-ignition events, the cylinder

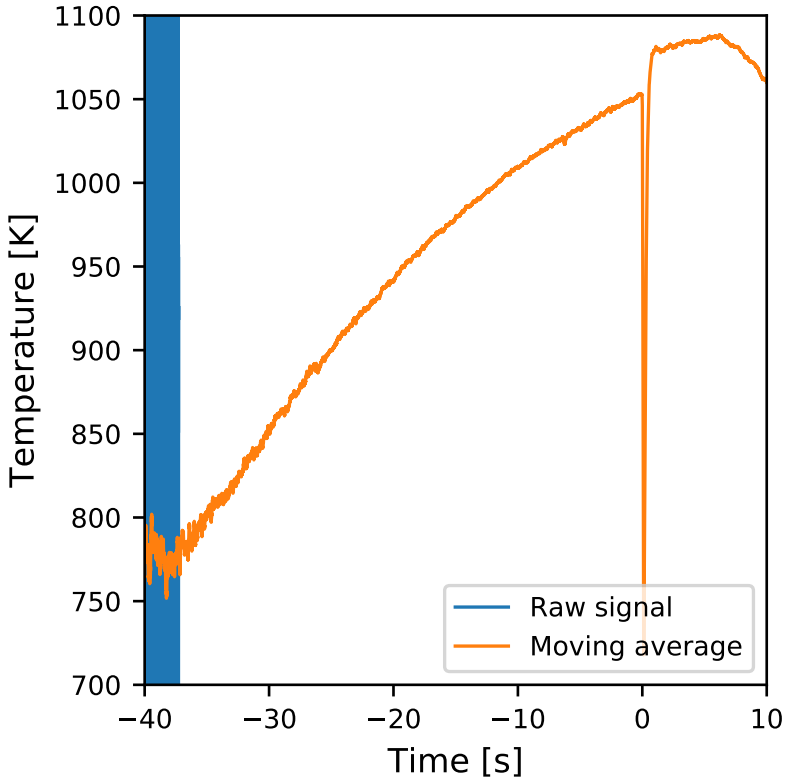

Figure 6.2: Raw and moving average temperature signals (dodecane shot 23). Moving average window size was 500 samples. $t = 0$ indicates time of ignition pressure trigger signal. Experiment conducted using dry air (21.20 vol% O_2), at an equivalence ratio of $\phi = 0.95 \pm 0.068$, initial pressure of $P_0 = 101.3 \pm 0.1$kPa, and initial temperature of $T_0 = 130 \pm 5$°C.

was run for up to 3 minutes, with a minimum heating period of 2 minutes. The resulting ignition temperature threshold data are shown in Figure 6.3.

The ignition temperature showed no clear dependence on stoichiometry within the flammability limits. The observed variation was largely due to differences in heating rates, as discussed in 7.2. The average ignition temperature over all experiments ($n = 26$) was 1020 K ($s = 27$ not including other sources of variability). The minimum ignition temperature observed was 977 K at $\phi = 1.47 \pm 0.068$, and the maximum was 1067 K at $\phi = 0.95 \pm 0.068$. Around stoichiometric conditions ($0.5 < \phi < 1.5$) the minimum ignition temperature was 997 K. All stated temperatures have an uncertainty of 3-5% of the measured value, $\approx \pm 50$ K.

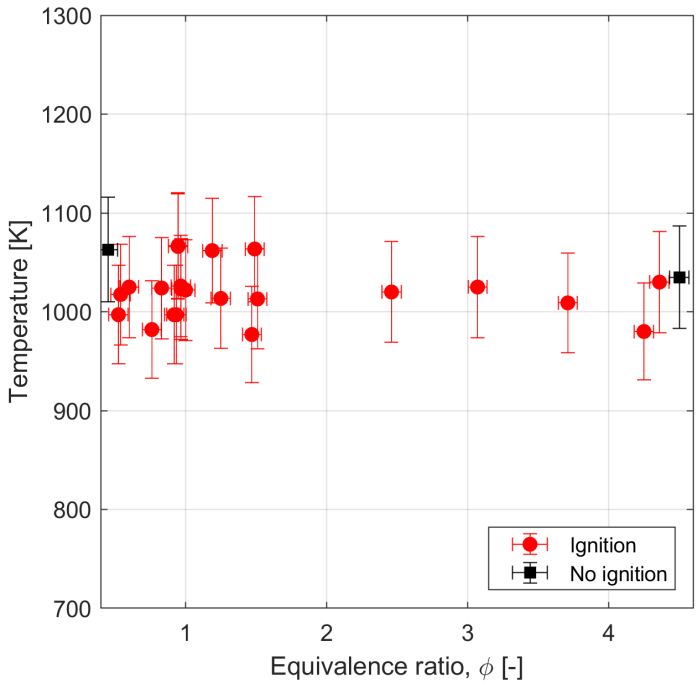

Figure 6.3: Ignition temperature thresholds for dodecane (Sigma-Aldrich ReagentPlus >99%) mixed with dry air (21.2 mol% O_2) at $T_0 = 130 \pm 5$°C, $P_0 = 101.3 \pm 0.1$kPa. Heating rate of 90 W to 130 W, and 11 $K s^{-1}$ to 14.3 $K s^{-1}$ (45 second average).

6.1.2 Aachen surrogate

The Aachen surrogate [50] (80% n-decane, 20% trimethylbenzene by weight) was mixed with dry air (21.20 mol% O_2) to an initial pressure (P_0) of 101.3 ± 0.1kPa and settled to an initial temperature (T_0) of 138 ±2 °C. The additional temperature rise was similar to that for dodecane (≈4 K and 1 kP). The heating power was 95 W to (130 ± 1) W, and 10.7 $K s^{-1}$ to 14.4 $K s^{-1}$ (45 second average), with the ignition events at the higher end of the power and heating rate range (130 ± 1 W). All ignition close to stoichimetric happened within 1 min ±5 seconds, while richer mixtures ($\phi > 3$) had heating times up to 1 min 28 seconds. For non-ignition events, the cylinder was run for 2-3 minutes.

The ignition temperature thresholds for the Aachen surrogate are shown in Figure 6.4. The equivalence ratio error (±0.022) is smaller than the marker size and is omitted.

As for dodecane, the observed temperature of ignition for the Aachen surrogate was nearly independent of fuel concentration around stoichiometric conditions ($0.75 < \phi < 1.25$). In this range, the mean ignition temperature ($n = 6$) was 1061 K ($s = 2.6$). Unfortunately, the ignition cylinder quartz housing cracked under thermal load after several shots, introducing the possibility of thermal leaks. Therefore, only one valid ignition point was included

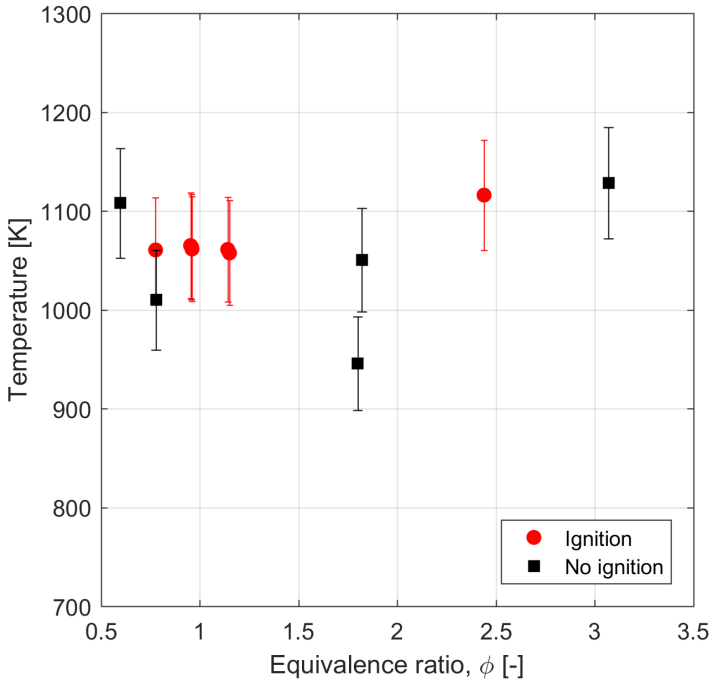

Figure 6.4: Ignition temperature thresholds for Aachen surrogate (80/20 wt% n-decane/TMB) mixed with dry air (21.2 mol% O_2) at $T_0 = 138 \pm 2$°C, $P_0 = 101.3 \pm 0.1$kPa. Heating rate of 95 W to (130 ± 1) W and 10.7 K s^{-1} to 14.4 K s^{-1} (45 second average).

in the rich regime. However, this data point ($\phi = 2.44 \pm 0.022$) indicates a higher ignition temperature (1122 K) in this regime, and the ignition dynamics were characterised by a very weak pressure transient and puffing flame behavior. It is also worth noting that the UFL calculated from Le Chatelier's mixing rule is 5.6 mol% fuel, which corresponds to an equivalence ratio of 4.15. Thus, the non-ignition event at $\phi = 3.07 \pm 0.022$ further indicates that there is more ignition variability at rich conditions, that an increased temperature is required, or an overestimation of the upper flammability limit. However, due to the low number of valid experiments in the rich regime, this is purely an indication, and more tests are required to draw any definite conclusions.

6.1.3 JI Unified surrogate

A limited number of shots ($n = 3$) were performed with the JI Unified surrogate. The ignition experiments were performed following dodecane shot 17-22. Both series were performed with the same cylinder and a constant current of 7 A, at a comparable heating rate of around 115 ± 1 W, and 12.6 ± 0.2 K s^{-1}. A comparison between the dodecane and JI surrogate heating curves at comparable heating rates are shown in Figure 6.5. For

clarity, only shots of similar equivalence ratios (dodecane shot 18,21,22 and JI shot 1,2,3) are shown, but all dodecane shots in this series showed similar heating curves.

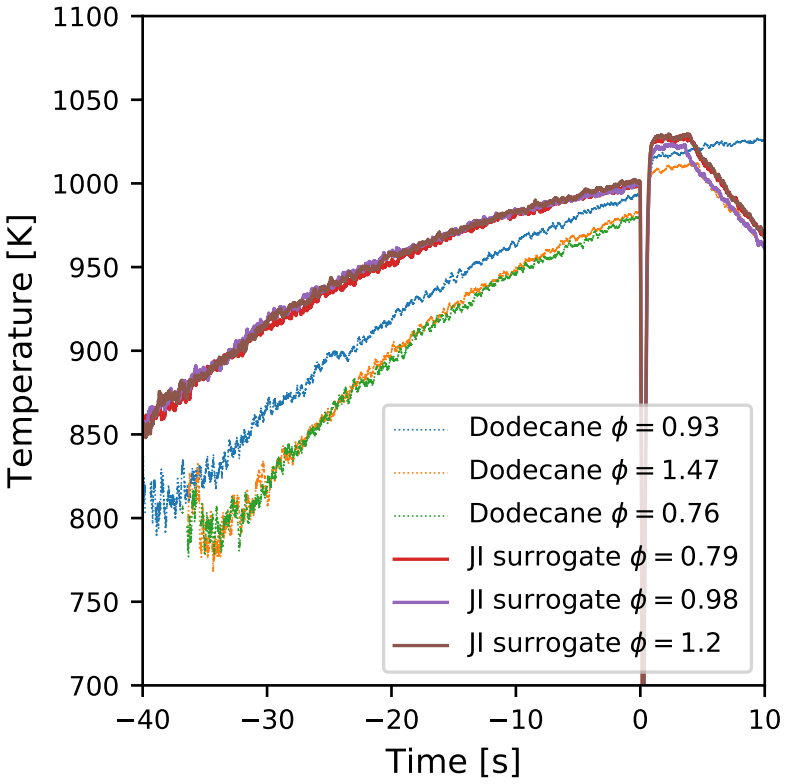

Figure 6.5: Heating curves for similar equivalence ratios of dodecane and JI surrogate ignition at heating rates of $115 \pm 1\,\mathrm{W}$ and $12.6 \pm 0.2\,\mathrm{K\,s^{-1}}$ (45 second average). $t = 0$ indicates time of ignition (pressure trigger). All experiments conducted in dry air (21.20 vol% O_2) at $P_0 = 101.3 \pm 0.1\mathrm{kPa}$

A slightly faster initial surface temperature rise and smaller slope at ignition was observed for the JI surrogate. This could be explained by increased resistance due to oxidation of the coil, but a systematic trend of increasing temperature rise with shot number was not observed for the dodecane experiments. Similar variation was also observed between dodecane shots, as seen for dodecane shot 17 ($\phi = 0.93 \pm 0.022$) compared to shot 21 and 22 ($\phi = 1.47$ and $\phi = 0.76$, respectively), where later shots showed decreased temperature. The resulting ignition thresholds for the JI surrogate are shown in Figure 6.6.

The ignition temperature for the three shots in the vicinity of the stoichiometric limit showed high repeatability. The average ignition temperature ($n = 3$) was 1002.5 K ($s = 4$) with a minimum of 999 K and a maximum of 1006 K.

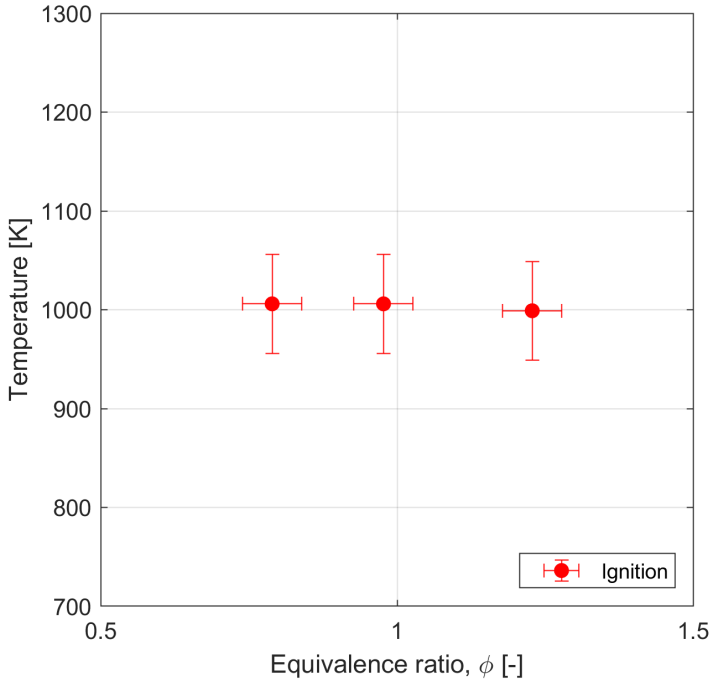

Figure 6.6: Ignition temperature thresholds for JI Unified surrogate.

6.2 Ignition dynamics

The ignition events were captured with high-speed Schlieren images and Mach-Zehnder interferograms, as described in Section 5.6 and 5.4, respectively.

All shots were performed with the cylinder in the vertical direction. Based on a model by Laurendeau [22], Boeck [40] predicted the point of ignition to be at the top of the vertical cylinder. At this point, the residence time of a gas particle flowing along the heated surface, and the thickness of the boundary layer are both at a maximum. In this work, the point of ignition was consistently observed to be near the top of the cylinder, at 85-90 % of the full cylinder length. Along the circumference of the cylinder, the point of ignition varied between each experiment. This is consistent with the dynamics reported in [40].

Figure 6.7 compares the time evolution of three dodecane flames (shot 7, 8 and 10) of increasing equivalence ratio. Ignition at equivalence ratios from the lower flammability limit up to $\phi = 3.7$ were characterised by a single flame propagating at high speed with a sharp outer boundary gradient (6.7 a-f). The flame propagated spherically outwards, with some stretching in the vertical direction due to buoyancy, until it occupied the entire geometry of the vessel (6.7 a-b). Subsequent reflection and formation of cell structures is shown in (6.7 c-d). Ignition of richer mixtures (6.7 c-h) was also characterised by

a single flame, but with significantly slower propagation speed, a less sharply defined boundary, and visible deformation of the flame. At very rich conditions ($\phi > 3.7$) to the upper flammability limit, puffing flame behavior was observed (6.7 i-l). Puffing flames are continuous flames affected by large scale instabilities caused by expansion, buoyancy, and vorticity in the flow field. The flame initially expands rapidly, but radial expansion is halted (6.7 i-j) and the flame is carried upward and deformed by buoyancy (6.7 k-l). A new flame is then generated at the surface, and the pattern repeats for several cycles. Puffing flames were also observed in rich hexane ignition experiments [54][41], and a detailed treatment of the phenomenon can be found in [41].

The ignition pressure transients of each experiment was measured by the high frequency (>10000 samples per second) Endevco pressure transmitter and captured at 50000 samples per second by the Yokogawa ScopeCorder. Figure 6.8 shows the pressure transients for dodecane ignition for increasing equivalence ratios, ranging from $\phi = 1.49$ to $\phi = 4.36$. The transient for $\phi = 1.49$ (solid blue line) is characteristic of single flame propagation at high flame speeds. This mode was observed for all experiments around stoichiometric conditions ($0.5 < \phi < 1.5$).

Figure 6.9 shows the peak pressure for the Aachen surrogate as a function of equivalence ratio. The adiabatic constant volume pressure ($UV = \text{const}$) between the upper and lower flammability limit was calculated using Cantera [27] and the JetSurf2.0 [23] model modified by Mertens and Manion [67] to include trimethylbenzene kinetics.

As seen in Figure 6.4, the measured pressure is significantly lower than the adiabatic constant volume computation, due to heat loss from the gas to the vessel. As the equivalence ratio increases and flame speed decreases, the total losses also increase due to increased time available for heat transfer. This, in addition to the increased formation of soot and soot precursors on the rich side explain why the discrepancy between measurements and adiabatic simulations increases with equivalence ratio.

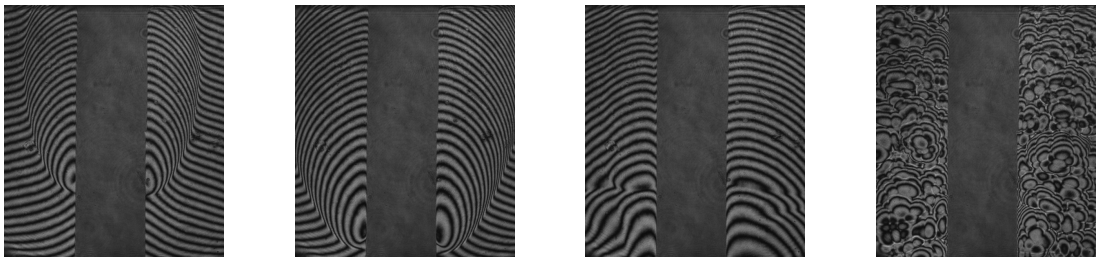

(a) $\phi = 1.51$, $t = t_{ign} + 3.0$ms
(b) $\phi = 1.51$, $t = t_{ign} + 6.0$ms
(c) $\phi = 1.51$, $t = t_{ign} + 16.0$ms
(d) $\phi = 1.51$, $t = t_{ign} + 50.0$ms

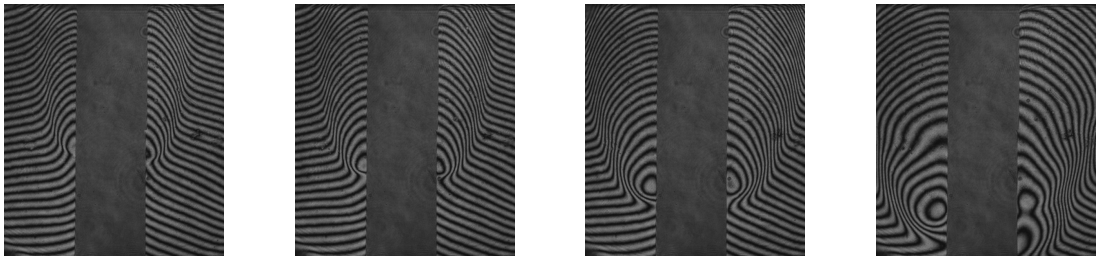

(e) $\phi = 3.07$, $t = t_{ign} + 3.0$ms
(f) $\phi = 3.07$, $t = t_{ign} + 6.0$ms
(g) $\phi = 3.07$, $t = t_{ign} + 16.0$ms
(h) $\phi = 3.07$, $t = t_{ign} + 50.0$ms

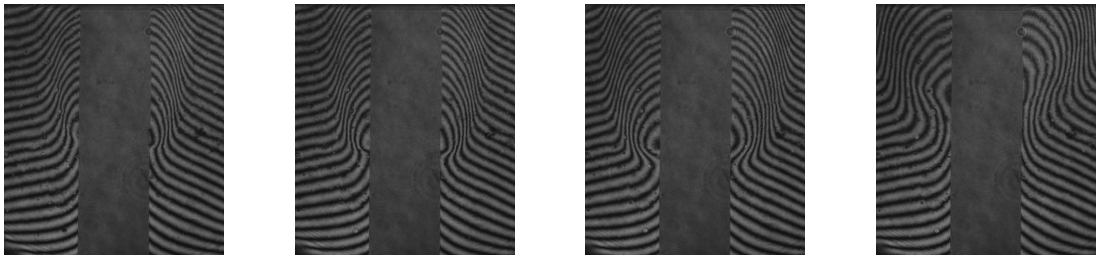

(i) $\phi = 4.36$, $t = t_{ign} + 3.3$ms
(j) $\phi = 4.36$, $t = t_{ign} + 6.0$ms
(k) $\phi = 4.36$, $t = t_{ign} + 16.0$ms
(l) $\phi = 4.36$, $t = t_{ign} + 50.0$ms

Figure 6.7: Dodecane ignition dynamics comparison for fast, slow, and puffing flame dynamics.

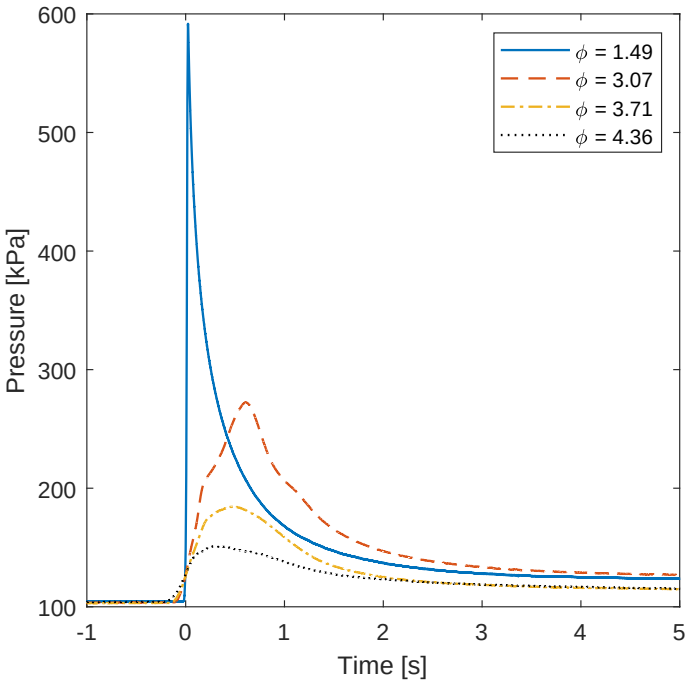

Figure 6.8: Dodecane ignition pressure transients for increasing equivalence ratios.

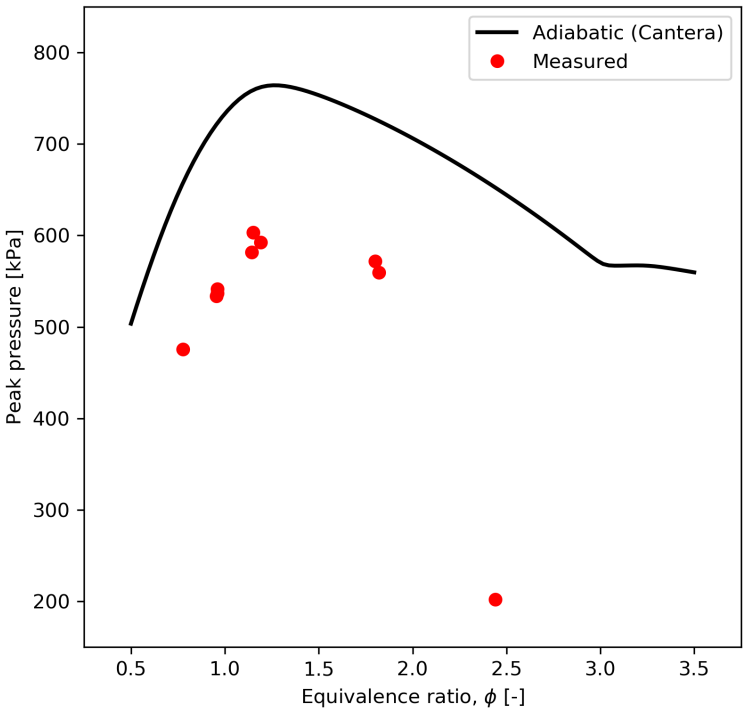

Figure 6.9: Aachen surrogate peak pressure as a function of equivalence ratio from adiabatic constant-volume Cantera simulations and measured peak pressures.

7 Discussion

7.1 Error sources

The ignition temperature has several sources of error. Most notably:

- Surface variation (≈ 3-5 % of measured T) [40].
- Pyrometer measurement variation at time of ignition (±5 K for the Yokogawa ScopeCorder data).
- Ignition time and averaging variation (less than 5 K difference for averaging windows above 50).
- Calibration variation (less than 10 K difference)
- Calibration fit uncertainty (approx. 12 K difference)

The pyrometer error is dominated by the surface variation observed, and thus a conservative general error of 5% has been adopted for the reported ignition temperatures.

The fuel concentration uncertainty is affected by uncertainties in:

- Injection volume
- Vessel volume
- Temperature at time of mixing with air
- Pressure at time of mixing with air
- Liquid fuel composition and density

For the Dodecane shots, a Perfektum 0.25 ml syringe with an estimated uncertainty of ±5 µl was used. For the surrogate shots, a Hamilton Gastight 100 µl syringe was used instead, with an uncertainty of ±0.5 µl. Conservative uncertainty estimates for the temperature and pressure at time of mixing fuel-air are ±3 K and ±0.1 kPa. Sensitivity tests for the equivalence ratio showed an error of ≈±0.033 (7.47%) at the lean test conditions (75 microliters, $\phi = 0.442$), and ±0.068 (1.51 %) at the rich conditions (730 microliters, $\phi = 4.495$). The largest absolute error of ±0.068 was chosen as a conservative estimate for all dodecane equivalence ratios. For the Aachen and JI surrogate, using the Hamilton

Gastight 100 µl syringe, the sensitivity test showed that the maximum absolute error was significantly lower at ±0.022 (rich conditions), that was applied to all equivalence ratios.

It is important to note that the ignition temperature is also heavily dependent on other factors, such as the thermal losses (vessel volume and geometry) and the flow conditions in the vessel. The presence of stagnation points near the heated surface reduce the ignition temperature significantly [40]. Thus, the reported ignition temperatures are only valid for conditions similar to those described in this work.

7.2 Heating rate dependence

Multiple series of experiments for the same fuel were performed at different heating rates. The ignition temperatures for each series were highly repeatable, but differed significantly from the other series. For experiments using dry air, the ignition temperature was found to be systematically dependent on the heating rate and temperature history. This has also been observed in other studies [22]. Figure 7.1 shows the temperature history of two series of Dodecane (Sigma-Aldrich ReagentPlus >99 mol%) ignition experiments, highlighting the difference in ignition temperature at different heating rates. The first series of 4 shots (17,18,19,21) was conducted with $115 \pm 1\,\mathrm{W}$ of heating effect, resulting in a heating rate of $12.7 \pm 0.2\,\mathrm{K\,s^{-1}}$ (average over 45 seconds, pyrometer uncertainty not taken into account). The second series (23-26) was heated at $130 \pm 1\,\mathrm{W}$ and $14.1 \pm 0.2\,\mathrm{K\,s^{-1}}$. Time $t = 0$ indicates time of ignition (pressure trigger). The experiments were all conducted using dry air (21.20 vol% O_2), at equivalence ratios of $0.5 < \phi < 1.5$, initial pressures of $P_0 = 101.3 \pm 0.1\mathrm{kPa}$, and initial temperatures of $T_0 = 130 \pm 5°\mathrm{C}$ (internal thermocouple, TT1). The total heating time before ignition was the same for both series (1 min ±5 seconds). The first 20 seconds of heating is not shown because the pyrometer signal to noise ratio was too low to measure accurate temperatures below 750 K.

Because of the apparent dependence on heating rate, the ignition temperature for different fuels should only be compared at equal heating rates. Figure 7.2 compares dodecane (shot 24 and 26) and Aachen (shot 5 and 6) ignition at similar heating rates and equivalence ratios. Note that the heating curves for equal equivalence ratio (green and blue for $\phi \approx 0.95$, red and and orange for $\phi \approx 1.5$) are barely distinguishable due to the close overlap.

As seen in Figure 7.2, similar heating curves resulted in very similar ignition temperatures for the two fuels around stoichiometric conditions. At comparable heating rates, the ignition temperatures were also found to be nearly independent of equivalence ratio between the lower and upper flammability limits for all fuels studied. Further experiments should be conducted to reveal if the fuel ignition behavior diverges for other heating rates and richer conditions.

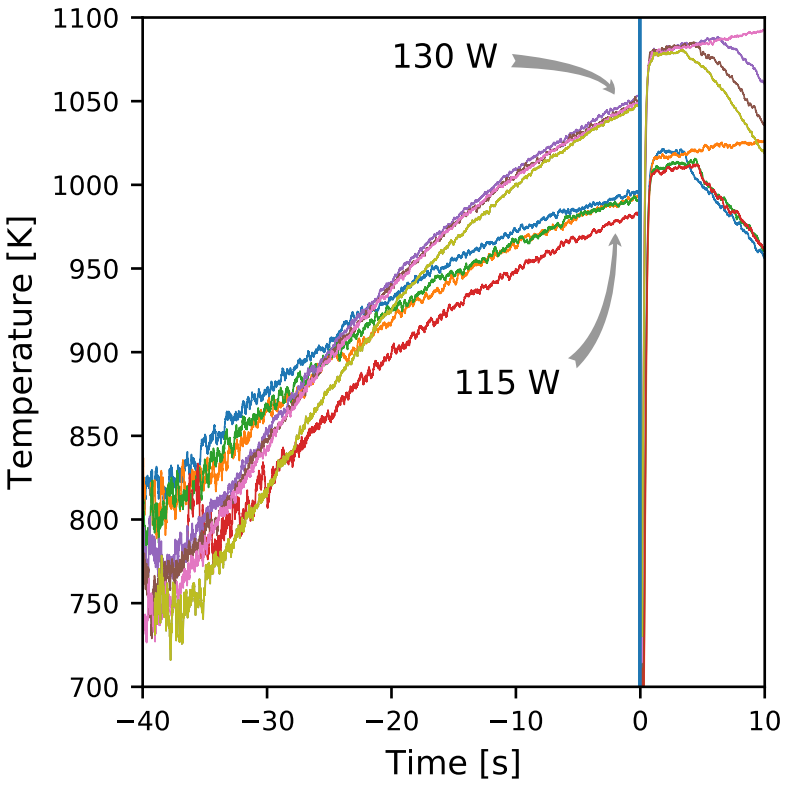

Figure 7.1: Dodecane (Sigma-Aldrich ReagentPlus >99 mol%) ignition series at heating powers of 115 ± 1 W and 130 ± 1 W. $t = 0$ indicates time of ignition pressure signal. The experiments were all conducted using dry air (21.20 vol% O_2), at equivalence ratios of $0.5 < \phi < 1.5$, initial pressures of $P_0 = 101.3 \pm 0.1$kPa, and initial temperatures of $T_0 = 130 \pm 5$°C.

Most dodecane-dry air mixtures of equivalence ratios below 3 ignited after 1 minute (±5 seconds) of cylinder heating, even for different heating rates. At higher equivalence ratios, or when atmospheric air containing moisture was used, more variability was observed, with ignition taking place between approximately 1 to 2 minutes of heating. Higher heating rates resulted in higher surface temperatures measured at time of ignition.

Figure 7.1 shows that increased heating and a faster temperature rise lead to higher surface temperature at ignition. From the Van't Hoff ignition criterion, a higher temperature and heat flow increases the ignition criterion. By examination of Equation 1.39, we can see that the criterion on the left hand side scales by ΔT^2. However, the right hand side scales with $k_r {T_w}^2$, and therefore dominates at higher T_w. Thus, the observed phenomenon cannot be explained by the predictions of simple thermal theory considering only global reaction kinetics and conduction.

From the more detailed kinetics outlined in Section 1.3, we know that the ignition is initiated by thermal cracking of the fuel, with H-atom abstraction and C-C fission identified

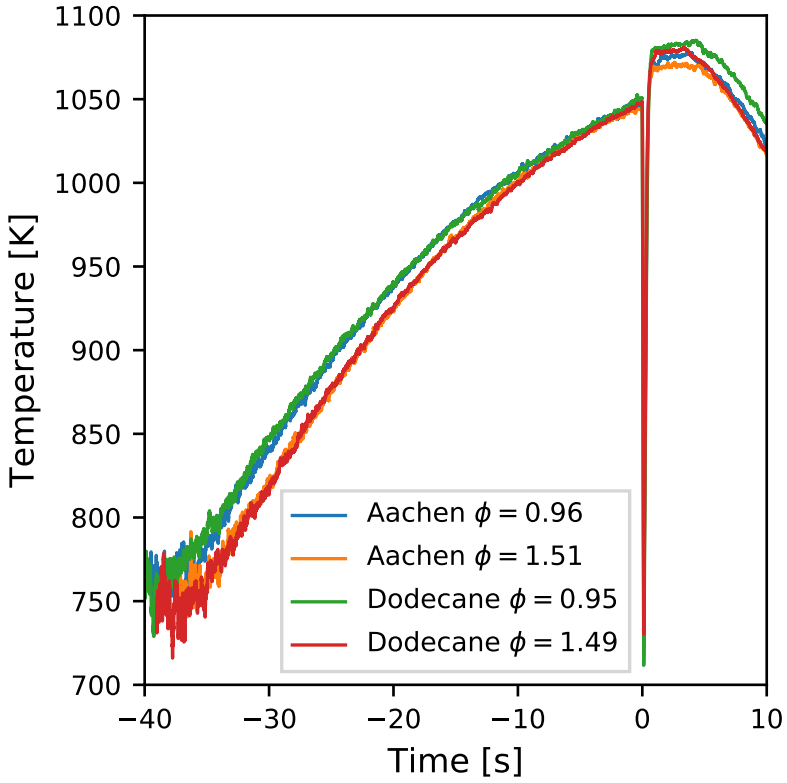

Figure 7.2: Heating curves for similar equivalence ratios of dodecane and Aachen surrogate ignition. $t = 0$ indicates time of ignition. All experiments conducted in dry air (21.20 vol% O_2) at $P_0 = 101.3 \pm 0.1$kPa

as limiting steps. Thermal cracking requires high temperatures and residence times to initiate and build a pool of radicals and lower species that subsequently oxidize. Above the minimum temperature threshold for pyrolysis, some minimum time must pass for the radical pool to build to a critical mass. The conversion of the fuel is generally governed by the Damkohler number ($Da = \tau_{\text{flow}}/\tau_{\text{chem}}$), where a high number indicates higher conversion.

High heating rates lead to higher temperatures, but also increased flow velocity of fluid parcels in the plume boundary layer. A possible contributing factor to the observed increased ignition temperture at higher heating rates is that a higher flow velocity in the thermal plume leads to shorter residence times of fluid parcels near the hot surface, counteracting the temperature effect on Da and thus fuel conversion. If this were the case, we may also expect the effect of heating to be less pronounced for the horizontal direction, where stagnation points are present. Boeck et al. [40] found the ignition temperature to be significantly lower in this orientation. Their results also indicated that the ignition temperature of fuels with more direct oxidation pathways (such as H_2) were less sensitive

to orientation compared to pyrolysis-governed fuels (such as hexane), which could be interpreted as increased importance of residence time for high carbon number alkanes. However, it should be stressed that this is not the only possible explanation for their observed results.

For forced convection, the increase of ignition temperature with increased velocity is well documented [22]. The residence time is inversely proportional to velocity, and the Damkohler number can alternatively be expressed as $Da = \frac{k_r L}{u}$. Thus, the evolution of u as a function of T_w for natural convection is of interest to investigate the effect on Da. For a surface temperature of $T_w = 1000\text{K}$ and $T_\infty = 400\text{K}$, using property values for air at the film temperature $(T_w + T_\infty)/2$, the Grashof number was calculated as $Gr = 1800$ from Equation 1.52. Hence, the flow was laminar over the entire cylinder length according to Criteria 1.61. Further, $Gr_L Pr < 10^4$, and thus the boundary layer approximations are not strictly valid according to Criteria 1.60. The right side of Criteria 1.62 was evaluated as ≈ 5, which is on the order of, but not strictly less than the aspect ratio of 1. However, from interferograms, the thermal boundary layer is visibly thinner than the diameter, and hence the flow boundary layer will be so as well for $Pr < 1$. The Prantl number was below 1 for all temperatures studied, and thus the flat plate assumption is valid. Despite the boundary layer assumptions and the assumption of no heat generation in the boundary layer being strictly invalid, for qualitative purposes, the x-velocity component u in the boundary layer was found by solving the Ostrach system of Equations 1.58-1.59 for wall temperatures of $600\,\text{K}$ to $1000\,\text{K}$. In this range, power law scaling was found for u as a function of T_w, but the velocities were still small for the short cylinder length in question. At the point of ignition observed from the interferograms, ($x = 0.9L$ and 1 mm from the surface in the y-direction), u increased from $0.4\,\text{m}\,\text{s}^{-1}$ to $2\,\text{m}\,\text{s}^{-1}$. This was outscaled by the Arrhenius exponential at high temperatures leading to $Da > 1$ over 650 K using global dodecane combustion kinetics. The same result is expected for detailed kinetics. Moreover, thermal cracking conversion timescale of n-dodecane around 1000 K has been found to be on the order of milliseconds at well-mixed conditions [17]. The residence time of the gas in the hot layer close the the cylinder wall was found to be above that at all conditions assuming the relevant gas particles follow a path close to the wall along the entire length of the cylinder. However, the path of the fluid parcels relevant for ignition could be very different, and numerical simulations resolving the real flow conditions should be performed to evaluate the residence time along the real streamline.

Another effect that could potentially increase the observed ignition temperature is increased convective losses to the gas outside the boundary layer at higher velocities. However, at the velocities found for this case, this effect is expected to be small. This is supported by a an order of magnitude analysis at similar temperatures and geometry (glowplug at 950 K) performed by Boettcher [41], where the convective heat losses were found to be an order of magnitude lower than the conductive and diffusion terms.

Previous work at EDL [68], [69] found ignition to be of a stochastic nature at a cer-

tain temperature range, even for seemingly identical conditions. From a large number of observations at equal conditions, a logistic regression can be fitted to find the probability of ignition as a function of temperature. Due to reliability issues with the ignition device, namely wire burnout and cracking of the quartz components, the number of observations at equal conditions was too low for this analysis to be meaningful. The low number of observations at identical conditions, combined with the temperature measurement uncertainty of ± 50, makes it hard to draw definite conclusions from the data, and no convincing argument can be drawn from simplified analysis. In future work, the observed increased ignition temperature with heating rate phenomenon and the underlying mechanisms controlling the temperature-history dependence should be investigated further through additional, well controlled tests and detailed numerical simulations.

7.2.1 Atmospheric vs dry air

The combustion experiments in this work were mainly performed using premixed dry air (Airgas Ultra Zero grade) as the oxidizer at standard atmospheric pressure, approx. (101.3kPa). Previous studies with the vessel[40], [41] were conducted using synthetic dry air mixed from industrial grade oxygen and nitrogen. For real safety applications, the air will often be at local atmospheric conditions, and will contain some moisture that may affect the ignition threshold. The presence of moisture is expected to increase the OH-radical generation, as outlined in Section 1.3. To investigate this effect, the results from experiments conducted using air at local atmospheric conditions were compared to the those from dry air experiments. At similar heating rates, the measured ignition temperature for dry air were lower than for moist air. At a similar equivalence ratio of $\phi = 1.5$, and heating rate of $12.8\,\mathrm{K\,s^{-1}}$ the T_{ign} for dry air was $977\,\mathrm{K}$, and $1013\,\mathrm{K}$ for moist air. However, when when measurement and calibration inaccuracies are taken into account, the differences are within the margin of error.

8 Conclusion

Hot surface ignition of proposed jet fuel surrogates (dodecane, Aachen, and JI unified) at atmospheric pressure was studied. The combustion chamber was a 2.2 liter vessel with optical access, heated to above the dew temperature for the mixture to avoid condensation. The ignition source was a 10 mm x 10 mm stainless steel cylinder (aspect ratio 1) heated at $90\,\mathrm{W}$ to $130\,\mathrm{W}$ and $10.7\,\mathrm{K\,s^{-1}}$ to $14.3\,\mathrm{K\,s^{-1}}$ (average over 45 seconds). The temperature was measured non-intrusively by a custom two-color pyrometer. The uncertainty of the temperature measurements was dominated by the variation in temperature along the surface of 3-5%, and an uncertainty of ±50 K was adopted for all stated temperatures.

For dodecane, the ignition temperature showed no clear dependence on stoichiometry within the flammability limits. The observed variation is believed to be largely due to differences in heating rates, as discussed in 7.2. The average ignition temperature over all 26 experiments ($n = 26$) was $1020 \pm 50\,\mathrm{K}$. The standard deviation of the observations was $s = 27$. The minimum ignition temperature observed was $977 \pm 50\,\mathrm{K}$ at $\phi = 1.47 \pm 0.068$, and the maximum was $1067 \pm 50\,\mathrm{K}$ at $\phi = 0.95 \pm 0.07$. Around stoichiometric conditions ($0.5 < \phi < 1.5$) the minimum ignition temperature was $997 \pm 50\,\mathrm{K}$.

For the Aachen surrogate, the mean ignition temperature ($n = 6$) around stoichiometric ($0.75 < \phi < 1.25$) was $1061 \pm 50\,\mathrm{K}$ ($s = 2.6$). At richer conditions, only one ignition event was captured ($\phi = 2.44 \pm 0.02$) at a temperature of $1122 \pm 50\,\mathrm{K}$, characterized by a weak pressure transient and puffing flame behavior. Another high-temperature attempt at $\phi = 3.07 \pm 0.022$, estimated to be within the upper flammability limit (from Le Chatelier's mixing rule) did not ignite. This could be due to an overestimation of the upper limit, the inability of the cylinder to reach the ignition temperature in this regime, or simply an increased variability in the rich regime.

For the JI unified surrogate, three shots were performed around stoichiometric conditions ($0.79 < \phi < 1.22$). The average ignition temperature (n=3) was $1061 \pm 50\,\mathrm{K}$ (s=4) with a minimum of $999 \pm 50\,\mathrm{K}$ and a maximum of $1006 \pm 50\,\mathrm{K}$.

Over a minimum threshold, the ignition temperature appeared to be dependent on the heating rate of the cylinder. At different heating rates, different ignition temperatures were observed for the same fuel and initial conditions. At comparable power and heating rates, the ignition temperature was very similar for all fuels studied.

Bibliography

[1] J. M. Smith, H. Van Ness and M.Abbott, *Introduction to Chemical Engineering Thermodynamics*, en, 7th ed. 2004. [Online]. Available: https://www.mheducation.com/highered/product/introduction-chemical-engineering-thermodynamics-smith-van-ness/M9781259696527.html.

[2] M. D. Koretsky, *Engineering and Chemical Thermodynamics*, en. John Wiley & Sons, Dec. 2012.

[3] E. E. Ludwig, *Applied Process Design for Chemical and Petrochemical Plants:* en. Gulf Professional Publishing, Nov. 1997.

[4] S. Skogestad, *Chemical and Energy Process Engineering*, en. CRC Press, Aug. 2008.

[5] H. H. J. Rachford and J. D. Rice, 'Procedure for Use of Electronic Digital Computers in Calculating Flash Vaporization Hydrocarbon Equilibrium', *Journal of Petroleum Technology*, vol. 4, no. 10, pp. 19–3, Oct. 1952. [Online]. Available: https://www.onepetro.org/journal-paper/SPE-952327-G.

[6] EPA, 'Methods for Estimating Air Emissions From Chemical Manufacturing Facilities', EPA, Research Triangle Park, NC, Standard, 2007. [Online]. Available: https://www.epa.gov/sites/production/files/2015-08/documents/ii16_aug2007final.pdf.

[7] G. H. Thomson, 'The DIPPR® databases', en, *International Journal of Thermophysics*, vol. 17, no. 1, pp. 223–232, Jan. 1996. [Online]. Available: https://doi.org/10.1007/BF01448224.

[8] W. V. Wilding, R. L. Rowley and J. L. Oscarson, 'DIPPR Project 801 evaluated process design data', en, p. 8, 1998. [Online]. Available: https://dippr.aiche.org/.

[9] CRC, 'Handbook of Aviation Fuel Properties', Coordinating Research Council, SAE, Warrendale, PA, Technical report CRC Report No. 635, 2004, p. 144. [Online]. Available: https://apps.dtic.mil/dtic/tr/fulltext/u2/a429439.pdf.

[10] D. Larsen, *Temperature Effects on the Solubility of Gases*, en, Oct. 2013. [Online]. Available: https://chem.libretexts.org/Bookshelves/Physical_and_Theoretical_Chemistry_Textbook_Maps/Supplemental_Modules_(Physical_and_Theoretical_Chemistry)/Equilibria/Solubilty/Temperature_Effects_on_the_Solubility_of_Gases.

[11] *Medical Definition of Le Chatelier's Principle*, en. [Online]. Available: https://www.merriam-webster.com/medical/Le+Chatelier%27s+principle.

[12] R. Battino, T. R. Rettich and T. Tominaga, 'The Solubility of Nitrogen and Air in Liquids', en, *Journal of Physical and Chemical Reference Data*, vol. 13, no. 2, pp. 563–600, Apr. 1984. [Online]. Available: http://aip.scitation.org/doi/10.1063/1.555713.

[13] R. Battino, 'The Ostwald coefficient of gas solubility', en, *Fluid Phase Equilibria*, vol. 15, no. 3, pp. 231–240, Jan. 1984. [Online]. Available: http://linkinghub.elsevier.com/retrieve/pii/0378381284870090.

[14] S. R. Turns, *An Introduction to Combustion: Concepts and Applications*, en. McGraw-Hill, 2012.

[15] I. Glassman, R. A. Yetter and N. G. Glumac, *Combustion*, en. Academic Press, Dec. 2014.

[16] X. You, F. N. Egolfopoulos and H. Wang, 'Detailed and simplified kinetic models of n-dodecane oxidation: The role of fuel cracking in aliphatic hydrocarbon combustion', *Proceedings of the Combustion Institute*, vol. 32, no. 1, pp. 403–410, Jan. 2009. [Online]. Available: http://www.sciencedirect.com/science/article/pii/S1540748908000898.

[17] S. Banerjee, R. Tangko, D. A. Sheen, H. Wang and C. T. Bowman, 'An experimental and kinetic modeling study of n-dodecane pyrolysis and oxidation', *Combustion and Flame*, vol. 163, pp. 12–30, Jan. 2016. [Online]. Available: http://www.sciencedirect.com/science/article/pii/S0010218015002618.

[18] J. Chomiak, *Combustion: A study in theory, fact and application*, English. Jan. 1987. [Online]. Available: https://www.osti.gov/biblio/7003966-combustion-study-theory-fact-application.

[19] M. G. Zabetakis, 'Flammability Characteristics of Ccombustible Gases and Vapors', en, Bureau of Mines Washington D.C., Tech. Rep. BULL-627, Jan. 1965. [Online]. Available: https://apps.dtic.mil/docs/citations/AD0701576.

[20] F.-Y. Tsai, C.-C. Chen and H.-J. Liaw, 'A Model for Predicting the Auto-ignition Temperature using Quantitative Structure Property Relationship Approach', en, *Procedia Engineering*, vol. 45, pp. 512–517, 2012. [Online]. Available: https://linkinghub.elsevier.com/retrieve/pii/S1877705812032079.

[21] F. Gharagheizi, 'An accurate model for prediction of autoignition temperature of pure compounds', *Journal of Hazardous Materials*, vol. 189, no. 1, pp. 211–221, May 2011. [Online]. Available: http://www.sciencedirect.com/science/article/pii/S0304389411001993.

[22] N. M. Laurendeau, 'Thermal ignition of methane-air mixtures by hot surfaces: A critical examination', *Combustion and Flame*, vol. 46, pp. 29–49, Jan. 1982. [Online]. Available: http://www.sciencedirect.com/science/article/pii/0010218082900050.

[23] H. Wang, E. Dames, B. Sirjean, D. A. Sheen, R. Tango, A. Violi, J. Y. W. Lai, F. N. Egolfopoulos, D. F. Davidson, R. K. Hanson, C. T. Bowman, C. K. Law, W. Tsang, N. P. Cernansky, D. L. Miller and R. P. Lindstedt, *A high-temperature chemical kinetic model of n-alkane (up to n-dodecane), cyclohexane, and methyl-, ethyl-, n-propyl and n-butyl-cyclohexane oxidation at high temperatures, JetSurF version 2.0*, http://web.stanford.edu/group/haiwanglab/JetSurF/JetSurF2.0/index.html, 2010.

[24] C.-W. Zhou, Y. Li, U. Burke, C. Banyon, K. P. Somers, S. Ding, S. Khan, J. W. Hargis, T. Sikes, O. Mathieu, E. L. Petersen, M. AlAbbad, A. Farooq, Y. Pan, Y. Zhang, Z. Huang, J. Lopez, Z. Loparo, S. S. Vasu and H. J. Curran, 'An experimental and chemical kinetic modeling study of 1,3-butadiene combustion: Ignition delay time and laminar flame speed measurements', *Combustion and Flame*, vol. 197, pp. 423–438, Nov. 2018. [Online]. Available: http://www.sciencedirect.com/science/article/pii/S0010218018303675.

[25] A. Stagni, A. Cuoci, A. Frassoldati, T. Faravelli and E. Ranzi, 'Lumping and Reduction of Detailed Kinetic Schemes: An Effective Coupling', en, *Industrial & Engineering Chemistry Research*, vol. 53, no. 22, pp. 9004–9016, Jun. 2014. [Online]. Available: http://pubs.acs.org/doi/10.1021/ie403272f.

[26] E. Ranzi, A. Frassoldati, A. Stagni, M. Pelucchi, A. Cuoci and T. Faravelli, 'Reduced Kinetic Schemes of Complex Reaction Systems: Fossil and Biomass-Derived Transportation Fuels: Reduced Kinetic Schemes of Complex Reaction Systems', en, *International Journal of Chemical Kinetics*, vol. 46, no. 9, pp. 512–542, Sep. 2014. [Online]. Available: http://doi.wiley.com/10.1002/kin.20867.

[27] D. G. Goodwin, R. L. Speth, H. K. Moffat and B. W. Weber, *Cantera: An object-oriented software toolkit for chemical kinetics, thermodynamics, and transport processes*, https://www.cantera.org, 2018.

[28] H. Le Chatelier, 'Estimation of firedamp by flammability limits', *Annals of Mines*, vol. 19, no. 8, pp. 388–395, 1891. [Online]. Available: https://ci.nii.ac.jp/naid/20000832183/.

[29] C. V. Mashuga and D. A. Crowl, 'Derivation of Le Chatelier's mixing rule for flammable limits', en, *Process Safety Progress*, vol. 19, no. 2, pp. 112–117, 2000. [Online]. Available: http://doi.wiley.com/10.1002/prs.680190212.

[30] Egerton Alfred Charles and Powling J., 'The limits of flame propagation at atmospheric pressure II. The influence of changes in the physical properties', *Proceedings of the Royal Society of London. Series A. Mathematical and Physical Sciences*, vol. 193, no. 1033, pp. 190–209, May 1948. [Online]. Available: https://royalsocietypublishing.org/doi/abs/10.1098/rspa.1948.0040.

[31] J. G. Hansel, J. W. Mitchell and H. C. Klotz, 'Predicting and controlling flammability of multiple fuel and multiple inert mixtures', en, *Plant/Operations Progress*, vol. 11, no. 4, pp. 213–217, 1992. [Online]. Available: https://onlinelibrary.wiley.com/doi/abs/10.1002/prsb.720110408.

[32] G. A. Melhem, 'A detailed method for estimating mixture flammability limits using chemical equilibrium', en, *Process Safety Progress*, vol. 16, no. 4, pp. 203–218, 1997. [Online]. Available: https://aiche.onlinelibrary.wiley.com/doi/abs/10.1002/prs.680160403.

[33] C. V. Mashuga and D. A. Crowl, 'Flammability zone prediction using calculated adiabatic flame temperatures', en, *Process Safety Progress*, vol. 18, no. 3, pp. 127–134, 1999. [Online]. Available: http://doi.wiley.com/10.1002/prs.680180303.

[34] T. L. Bergman, F. P. Incropera, D. P. DeWitt and A. S. Lavine, *Fundamentals of Heat and Mass Transfer*, en, 7th ed. John Wiley & Sons, Apr. 2011.

[35] S. Ostrach, 'An analysis of laminar free-convection flow and heat transfer about a flat plate paralled to the direction of the generating body force', en, Jan. 1953. [Online]. Available: http://ntrs.nasa.gov/search.jsp?R=19930092147.

[36] FAA Fuel Flammability Task Group, 'A Review of the Flammability Hazard of Jet A Fuel Vapor in Civil Transport Aircraft Fuel Tanks', U.S Department of Transportation, Tech. Rep., 1998. [Online]. Available: https://www.fire.tc.faa.gov/pdf/ar98-26.pdf.

[37] P. a. E. Panel and C. a. E. P. of AGARD, Eds., *Aircraft Fire Safety: a lecture series*, en, ser. Lecture Series. AGARD 123. Neuilly-sur-Seine, 1982.

[38] FAA, 'Fuel Tank Ignition Source Prevention Guidelines', U.S. Department of Transportation, Standard, 2018. [Online]. Available: https://www.faa.gov/documentLibrary/media/Advisory_Circular/AC_25.981-1D.pdf.

[39] A. 659, 'Standard Test Method for Autoignition Temperature of Chemicals', ASTM International, West Conshohocken, PA, Standard, 2005. [Online]. Available: https://www.astm.org/Standards/E659.htm.

[40] L. R. Boeck, M. Meijers, A. Kink, R. Mével and J. E. Shepherd, 'Ignition of fuel–air mixtures from a hot circular cylinder', en, *Combustion and Flame*, vol. 185, pp. 265–277, Nov. 2017. [Online]. Available: https://linkinghub.elsevier.com/retrieve/pii/S0010218017302523.

[41] P. A. Boettcher, 'Thermal Ignition', PhD, California Institute of Technology, Pasadena, CA, May 2012. [Online]. Available: https://thesis.library.caltech.edu/7037/1/Boettcher_P_A.pdf.

[42] A. M. Brownstein, 'Chapter 7 - Diesel Fuel', in *Renewable Motor Fuels*, A. M. Brownstein, Ed., Boston: Butterworth-Heinemann, Jan. 2015, pp. 67–75. [Online]. Available: http://www.sciencedirect.com/science/article/pii/B9780128009703000078.

[43] ASTM:D6890-16e2, 'Standard Test Method for Determination of Ignition Delay and Derived Cetane Number (DCN) of Diesel Fuel Oils by Combustion in a Constant Volume Chamber', ASTM International, West Conshohocken, PA, Standard, 2016. [Online]. Available: https://www.astm.org/Standards/D6890.

[44] C. P. Wood, V. G. Mcdonell, R. A. Smith and G. S. Samuelsen, 'Development and application of a surrogate distillate fuel', *Journal of Propulsion and Power*, vol. 5, no. 4, pp. 399–405, Jul. 1989. [Online]. Available: https://arc.aiaa.org/doi/10.2514/3.23168.

[45] W. Schulz, 'Oxidation products of a surrogate jp-8 fuel', *ACS Petroleum Chemistry Division Preprints*, vol. 37, no. 2, pp. 383–392, 1991.

[46] T. Edwards and L. Q. Maurice, 'Surrogate Mixtures to Represent Complex Aviation and Rocket Fuels', *Journal of Propulsion and Power*, vol. 17, no. 2, pp. 461–466, Mar. 2001. [Online]. Available: https://arc.aiaa.org/doi/10.2514/2.5765.

[47] A. Violi, S. Yan, E. G. Eddings, A. F. Sarofim, S. Granata, T. Faravelli and E. Ranzi, 'Experimental formulation and kinetic model for JP-8 surrogate mixtures', *Combustion Science and Technology*, vol. 174, no. 11-12, pp. 399–417, Nov. 2002. [Online]. Available: https://doi.org/10.1080/00102200215080.

[48] S. Dooley, S. H. Won, M. Chaos, J. Heyne, Y. Ju, F. L. Dryer, K. Kumar, C.-J. Sung, H. Wang, M. A. Oehlschlaeger, R. J. Santoro and T. A. Litzinger, 'A jet fuel surrogate formulated by real fuel properties', *Combustion and Flame*, vol. 157, no. 12, pp. 2333–2339, Dec. 2010. [Online]. Available: http://www.sciencedirect.com/science/article/pii/S0010218010001896.

[49] S. Dooley, S. H. Won, J. Heyne, T. I. Farouk, Y. Ju, F. L. Dryer, K. Kumar, X. Hui, C.-J. Sung, H. Wang, M. A. Oehlschlaeger, V. Iyer, S. Iyer, T. A. Litzinger, R. J. Santoro, T. Malewicki and K. Brezinsky, 'The experimental evaluation of a methodology for surrogate fuel formulation to emulate gas phase combustion kinetic phenomena', *Combustion and Flame*, vol. 159, no. 4, pp. 1444–1466, Apr. 2012. [Online]. Available: http://www.sciencedirect.com/science/article/pii/S001021801100349X.

[50] S. Honnet, K. Seshadri, U. Niemann and N. Peters, 'A surrogate fuel for kerosene', *Proceedings of the Combustion Institute*, vol. 32, no. 1, pp. 485–492, Jan. 2009. [Online]. Available: http://www.sciencedirect.com/science/article/pii/S1540748908002381.

[51] X. Chen, E. Khani and C. P. Chen, 'A unified jet fuel surrogate for droplet evaporation and ignition', *Fuel*, vol. 182, pp. 284–291, Oct. 2016. [Online]. Available: http://www.sciencedirect.com/science/article/pii/S0016236116304355.

[52] S. Humer, R. Seiser and K. Seshadri, 'Experimental Investigation of Combustion of Jet Fuels and Surrogates in Nonpremixed Flows', *Journal of Propulsion and Power*, vol. 27, no. 4, pp. 847–855, 2011. [Online]. Available: https://doi.org/10.2514/1.46916.

[53] D. Kim, J. Martz and A. Violi, 'A surrogate for emulating the physical and chemical properties of conventional jet fuel', *Combustion and Flame*, vol. 161, no. 6, pp. 1489–1498, Jun. 2014. [Online]. Available: http://www.sciencedirect.com/science/article/pii/S001021801300463X.

[54] M. Meijers, 'Experimental Ignition of Fuel-Air-Mixtures by an Homogeneously Heated Surface', Tech. Rep., 2016.

[55] A. A. Kink, 'Thermal Ignition From a Concentrated Hot Surface', en, Tech. Rep., Jun. 2016.

[56] M. J. Hurley, D. T. Gottuk, J. R. H. Jr, K. Harada, E. D. Kuligowski, M. Puchovsky, J. L. Torero, J. M. W. Jr and C. J. Wieczorek, Eds., *SFPE Handbook of Fire Protection Engineering*, en, 5th ed. New York: Springer-Verlag, 2016. [Online]. Available: https://www.springer.com/la/book/9781493925643.

[57] V. Babrauskas, *Ignition handbook: principles and applications to fire safety engineering, fire investigation, risk management and forensic science*, eng. Issaquah, WA: Fire Science Publishers, 2003.

[58] J. M. Kuchta, *Investigation of Fire and Explosion Accidents in the Chemical, Mining, and Fuel-Related Industries: A Manual*, English, Report, 1985. [Online]. Available: https://digital.library.unt.edu/ark:/67531/metadc12822/.

[59] D. Bjerketvedt, J. R. Bakke and K. van Wingerden, 'Gas explosion handbook', *Journal of Hazardous Materials*, Gas Explosions Handbook, vol. 52, no. 1, pp. 1–150, Jan. 1997. [Online]. Available: http://www.sciencedirect.com/science/article/pii/S0304389497816202.

[60] R. K. Eckhoff, 'Chapter Two - Gas and Vapor Cloud Explosions', in *Explosion Hazards in the Process Industries (Second Edition)*, R. K. Eckhoff, Ed., Second Edition, Gulf Professional Publishing, 2016, pp. 9–149. [Online]. Available: http://www.sciencedirect.com/science/article/pii/B9780128032732000025.

[61] AspenTech, 'Aspen HYSYS 10', Standard, 2018. [Online]. Available: https://www.aspentech.com/v10.

[62] D.-Y. Peng and D. B. Robinson, 'A new two-constant equation of state', *Industrial & Engineering Chemistry Fundamentals*, vol. 15, no. 1, pp. 59–64, 1976.

[63] A. A. Michelson and E. W. Morley, 'On the relative motion of the Earth and the luminiferous ether', en, *American Journal of Science*, vol. Series 3 Vol. 34, no. 203, pp. 333–345, Nov. 1887. [Online]. Available: http://www.ajsonline.org/content/s3-34/203/333.

[64] LIGO Scientific Collaboration and Virgo Collaboration, B. P. Abbott, R. Abbott *et al.*, 'GW170817: Observation of Gravitational Waves from a Binary Neutron Star Inspiral', *Physical Review Letters*, vol. 119, no. 16, p. 161 101, Oct. 2017. [Online]. Available: https://link.aps.org/doi/10.1103/PhysRevLett.119.161101.

[65] W. Merzkirch, *Flow Visualization*, en, 2nd. Elsevier, Dec. 2012.

[66] E. Hecht, *Optics*, en, 5th ed. Pearson Education, Incorporated, 2017.

[67] L. A. Mertens and J. A. Manion, 'B-Bond Scission and the Yields of H and CH3 in the Decomposition of Isobutyl Radicals', *The Journal of Physical Chemistry A*, vol. 122, no. 24, pp. 5418–5436, Jun. 2018. [Online]. Available: https://doi.org/10.1021/acs.jpca.8b01194.

[68] S. P. M. Bane, 'Spark Ignition: Experimental and Numerical Investigation With Application to Aviation Safety', en, p. 284, Jun. 2010.

[69] S. A. Coronel, 'Thermal Ignition Using Moving Hot Particles', en, PhD thesis, 2016.

H

Appendix A

Shot Checklist Procedure

The pre-ignition shot checklist for surrogate-dry air shots is attached in this appendix.

Surrogate Vertical Cylinder Checklist 1.3

Shot: _____

Date & time: _____

Fuel: _____
Batch/Lot number: _____
Composition:
_____ mol%: _____
_____ mol%: _____
_____ mol%: _____
_____ mol%: _____

Air: Dry premixed (Ultra Zero) □
O_2: 21.20 %
CO and CO_2: < 1.0 ppm
Hydrocarbons: < 0.1 ppm
Moisture: 1.98 ppm

P_{fuel}: _____
P_{air}: _____
P_{tot}: _____
ϕ: _____ Fuel/Air T_{dew}: _____

External heating _____

T should be above T_{dew}.
NB: Max $T = 200\,C$ (O-ring failure).

Bottom heating □:
- □ Heating on. Knob level: _____

Injection point heating □:
- □ Make sure heating ropes/tapes are not "hanging loose".
- □ Connect injection thermocouple to Controller and turn on.
- □ Temperature Set Point: _____
- □ Flip "HEAT" switch on. Monitor temperatures.

Ready the laser

- □ Laser ON, EMISSION key ON and shutter OPEN.
- □ Beam path unblocked and no stray reflections.

Ready the camera

NB: Make sure laser beam is expanding (not focused onto the camera chip) before removing lens cap.
- □ Camera ON (plugged in).
- □ Phantom PCC software open.
  Resolution: _____
  Sample rate: _____
  Exposure time: _____
  Trigger delay: _____
- □ Lens cap removed.
- □ Number of fringe-pairs: _____

Ready the pyrometer

- □ Lens cap removed.
- □ Detector 1 (1940 nm) ON:
  Gain: _____ BW: _____
- □ Detector 2 (1705 nm) ON:
  Gain: _____ BW: _____
- □ Steady signal (can take hours)
- □ Pyrometer centered on cylinder

Ready the Oscilloscope

- □ Turn on the Yokogawa DL850E ScopeCorder
- □ Pyrometer 1940 nm detector connected to CH1_1
- □ Pyrometer 1705 nm detector connected to CH1_2
- □ PT1 (Endevco) pressure transmitter connected to CH2_1
- □ "EXT TRIG" connected to Phantom Camera "TRIGGER". Pressure trigger set to: _____
- □ Connect USB flash drive

Evacuate, fill and mix

Caution: DO NOT operate the injection point while power supply is powered on!

- □ V4, V5, V8 closed.
- □ Injection point septum installed and tight.
- □ Open V1 and V2 in LabView (Red = Open).
- □ Open V3 (vacuum line).
- □ Check the vacuum pump oil level.
- □ Start vacuum pump and let run.
- □ Zero PT1 & PT2.
  PT1 (Endevco): _____
  PT2 (HEISE): _____
- □ Close all hand valves.
- □ Stop vacuum pump.
- □ Turn on stirbar (70% of max).
- □ Close V1 and V2 in LabView.
- □ Inject fuel from side.
  Volume: _____
  Partial pressure: _____
- □ Leak? _____
- □ Open V4, V7 and N1 to pressurize piping to 1 atm.
- □ Open V2. Close at equal or desired pressure.
  PT1 (Endevco): _____
  PT2 (HEISE): _____
- □ Close all hand valves.
- □ Stir for 3 minutes.
- □ Turn off stirbar. Settle for 3 minutes. Watch for condensation (pressure decrease).

Pre-ignition reference

Pressure (PT1): _____
Temperature (TT1): _____
Steady-state wall temperatures:
1 Bottom: _____ 2 Top: _____
3 Side: _____ 4 Injection: _____
- □ Press Capture on PCC Software.
- □ Start (arm) Oscilloscope(s).
- □ Press MANUAL TRIG on Yokogawa.
- □ Save reference signals as: _____
- □ Save reference cine as: _____
- □ Press Capture in PCC.
- □ Start (arm) Oscilloscope(s).

Ignition

NB: Power supply supplies current by default when turned on ("load on" by default). Make sure max current (screw) is set below 7.5 A.
Max current: _____
- □ Skin, eye and ear protection.
- □ Output connected and tightened.
- □ Plug in the power supply. Push on button.
- □ Make sure Voltage is sufficient to supply max current.
- □ Press "load OFF" to turn off after ignition (or after 3 min).

Results

Ignition (time): _____
Save signals as: _____
Save cine as: _____
Peak pressure _____
Peak temperature _____
Final pressure _____
Final temperature _____

Comments:

Appendix B

Certificate of Analysis

Certificates of Analysis for the Dodecane and dry air used in the experiments are attached in this appendix.

Certificate of Analysis

SIGMA-ALDRICH

Appendix B Certificate of Analysis

Product Name	Dodecane, *ReagentPlus*®, ≥99%
Product Number	D221104
Product Brand	SIGALD
CAS Number	112-40-3
Molecular Formula	$CH_3(CH_2)_{10}CH_3$
Molecular Weight	170.33

TEST	SPECIFICATION	LOT 00459CS RESULTS
APPEARANCE	COLORLESS LIQUID	COLORLESS LIQUID
REFRACTIVE INDEX AT 20 DEG C	1.422 +/- 0.002	1.4205
INFRARED SPECTRUM	CONFORMS TO STRUCTURE.	CONFORMS TO STRUCTURE AND STANDARD AS ILLUSTRATED ON PAGE 3A OF EDITION I, VOLUME 1 OF "THE ALDRICH LIBRARY OF FT-IR SPECTRA".
GAS LIQUID CHROMATOGRAPHY	99.0% (MINIMUM)	99.36 %
COLOR TEST	20 APHA (MAXIMUM)	<10 APHA
QUALITY CONTROL ACCEPTANCE DATE		MARCH, 1998

Barbara Rajzer, Supervisor
Quality Control
Milwaukee, Wisconsin USA

Airgas
an Air Liquide company

Airgas West region
Airgas USA, LLC
8832 DICE RD
Santa Fe Springs, CA 90670
Airgas.com

CERTIFICATE OF BATCH ANALYSIS

Grade of Product: ULTRA ZERO

Part Number:	AI UZ200	Reference Number:	166-401482518-1
Cylinder Analyzed:	0074260	Cylinder Volume:	236.0 CF
Laboratory:	103 - Santa Fe Springs (W126) - CA	Cylinder Pressure:	2200 PSIG
Analysis Date:	Apr 17, 2019	Valve Outlet:	590
Lot Number:	166-401482518-1		

ANALYTICAL RESULTS

Component	Requested Purity	Certified Concentration
AIR		
CO + CO2	< 1.0 PPM	< 1.0 PPM
THC	< 0.1 PPM	< 0.1 PPM
Percent Oxygen	20-22 %	21.20 %
Moisture	< 2.0 PPM	1.98 PPM

Cylinders in Batch:

0074260, 5329254Y, FT035158, H 004833, H-683212, K-11155, N 154295, S G 1252 B, Z 23912

Impurities verified against analytical standards traceable to NIST by weight and/or analysis.

Signature on file
Approved for Release

Appendix C

Part CAD drawings

The CAD part drawings for the bottom plate, spinbar cavity holder plate and the injection side plate are attached in this appendix.

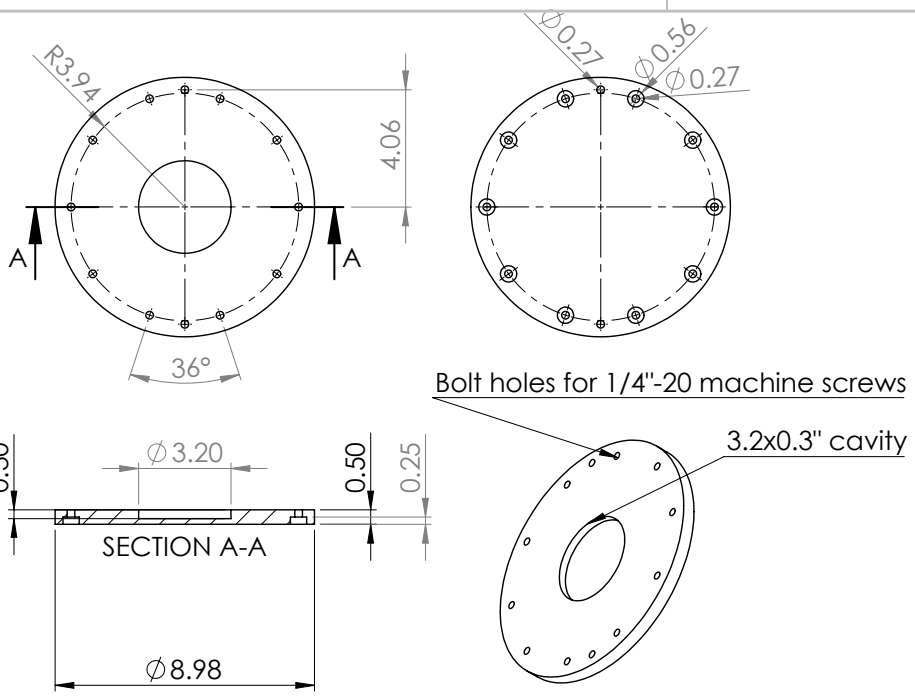

		UNLESS OTHERWISE SPECIFIED:		NAME	DATE
		DIMENSIONS ARE IN INCHES TOLERANCES: FRACTIONAL ± ANGULAR: MACH ± BEND ± TWO PLACE DECIMAL ± THREE PLACE DECIMAL ±	DRAWN		
			CHECKED		
			ENG APPR.		
			MFG APPR.		
		INTERPRET GEOMETRIC TOLERANCING PER:	Q.A.		
		MATERIAL	COMMENTS:		
NEXT ASSY	USED ON	FINISH			
APPLICATION		DO NOT SCALE DRAWING			

PROPRIETARY AND CONFIDENTIAL

THE INFORMATION CONTAINED IN THIS DRAWING IS THE SOLE PROPERTY OF <INSERT COMPANY NAME HERE>. ANY REPRODUCTION IN PART OR AS A WHOLE WITHOUT THE WRITTEN PERMISSION OF <INSERT COMPANY NAME HERE> IS PROHIBITED.

TITLE:

IGGY_BottomPlate_Spinbar2_dr

SIZE	DWG. NO.	REV
A		
SCALE: 1:5	WEIGHT:	SHEET 1 OF 1

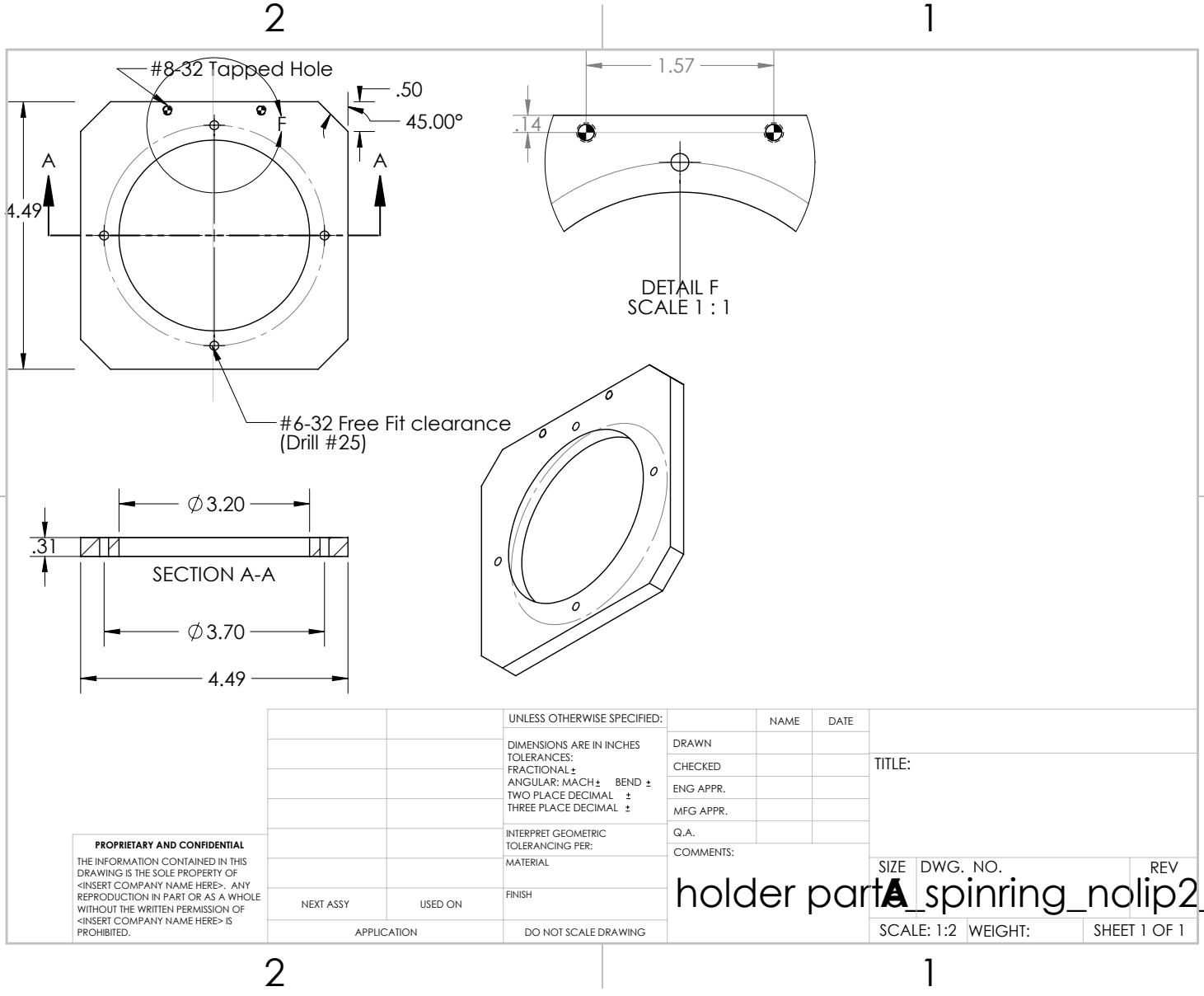
2
1
B
A
#8-32 Tapped Hole
.50
45.00°
F
A
4.49
1.57
.14
DETAIL F
SCALE 1 : 1
#6-32 Free Fit clearance
(Drill #25)
∅3.20
.31
SECTION A-A
∅3.70
4.49
UNLESS OTHERWISE SPECIFIED:
DIMENSIONS ARE IN INCHES
TOLERANCES:
FRACTIONAL ±
ANGULAR: MACH ± BEND ±
TWO PLACE DECIMAL ±
THREE PLACE DECIMAL ±
INTERPRET GEOMETRIC TOLERANCING PER:
MATERIAL
FINISH
DO NOT SCALE DRAWING
NEXT ASSY
USED ON
APPLICATION
NAME
DATE
DRAWN
CHECKED
ENG APPR.
MFG APPR.
Q.A.
COMMENTS:
TITLE:
holder part1_spinring_nolip2_dr
SIZE
DWG. NO.
REV
SCALE: 1:2
WEIGHT:
SHEET 1 OF 1
PROPRIETARY AND CONFIDENTIAL
THE INFORMATION CONTAINED IN THIS DRAWING IS THE SOLE PROPERTY OF <INSERT COMPANY NAME HERE>. ANY REPRODUCTION IN PART OR AS A WHOLE WITHOUT THE WRITTEN PERMISSION OF <INSERT COMPANY NAME HERE> IS PROHIBITED.

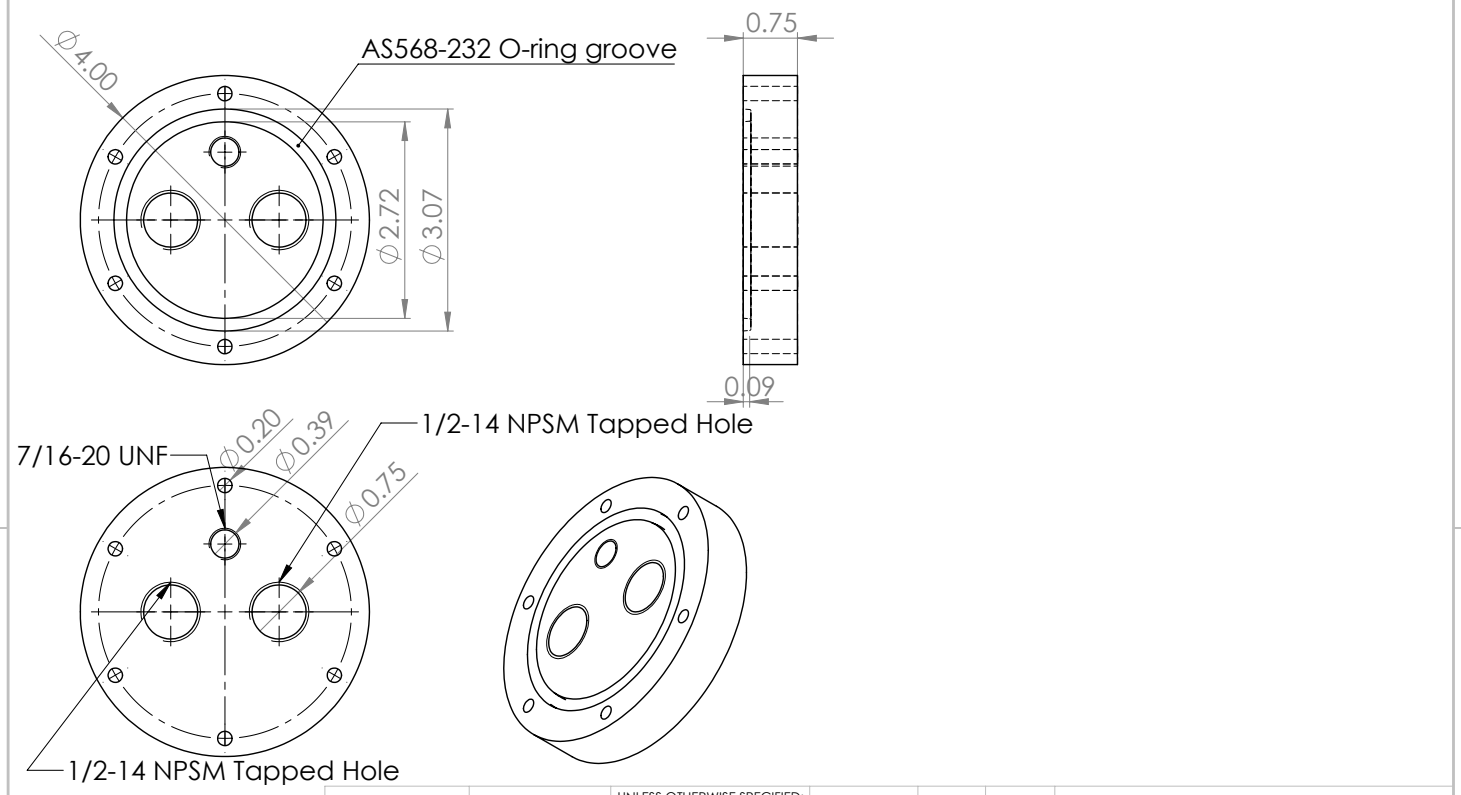

		UNLESS OTHERWISE SPECIFIED:		NAME	DATE
		DIMENSIONS ARE IN INCHES TOLERANCES: FRACTIONAL ± ANGULAR: MACH ± BEND ± TWO PLACE DECIMAL ± THREE PLACE DECIMAL ±	DRAWN		
			CHECKED		
			ENG APPR.		
			MFG APPR.		
		INTERPRET GEOMETRIC TOLERANCING PER:	Q.A.		
		MATERIAL	COMMENTS:		
NEXT ASSY	USED ON	FINISH			
APPLICATION		DO NOT SCALE DRAWING			

PROPRIETARY AND CONFIDENTIAL

THE INFORMATION CONTAINED IN THIS DRAWING IS THE SOLE PROPERTY OF <INSERT COMPANY NAME HERE>. ANY REPRODUCTION IN PART OR AS A WHOLE WITHOUT THE WRITTEN PERMISSION OF <INSERT COMPANY NAME HERE> IS PROHIBITED.

TITLE:

IGGY_injection_cylinder_gland

SIZE	DWG. NO.	REV
A		
SCALE: 1:2	WEIGHT:	SHEET 1 OF 1

Appendix D

Shotlists

Shotlist tables with selected values are attached in this appendix.

Dodecane

Shot	Date	V_{inj}	ϕ	T_{ign}	T_{max}	P_{max}	Air	P_0	T_0	Heating rate
1	04.15.2019	200.0	1.250	1013.5	1019.4	532.388157	Atm	97.87	149.0	11.503333
2	04.16.2019	160.0	1.000	1022.0	1027.8	530.574510	Atm	98.58	130.8	11.890000
3	04.17.2019	130.0	0.830	1024.0	1029.7	518.204778	Atm	98.97	130.3	NaN
4	04.17.2019	90.0	0.540	1017.5	1026.2	474.093921	Atm	99.06	129.3	11.845556
5	04.17.2019	730.0	4.500	NaN	1035.0	NaN	Atm	99.08	129.6	NaN
6	04.17.2019	250.0	1.510	NaN	NaN	NaN	Atm	99.06	130.5	NaN
7	04.23.2019	250.0	1.510	1013.0	1039.5	545.527215	Atm	98.70	128.3	12.805556
8	04.23.2019	500.0	3.070	1025.0	1036.1	272.383469	Atm	98.70	128.0	13.112222
9	04.23.2019	600.0	3.710	1009.0	1026.0	184.355060	Atm	98.69	128.5	12.925556
10	04.24.2019	700.0	4.360	1030.0	1041.7	151.120265	Atm	98.70	129.0	13.187778
11	04.24.2019	75.0	NaN	NaN	NaN	NaN	Atm	NaN	NaN	NaN
12	04.26.2019	160.0	0.966	1026.0	1035.0	537.827828	Atm	98.50	130.2	13.016667
13	04.26.2019	160.0	0.968	1023.0	1033.0	569.503403	Atm	98.50	131.3	12.736667
14	04.26.2019	400.0	2.460	1020.0	1026.3	390.138302	Atm	98.50	131.6	12.887778
15	04.26.2019	100.0	0.600	1025.0	1032.9	472.994977	Atm	98.60	131.6	12.781111
16	04.26.2019	75.0	0.451	NaN	1063.0	NaN	Atm	98.60	131.7	NaN
17	04.28.2019	160.0	0.919	997.0	1009.6	549.347765	Ultra Zero	102.13	124.9	12.570000
18	04.28.2019	160.0	0.934	997.0	1003.8	631.921129	Ultra Zero	101.25	128.0	12.736667
19	04.28.2019	90.0	0.524	997.0	1003.1	471.153772	Ultra Zero	101.41	129.1	12.687778
20	04.28.2019	700.0	4.250	980.0	992.5	340.922070	Ultra Zero	101.32	129.7	12.696667
21	04.28.2019	250.0	1.470	977.0	990.9	606.067936	Ultra Zero	101.45	129.1	12.830000
22	04.28.2019	130.0	0.761	982.0	992.5	563.580290	Ultra Zero	101.00	128.9	12.830000
23	05.02.2019	160.0	0.947	1066.9	1057.3	569.359518	Ultra Zero	101.31	134.5	14.074444
24	05.02.2019	160.0	0.946	1066.1	1054.9	591.551139	Ultra Zero	101.40	134.6	14.185556
25	05.02.2019	200.0	1.189	1061.9	1053.1	616.785560	Ultra Zero	101.29	134.2	14.094444
26	05.02.2019	250.0	1.490	1063.5	1051.3	591.659886	Ultra Zero	101.25	134.5	14.270000

Aachen

Shot	Date	V_{inj}	ϕ	T_{ign}	T_{max}	P_{max}	Air	P_0	T_0	Heating rate
1	05.06.2019	160.0	0.954	1065.0	1067.7	533.907395	Ultra Zero	NaN	137.6	13.376667
2	05.06.2019	130.0	0.777	1060.5	1064.5	475.629708	Ultra Zero	NaN	138.2	13.678889
3	05.06.2019	190.0	1.142	1061.0	1064.7	581.694032	Ultra Zero	NaN	138.5	13.632222
4	05.06.2019	160.0	0.959	1063.5	1066.4	541.416216	Ultra Zero	NaN	138.8	13.698889
5	05.06.2019	160.0	0.961	1061.5	1067.6	537.013881	Ultra Zero	NaN	139.2	14.068889
6	05.06.2019	250.0	1.510	1057.5	1063.0	603.359557	Ultra Zero	NaN	139.1	14.376667
7	05.06.2019	100.0	0.598	NaN	1108.0	105.585038	Ultra Zero	NaN	139.5	NaN
8	05.06.2019	130.0	0.779	NaN	1010.0	103.064346	Ultra Zero	NaN	139.2	NaN
9	05.08.2019	300.0	1.821	NaN	1050.5	109.614595	Ultra Zero	NaN	138.8	NaN
10	05.09.2019	300.0	1.800	NaN	951.0	571.994196	Ultra Zero	NaN	137.2	10.710000
11	05.11.2019	400.0	2.440	1116.0	1122.0	202.016498	Ultra Zero	NaN	137.0	13.918889
12	05.11.2019	500.0	3.070	1123.0	1128.3	109.310601	Ultra Zero	NaN	136.5	NaN
13	05.13.2019	300.0	1.820	928.0	938.2	559.330405	Ultra Zero	NaN	138.6	10.732222
14	05.13.2019	200.0	1.190	919.0	925.6	592.663627	Ultra Zero	NaN	135.9	10.816667
15	05.16.2019	300.0	1.800	940.5	945.8	106.432914	Ultra Zero	NaN	135.2	NaN

JI Unified

Shot	Date	V_{inj}	ϕ	T_{ign}	T_{max}	P_{max}	Air	P_0	T_0	Heating rate
1	04.29.2019 00:30	160.0	0.977	1006.0	1017.2	530.669700	Ultra Zero	101.00	129.0	12.485556
2	04.29.2019 01:00	130.0	0.789	1006.0	1014.2	530.669700	Ultra Zero	101.30	129.3	12.563333
3	04.29.2019 01:45	200.0	1.228	999.0	1019.0	530.242504	Ultra Zero	101.24	130.0	12.816667